UiO : **Department of Geosciences**
University of Oslo

Reservoir Characterization of Utsira High, Central North Sea

Håkon Berggren Olsen
Master's Thesis, Autumn 2021

Abstract

This study entails reservoir characterization of the Triassic and Jurassic succesions of the Utsira Area through petrophysical analyis, rock physics diagnostics and AVO forward modelling of 17 wells 16/1-1, 16/1-2, 16/1-3, 16/1-4, 16/1-5, 16/1-6A, 16/1-7, 16/1-8, 16/1-9, 16/1-10, 16/1-12, 16/1-13, 16/1-15, 16/1-15A, 16/1-17, 16/1-18, 16/1-19 S and 16/1-23 S. The wells are situated on the Utsira High and the Gudrun Terrace in the Central North Sea. The main reservoir units targeted are the Triassic Skagerrak Formation of the Hegre Group and the Jurassic Sleipner Formation of the Vestland Group, with minor discussion of the Pre-Devonian basement. Rotated fault blocks comprise the trapping regime for the Ivar Aasen and Edvard Grieg field, which are the of main interest in this study.

Petrophysical analysis have been conducted to estimate reservoir properties such as shale volume, porosity, water saturation and net-to-gross values. Reservoir and pay zones are estimated through cutoff values from the literature applied on the reservoir properties mentioned. Rock physics diagnostics helped validate and quality control the petrophysical analysis, aswell as providing a qualitative interpretation of the fluid sensitivity, cementation, sorting and lithologies of the reservoir units and sealing layers. AVO forward modelling was conducted on the well log data with fluid replacement testing computing fluid sensitivity analysis which were then labelled under different AVO classes.

The Sleipner Formation was found to portray the generally best reservoir qualities with greater averages of net-to-gross and porosities. However the upper part of the Skagerrak Formation of finely sorted, possibly aeolian, sandstone showed excellent reservoir properties. The reservoir quality of the Skagerrak Formation was found to be quickly deteriorating with depth due to poor sorting in conglomeratic sandstones.

Rock physics diagnostics qualtiy controlled estimations and found highly arkosics sandstones of the Skagerrak Formation to severly disturb shale volume estimation with absent spectral gamma ray logs. Rock physics templates struggled with delineating hydrocarbon bearing from the background trend due to severe compaction.

Heavily cementation was found in increasing depth for the reservoir units, resulting in a great porosity reduction. The Sleipner Formation was found to be carrying the most cementation, correlated with it situated at deeper depths. AVO forward modelling classifies the heavily cemented, conglomeratic reservoirs of the Skagerrak Formation as Class 1 AVO anomalies. A Class 4 AVO anomaly was found in well 16/1-13 (Edvard Grieg 2nd Appraisal) by AVO forward modelling as cementation and compaction was less severe in the finely sorted sandstone part of the Skagerrak Formation. Well 16/1-9 containing gas was classified as a class 3 AVO anomaly.

Uplift was estimated by comparing the log data to P-wave depth relations from laboratoric measurements. Utsira High did not show any significant uplift. Estimation of uplift by the use contact models and empirically derived equations performed poorly in correlating with laboratoric studies of core samples published in literature.

Acknowledgements

I want to send my strongest and most heartfelt compliments and thanks to Professor Nazmul Haque Mondol for the guidance, support, patience and faith given in me througout the time writing this thesis.

I would also like to thank fellow master student partner Alseit Kizatbay for all the discussions, help and support you have shown. I would also like to thank all my student and faculty personell at the Institute of Geosciences which have been so helpful and supportive over the 5 years I have spent at UiO.

Finally I would like to thank my family for their help and support throughout the years of my studies: my mother, father, grandmother, grandfather and brothers.

Contents

List of Figures

List of Tables

CHAPTER 1

Introduction

1.1 Background and Motvation

The North Sea is located between Norway to the east, United Kingdom to the west and Netherlands to the south. The North sea covers around 2 million km^2, with the norwegian part covering about $142000 km^2$. (NPD, 2021b). Since the late 1960s the Norwegian North Sea has been mapped for hydrocarbons, with the first oil discovery found at the northwestern flank of Utsira High (well 25/11-1) in the Balder field (Riber et al., 2015). By 2021, 67 fields are in production in the North Sea.

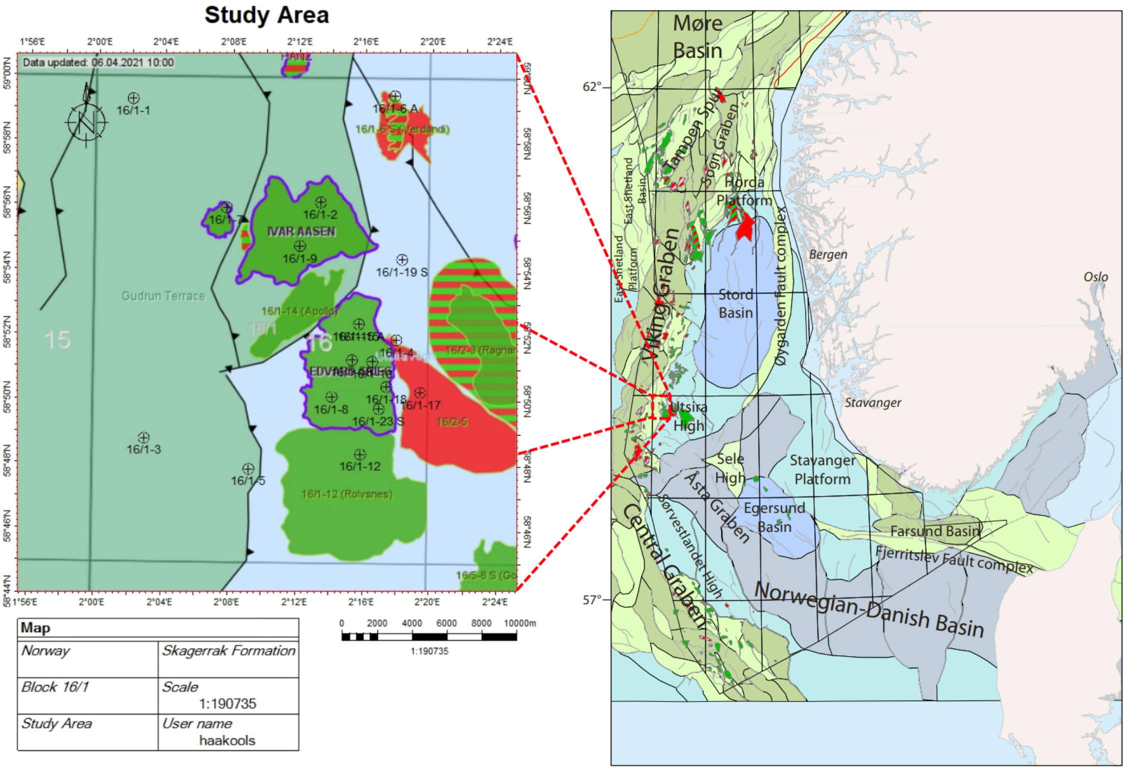

Figure 1.1: Location of study area Utsira High 16/1. (NPD, 2021c)

More and more conventional petroleum reservoirs are being exhausted, and the global demand for energy still favors hydrocarbon as an important life resources. The discovery of the Ivar Aasen field and subsequently the Edvard Grieg field proved that the Utsira High Play was deemed to be a success and paved way for the discovery of the giant Johan Sverdrup. Exploration on the southern part of Utsira High was already conducted in from as early as 1967, with most interestingly the Ivar Aasen field being penetrated by well 16/1-2 without the well log measurements indicating noticeable hydrocarbon saturation (Rønnevik et al., 2017).

The Edvard Grieg field proved that conglomerate reservoirs were a profitable plays and opens up the questions for many undiscovered reservoirs Lundin, 2018. Figure 1.2 from Rønnevik, 2015 shows the reserves of the NCS (Norwegian Contiental Shelf) from the past and interpreted into the future.

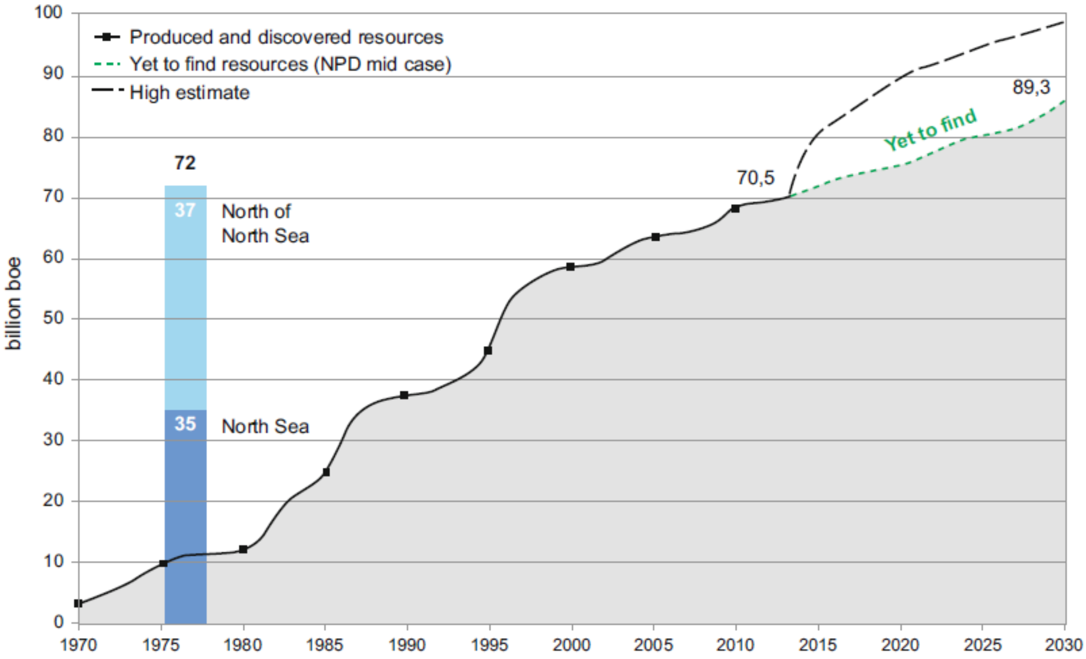

Figure 1.2: Figure showing the growth of reserves on the NCS. The breakthroughs are related to new play types being exercised, with the latest bump in 2010 owed to the discovery of the Johan Sverdrup Field. Figure from (Rønnevik, 2015)

The large bumps in the graph is correlated to new plays being discovered, with the latest significant increase from the Johan Sverdrup Field, which were discovered after the play concept from Ivar Aasen and Edvard Grieg was confirmed (Rønnevik, 2015).

BP, 2021 estimates a minimum of 25% decline in coal consumption by 2050 [1] highlighting the importance of norwegian hydrocarbon production as oil and gas to continue the even greater energy demand of today and the future.

1.2 Research Objectives

The research objectives are to conduct analysis of well logs to identify potential reservoir units and establishing reservoir parameters regarding porosity, shale volume, Sw and net-to-gross, use rock physics templates and diagnostics to help interpret sorting and diagenetic trends, cement volume, compaction indicators and hydrocarbon effects. Lastly to conduct AVO Forward Modelling to classify the reservoirs in terms of AVO anomalies.

1.3 Study area

The study area are selected well in block 16/1 (see figure 1.1 for map and table 1.2), covering the Utsira High and the Gudrun Terrace. The fields in the dataset are the Edvard Grieg and the Ivar Aasen field, as well as the Rolvsness field, Verdandi and Jorvik prospect. (NPD, 2021c)

The Edvard Grieg field is situated on the Utsira High, located in production license 338 operated by Lundin. It was discovered in 2007 and produces oil from Late Triassic to Early Cretaceous age reservoirs and have been producing since November 2015. As of April 2021 it has produced a gross 29.6 million standard cubic meter and expected future investments from 2020 onward are 4.2 billion NOK (NPD, 2021c)

The Ivar Aasen field was discovered in 2008 and is situated on the Gudrun Terrace, just three kilometers north of the Edvard Grieg Field. It is located in production licenses 001 B, 338 BS, 242 and 457 BS and operated by Aker BP. It is comprised of two separate reservoirs namely the Ivar Aasen field and

---

[1] Assuming business-as-usual and no climate benchmarks are met.

the smaller West Cable (16/1-7) discovery. . Production started in 2016 and is producing oil from Late Triassic to Middle Jurassic sandstones Skagerrak, Sleipner and Hugin formations. As of April 2021 it has produced a gross 14.6 million standard cubic meter. Expected future investments are as of 2020 1.6 billion NOK (NPD, 2021c).

Other fields and prospect include the Jorvik Prospect, Verdandi and the Rolvness field. The latter of greatest interest of the lesser prospect and is bordering to the south of the Edvard Grieg. It was discovered in 2009 and test production has started this year.

1.4 Database and softwares

This study is based on well log data from 18 wells , information from published articles, literature and availible information from the NPD (Norwegian Petroleum Directorates) webpages. Key facts displayed in table 1.2 are cited from NPD, 2021c.

For the analysis of the well log data, Hampson Russel (HR), Interactive Petrophysics (IP), Petrel and Python have been used. IP have been used to perform petrophysical analysis while HR have been used to conduct rock physics diagnostics and AVO forward modelling. Petrel have been used to conduct well correlation and thickness map generation of target horizons. Petrel have been used to create thickness map of target horizons as well as maps displaying spatial changes in petrophysical quantites.
Furthermore Microsoft packages (Word, Excel and Powerpoint) have been used for editing, plotting and making figures. LaTeXwas used to create the thesis document.

Table 1.1: Table showing well log availability for the dataset

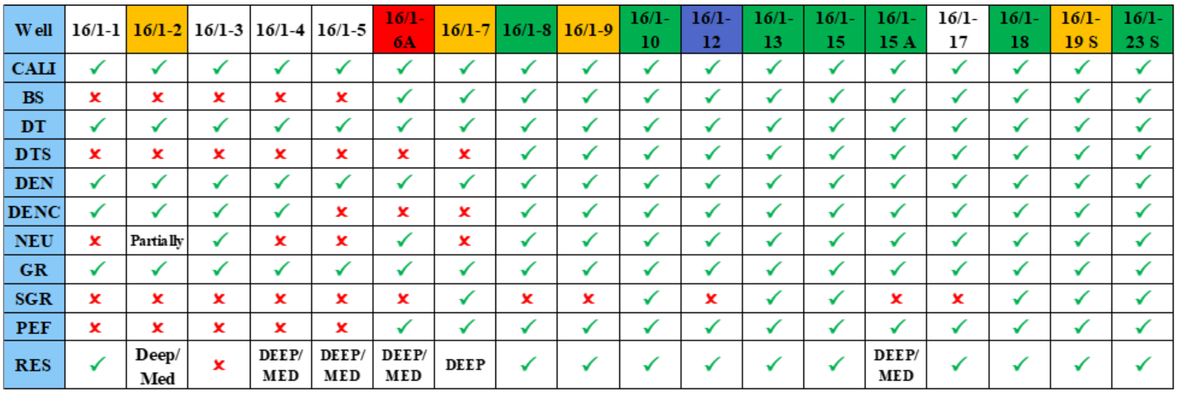

Well	16/1-1	16/1-2	16/1-3	16/1-4	16/1-5	16/1-6A	16/1-7	16/1-8	16/1-9	16/1-10	16/1-12	16/1-13	16/1-15	16/1-15 A	16/1-17	16/1-18	16/1-19 S	16/1-23 S
CALI	✓	✓	✓	✓	✓	✓	✓	✓	✓	✓	✓	✓	✓	✓	✓	✓	✓	✓
BS	✗	✗	✗	✗	✗	✓	✓	✓	✓	✓	✓	✓	✓	✓	✓	✓	✓	✓
DT	✓	✓	✓	✓	✓	✓	✓	✓	✓	✓	✓	✓	✓	✓	✓	✓	✓	✓
DTS	✗	✗	✗	✗	✗	✗	✗	✓	✓	✓	✓	✓	✓	✓	✓	✓	✓	✓
DEN	✓	✓	✓	✓	✓	✓	✓	✓	✓	✓	✓	✓	✓	✓	✓	✓	✓	✓
DENC	✓	✓	✓	✓	✗	✗	✗	✓	✓	✓	✓	✓	✓	✓	✓	✓	✓	✓
NEU	✗	Partially	✓	✗	✗	✓	✗	✓	✓	✓	✓	✓	✓	✓	✓	✓	✓	✓
GR	✓	✓	✓	✓	✓	✓	✓	✓	✓	✓	✓	✓	✓	✓	✓	✓	✓	✓
SGR	✗	✗	✗	✗	✗	✗	✓	✗	✗	✓	✗	✓	✓	✗	✗	✓	✓	✓
PEF	✗	✗	✗	✗	✗	✓	✓	✓	✓	✓	✓	✓	✓	✓	✓	✓	✓	✓
RES	✓	Deep/ Med	✗	DEEP/ MED	DEEP/ MED	DEEP/ MED	DEEP	✓	✓	✓	✓	✓	✓	DEEP/ MED	✓	✓	✓	✓

1.5 Chapter descriptions

Chapter 1 (Introduction) gives a brief introduction to the study area, motivation for conducting reservoir characterization. Study task, availible data,

Chapter 2 (Geological Setting) explains the regional geology, stratigraphy, structural evolution and petroleum systems of Jurassic and Triassic targets encompassed by the surrounding area. Lastly the effects of burial depth, uplift and pressure is discussed.

Chapter 3 (Methods and databases) gives a theoretical, geophysical background for the petrophysical analysis, a brief overview of rock physics and construction of rock physics templates (RPTs) and the theory of AVO (Amplitude versus offset) from published literature. Estimation of uplift is also discussed.

Chapter 4 (Petrophysical Analysis) presents results, interpretation and limitations of petrophysical analysis perfomed from well log data. Lithology discimination, porosity, permeability, pore fluid and is computed and presented along with net to gross values for key reservoir targets in Triassic and Jurassic successions.

Chapter 5 (Rock Physics Diagnositcs) presents results, interpretation and limitations of rock physics diagnostics on the well log data. Cross plots from literature are color coded with porosity, shale volume, water saturation to help link the reservoir to seismic properties. Assesment of lithology, porosity, cementation, sorting and fluid content are conducted concluded evalutation of the validity of the Petrophysical analysis.

Chapter 6 (AVO Forward Modelling) presents the results of AVO forward modelling with interpretation and limitations. Fluid contacts and seal-reservoir interface is plotted in the Intercept-Gradient space and classified by using methods from literature. Generation of synthetic seismic is conducted from well log quantities with the fluid substitution to study different pore fluid scenarios.

Chapter 7 (Summary and Conclusion) provides a summary of key findings in petrophysical analysis, rock physics diagnostics and AVO forward modelling in the target reservoirs contained in the area.

1.6 Limitations and further work

- This study did not have seismic data resulting in a constrained lateral resolution of the study area. Sections of the study affected by this the most is the well correlation and thickness maps shown throughout the study.
- First hand analysis of cores and cuttings, which can heavily improve reservoir characterization, was not possible due to time constraint and the COVID19 pandemic. Core measurements from laboratory and published literature however were compared with the results to quality control the findings.
- This study has been *mainly* focused on reservoir in the Jurassic and Triassic successions, with some additional comments about the thinly draped cretaceous succesions and the basement on Utsira High.
- Spectral Gamma Ray was not availible for all well logs and yielded therefore inaccuracies in the shale volume calculations.
- The fractured basement is of interest for future investigations as it was only briefly discussed in this study.
- This study was originally planned to conduct compehensive machine learning and data science experiments, but were not considered feasible resulting in a strained timescale for the completion.

Table 1.2: Table key information about the well logs included int his study

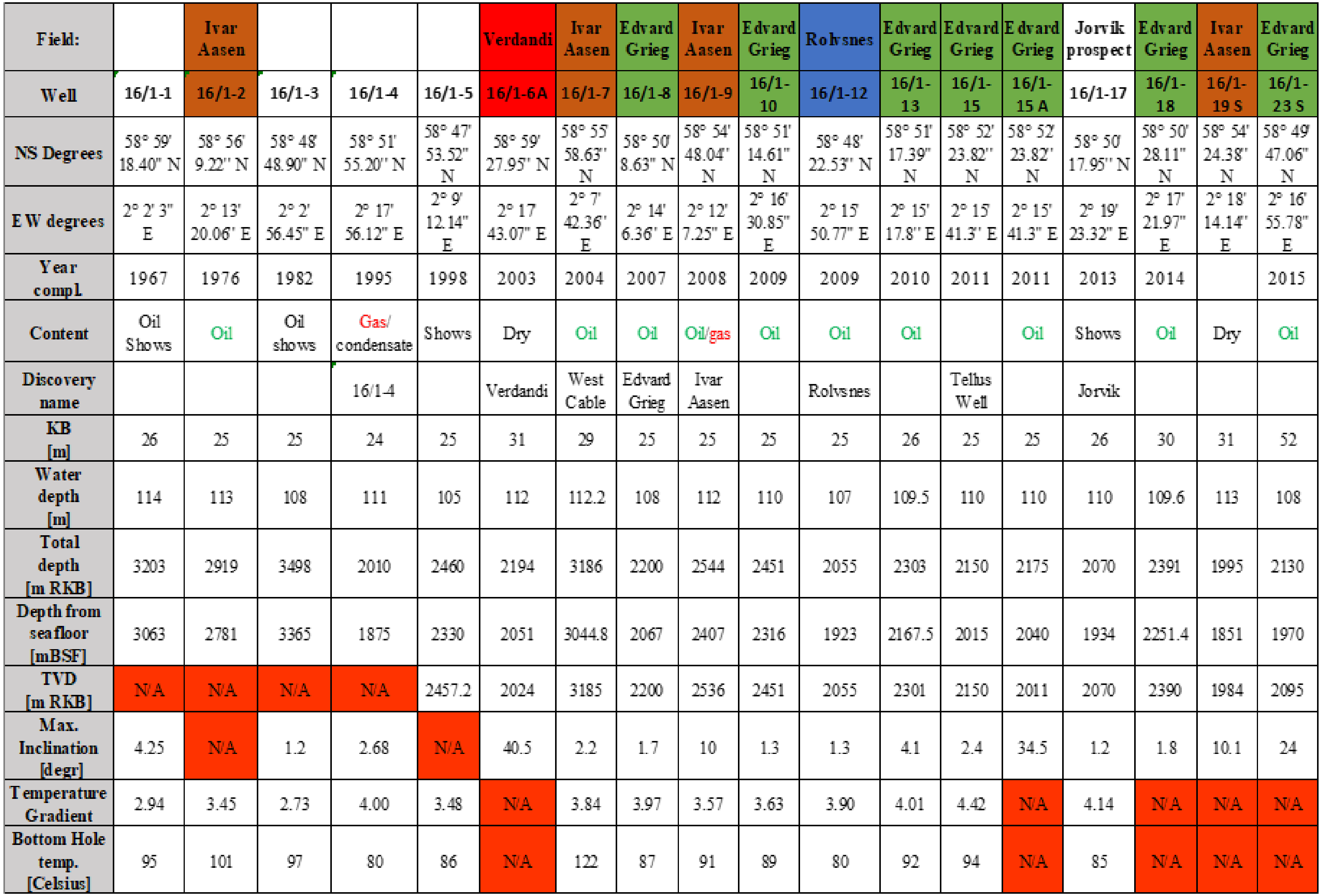

Field:		Ivar Aasen				Verdandi	Ivar Aasen	Edvard Grieg	Ivar Aasen	Edvard Grieg	Rolvsnes	Edvard Grieg	Edvard Grieg	Edvard Grieg	Jorvik prospect	Edvard Grieg	Ivar Aasen	Edvard Grieg
Well	16/1-1	16/1-2	16/1-3	16/1-4	16/1-5	16/1-6A	16/1-7	16/1-8	16/1-9	16/1-10	16/1-12	16/1-13	16/1-15	16/1-15 A	16/1-17	16/1-18	16/1-19 S	16/1-23 S
NS Degrees	58° 59' 18.40" N	58° 56' 9.22" N	58° 48' 48.90" N	58° 51' 55.20" N	58° 47' 53.52" N	58° 59' 27.95" N	58° 55' 58.63" N	58° 50' 8.63" N	58° 54' 48.04" N	58° 51' 14.61" N	58° 48' 22.53" N	58° 51' 17.39" N	58° 52' 23.82" N	58° 52' 23.82" N	58° 50' 17.95" N	58° 50' 28.11" N	58° 54' 24.38" N	58° 49' 47.06" N
EW degrees	2° 2' 3" E	2° 13' 20.06" E	2° 2' 56.45" E	2° 17' 56.12" E	2° 9' 12.14" E	2° 17' 43.07" E	2° 7' 42.36" E	2° 14' 6.36" E	2° 12' 7.25" E	2° 16' 30.85" E	2° 15' 50.77" E	2° 15' 17.8" E	2° 15' 41.3" E	2° 15' 41.3" E	2° 19' 23.32" E	2° 17' 21.97" E	2° 18' 14.14" E	2° 16' 55.78" E
Year compl.	1967	1976	1982	1995	1998	2003	2004	2007	2008	2009	2009	2010	2011	2011	2013	2014		2015
Content	Oil Shows	Oil	Oil shows	Gas/ condensate	Shows	Dry	Oil	Oil	Oil/gas	Oil	Oil	Oil		Oil	Shows	Oil	Dry	Oil
Discovery name				16/1-4		Verdandi	West Cable	Edvard Grieg	Ivar Aasen		Rolvsnes		Tellus Well		Jorvik			
KB [m]	26	25	25	24	25	31	29	25	25	25	25	26	25	25	26	30	31	52
Water depth [m]	114	113	108	111	105	112	112.2	108	112	110	107	109.5	110	110	110	109.6	113	108
Total depth [m RKB]	3203	2919	3498	2010	2460	2194	3186	2200	2544	2451	2055	2303	2150	2175	2070	2391	1995	2130
Depth from seafloor [mBSF]	3063	2781	3365	1875	2330	2051	3044.8	2067	2407	2316	1923	2167.5	2015	2040	1934	2251.4	1851	1970
TVD [m RKB]	N/A	N/A	N/A	N/A	2457.2	2024	3185	2200	2536	2451	2055	2301	2150	2011	2070	2390	1984	2095
Max. Inclination [degr]	4.25	N/A	1.2	2.68	N/A	40.5	2.2	1.7	10	1.3	1.3	4.1	2.4	34.5	1.2	1.8	10.1	24
Temperature Gradient	2.94	3.45	2.73	4.00	3.48	N/A	3.84	3.97	3.57	3.63	3.90	4.01	4.42	N/A	4.14	N/A	N/A	N/A
Bottom Hole temp. [Celsius]	95	101	97	80	86	N/A	122	87	91	89	80	92	94	N/A	85	N/A	N/A	N/A

CHAPTER 2

Geological Setting

2.1 Regional tectonic and structural evolution

The North Sea is a minor epicontental basin subject to multiple periods of extension and rifting in the Mesozoic resulting in grabens and highs, dominated by the N-S Viking Central-Graben. (Riber et al., 2015)

According to Ziegler, 1975, the basin development of the North Sea can be comprised into five stages

1. The Caledonian orogeny (Cambrian-Silurian)
2. Variscan (Devonian-Carboniferous)
3. Permo-Triassic intracratonic stage
4. Taphrogenic rifting stage (Jurassic-Cretaceous)
5. Post-rifting intracratonic stage (Tertiary)

The Caledonian orogeny started with the closure of the Iapetus Ocean and subsidence of both the Laurentia and Baltica margin Gee et al., 2008. In the Silurian to Devoian the collision between Laurentia and Baltica ceased and exhumation of the mountain chain started. Sedimentation from Devonian was dominated in a hot, arid climate with spurious continental deposits preserved on the today Norwegian Continental Shelf. (Riber et al., 2015)

2.1.1 Devonian

The Devonian period was dominated by the Caledonian orogeny which formed the mountain chain which spanned over western Scandinavia, Scotland, East Greenland and a southern part of Poland.The mountain chain was, dimension-wise, its greatest in the earlist Devonian before the collision between Baltica and Laurentia ceased and exhumation, erosion and denudation of the mountain chain became rapid. (Riber et al., 2015) The North Sea drifted northwards to the southern arid belt and the depositional regime was hot and continetal. The Old Red Sandstone was deposited during this time. (Faleide et al., 2015a)

2.1.2 Carboniferous

In the carboniferous period, current day southwest europe moved northwards into the humid equatorial belt. Hercynian/Variscan moutain spawned along a subduction zone through the mid european area when Gondwanaland collided with Baltica and Laurentia, closing the Rheic Ocean. (Riber et al., 2015) A foredeep on the northern side of the mountain chain created large sedimentary units. The swamp ares on the deltaes formed thick beds of coal. In the southern part of the North sea, black marine shales were deposited in the mid-Carboniferous.(Faleide et al., 2015a)

2.1.3 Permian

The Permian period saw current day southwest europe moved into the dry belt of the northern hemisphere. Extension in the latest Carboniferous-Permian with NW-SE trending strike-slip movements. Rifting caused igneous activity, which created the Oslo Graben, but is also present in the offshore subsurface. The sedimentation was primarily within two E-W aligned basins, separated by the Mid-North Sea and the Rinkøbing-Fyn Highs. These basins were filled with the continental derived Rotliegend Group. Most of the sedimentation occurred closed to the mountain chain by alluvial fans and aeolian dune deposits. The dry climate behind the mountain chain caused a marine evaportie basin, with sabkha deposits formed in the marginal areas. In the southern Permian basin Zechstein salt was deposited but is not present in the northern North Sea. (Faleide et al., 2015a)

2.1.4 Triassic

Continued rifting in the Triassic is shown with outbuilding clastic wedges in post-rift basin into the Jurassic.

Sediment supply from the Variscan mountain chain from the south. The Sedimentation rate was high enough to keep up with subsidence, formaing a flat landscape with rivers. The centre of the rift structure may show Triassic sediment thicknesses exceeding 5km. During this time, the Permian salt deposits started forming diapirs. The climate was still arid with predominantly red bed deposits, which deposits on England are called "New Red Sandstone". As the climate became less arid more fluvial sedimentation occurred.

On the margins of the evaporite basins, sabhka deposits was still occuring.

Fluvial sandstones deposited in the Jurassic can have varying sorting and reservoir quality depening on distance of sediment supply and facies, where quartz cementation and clay coatings may be well developed. (Faleide et al., 2015a)

In the Triassic, N-S to NE-SW rifting caused coarse fluvial deposits along the rift margins, with river and lake deposits in the middle of the rift basin.(NPD, 2021a)

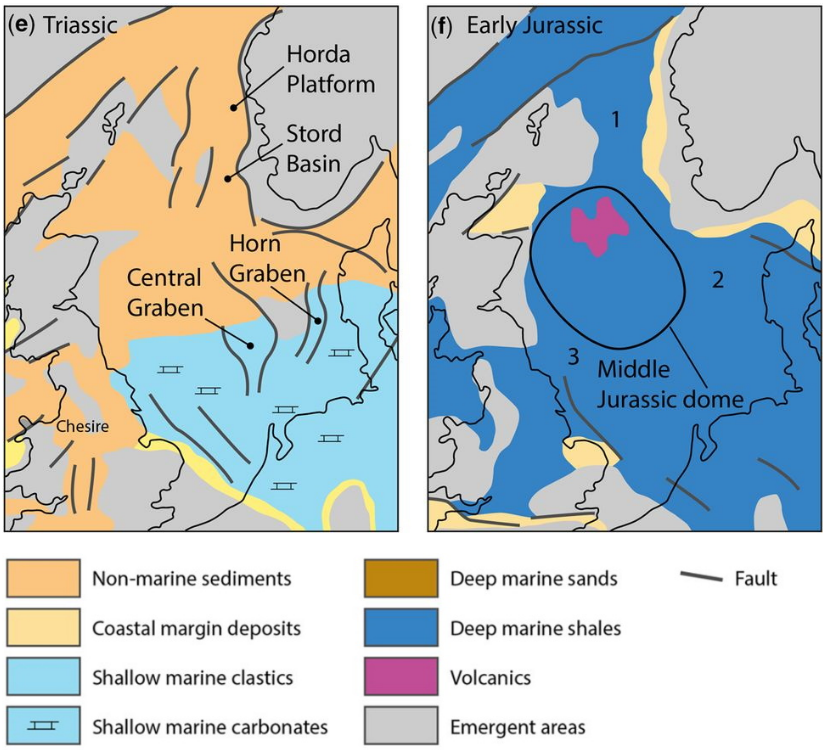

Figure 2.1: Depositional Facies map for the North sea. Figure from Kombrink and Patruno, 2020, based on Zanella et al., 2003

2.1.5 Jurassic

The transition from Triassic to Jurassic is marked with a marine transgression. The climate became more humid as the North Sea moved north of the northern hemisphere arid belt. In the Late Jurassic the volcanism reduced and subsidence occured. Along the Viking Graben, normal faulting rotated and tilted fault block, where the shoulders were subject to erosion removing lower-middle Jurassic to Upper Triassic strata. A marine transgression in the Late Jurassic deposited the clay dominated Heather formation over the Viking Graben. Coarser, sandy deposits from the Heather Formation was deposited as turbidites or along the rift margins as deltas. (Faleide et al., 2015a)

The rift topography allowed for overdeepened, anoxic basins for thich shale sequences to be deposited. These shale deposits serves as an important source rock. The Draupne Formation was deposited in this setting and is also an important seal for hydrocarbon reservoirs in the North Sea. (NPD, 2021a)

The Jurassic saw growth of a volcanic dome over the Viking Graben, Central Graben and the Moray Firth Basin followed the marine transgression and caused uplift and erosion and was followed by rifting (NPD, 2021a). In the Northern north sea, delta systems form depositing sand, shale and coal. (NPD, 2021a) From Late Jurassic into Early Cretaceous occured an importan rifting phase. Major block faulting with uplift and tiling helped create anoxic basins for thick shale sequences to be deposited.

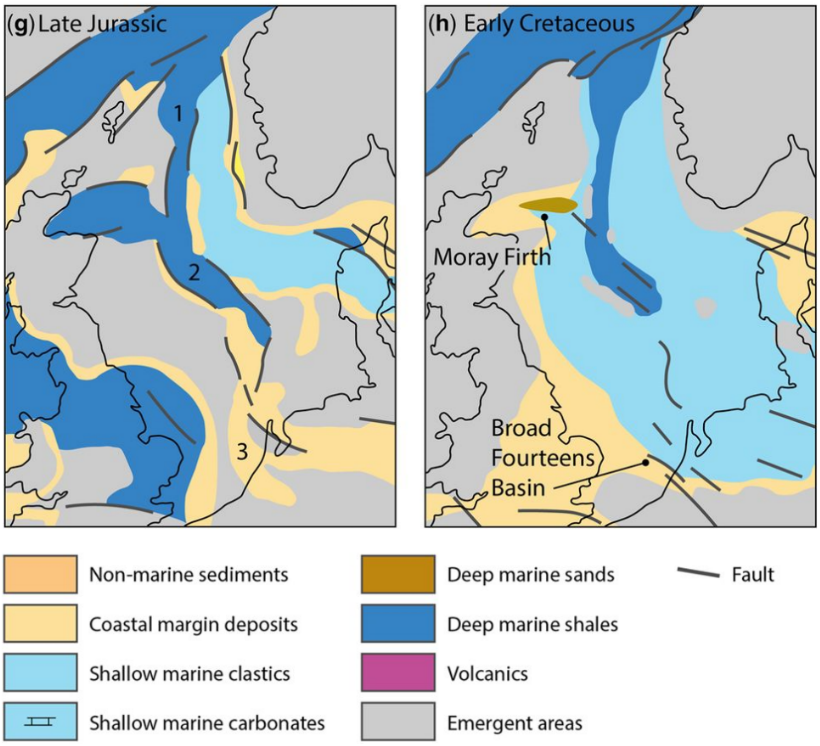

Figure 2.2: Depositional Facies map for the North sea. Figure from Kombrink and Patruno, 2020, based on Zanella et al., 2003

2.1.6 Createceous

The final phase of rifting in the Late Jurassic was followed by a marine transgression, with the uplifted rift structures remained subaerial during the Early Cretaceous. The BCU (Base Cretaceous Unconformity) between Cretaceous and Jurassic is well marked in seismic section.

The post rift stages can be summaries into three distinct stages:

1. **Ryazanian-lates Albian** Inital post rift process had varying degrees of subsidence. Previous structural rift characteristics had major influence on sediment distribution.
2. **Cenomanian-late Turonian** Sediment supply outpaced subsidence, resulting in isostatic/eustatic response.

3. **early Coniacian-early Palaeocene** Syn-rift features evened out and wide saucer-shaped basin configuration. Subsidence ceased as thermal equilibrium had been reached, and the basin infill became extra-basinal.

In the Central and South North Sea, chalk was deposited. Meanwhile northwards the carbonate deposits where more siliclastic. (NPD, 2021a)

2.1.7 Cenozoic

Paleocene and Eocene was influenced by ground movements due to the sea floor spreading of the Atlantic. Chalk deposition continued until early Paleocene.

Inversion caused uplift of basin margins, which created submarine fans starting from the Shetland Platform and transported eastward. These sandy submarine fans interfingered with marine shale deposits in the Rogaland and Hordaland groups.

In the Miocene, deltaic systems on the Shetland Platform is represented in the Skade and Utsira Formations.

Neogene saw major uplift and quaternary glacial erosion of the Norwegian mainland. This caused to thicken the overburden on the Jurassic source rocks such that they reached depths where hydrocarbon generation could occur. (NPD, 2021a)

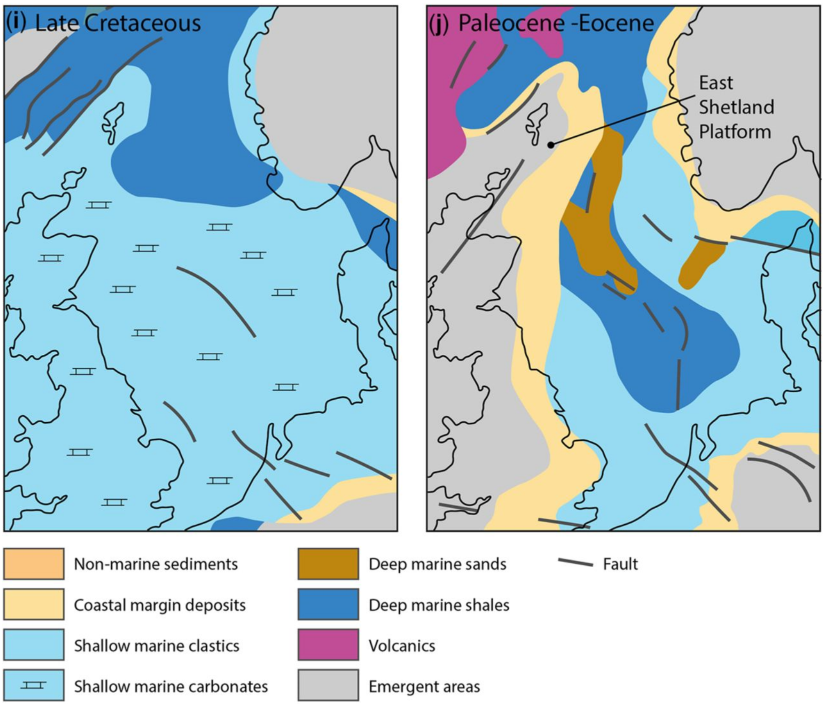

Figure 2.3: Depositional Facies map for the North sea. Figure from Kombrink and Patruno, 2020, based on Zanella et al., 2003

2.2 Structural Elements

The main structural elements in the study area of block 16/1 are the Utsira High and the Gudrun terrace to the east. An idealized cross sectional seismic cartoon of the study area is shown in figure 2.4. The South Viking Graben is on the west side of the structural high

2.2.1 Utsira High

Utsira High is a intrabasinal structural high covering 200 × 50km situated around 180km west of Stavanger, Norway. It has been a positive structural element since the paleozoic Steel and Ryseth, 1990. The Jurassic sediments have been mainly eroded from the high, before the large transgression

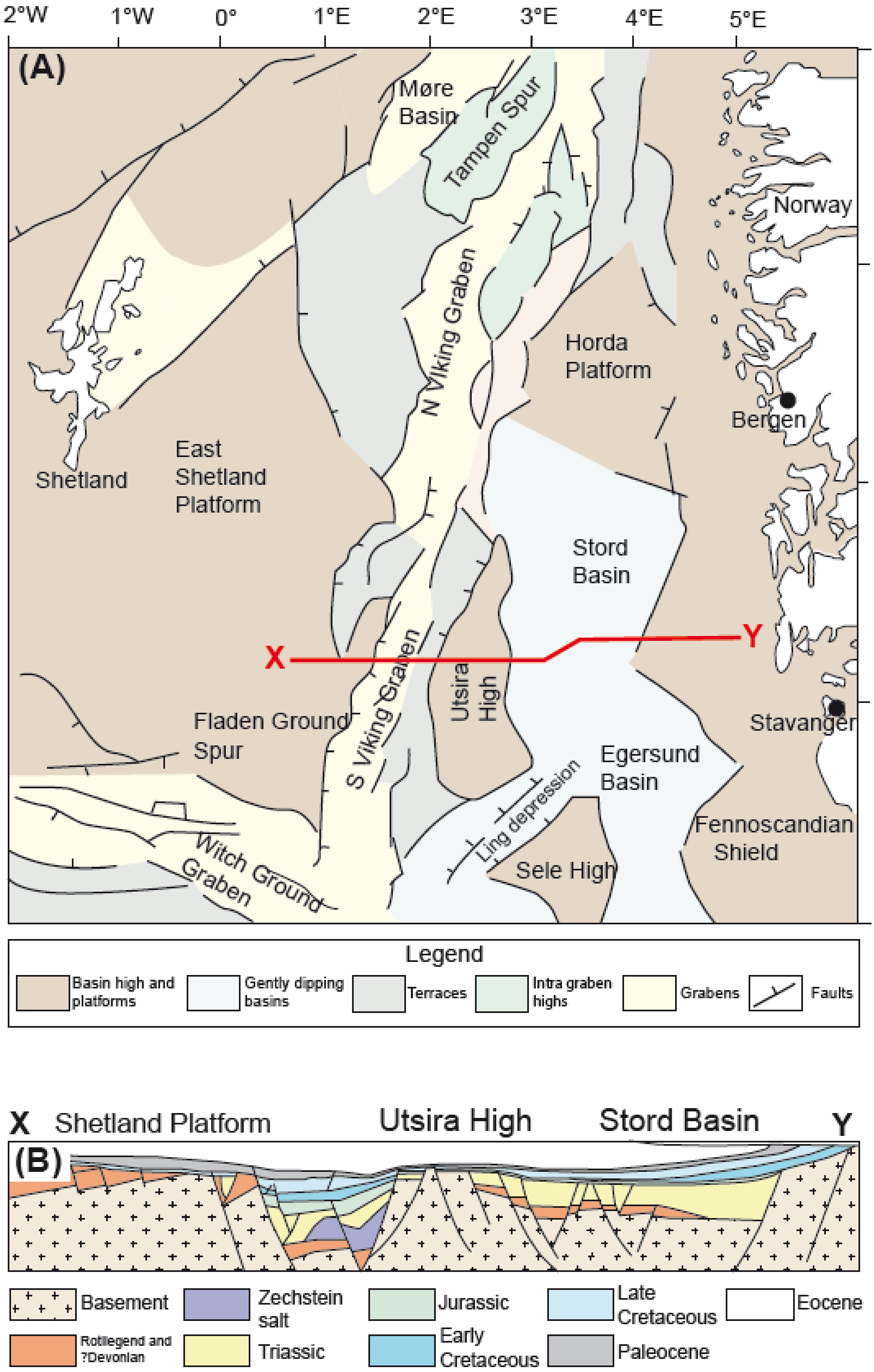

Figure 2.4: Cross section of the Utsira High with the Gudrun Terrace on the western side. Figure from Riber et al., 2015

in the Cretaceous covering the contiental shelf. The southern part of the Utsira High is called the Haugaland High. Almost all mesozoic sediments are eroded towards the center of the Haugaland High, resulting in Cretaceous succession deposited directly on the Pre-Devonian basement (Rønnevik et al., 2017).

2.2.2 Gudrun Terrace

The Gudrun Terrace is a half-graben terrace intermediatedly situated between the Utsira High to the east and the Viking Graben to the west. It is structural related to the Viking Graben, which was mostly spawned during the Jurassic-Cretaceous with crustal thinning and subsequent thermal subsidence. It is thought that the rift axis and orientation is inherited by a predated rift basin from the Permo-Triassic (Faleide et al., 2015a).

2.3 Stratigraphy

The lithostratigraphic column with rifting events around Utsira High is shown in figure 2.5 with the Edvard Grieg reservoir units marked by (R). The column does not contain the Pre-Devonian basement apparent. The lithology mesozoic sediments consists of Triassic conglomeratic deposits, Jurassic sandy deposits from fluvio-deltaic sandstones to shales. Into the cretaceous, a large transgression resulted in quiet contintal shelf setting with depostions of marls and chalks (Faleide et al., 2015a). The formations are more described in greater detail below. The formation to top data from NPD, 2021c are shown in table 2.1.

2.3.1 Shetland Group

2.3.1.1 Ekofisk Formation

The Ekofisk Formation is typically white to leight grey mudstones or wackestones, often alternating with chalky limestones or limestones. Thin beds of calcerous pyritic shales or clays are most common in the lower part of the formation. (NPD, 2021c)

2.3.1.2 Tor Formation

The Tor Formation is generally homogenous, but can consist of alternative white, grey or beige mudstones or wackestones, chalks, chalky limestones or limestones. Fine layers of soft grey-green or brown marl can occur, or rare stringers of calcerous shales. (NPD, 2021c) The depositional environment for the formation is open marine setting with deposition of calcerous debris flows,

2.3.1.3 Hod Formation

The Hod formation consists of hard, white to light grey microcrystalline limestones which may occur argillaceous or chalky. It can be dominated by white, light grey to light brown chalk facies or alternate with limestones. Glauconite can commonly occur in the lower part of the formation, and calcerous clay/shale laminae are occasionally present. (NPD, 2021c)

The depositional environment of the Hod formation is open marine setting with deposition of cyclic palagic carbonates (periodites) and distal turbidites. (NPD, 2021c)

2.3.2 Cromer Knoll Group

2.3.2.1 Sola Formation

The Sola formation is concised of finely laminated, often very pyritic, interbedded with stringers of limestone and marlstone. It was deposited in a marine enviroments with alternating anoxic and oxic bottom conditions (NPD, 2021c).

2.3.2.2 Åsgard Formation

The Åsgard formation is dominated by light to dark grey, olive-grey, greenish and brownish, often calcereous claystones. The claystones may be silty and very fine-grained sandstone layers or laminae are present. Light olive-grey marlstones and stringers of limestone can occur. Mica, pyrite and glauconite

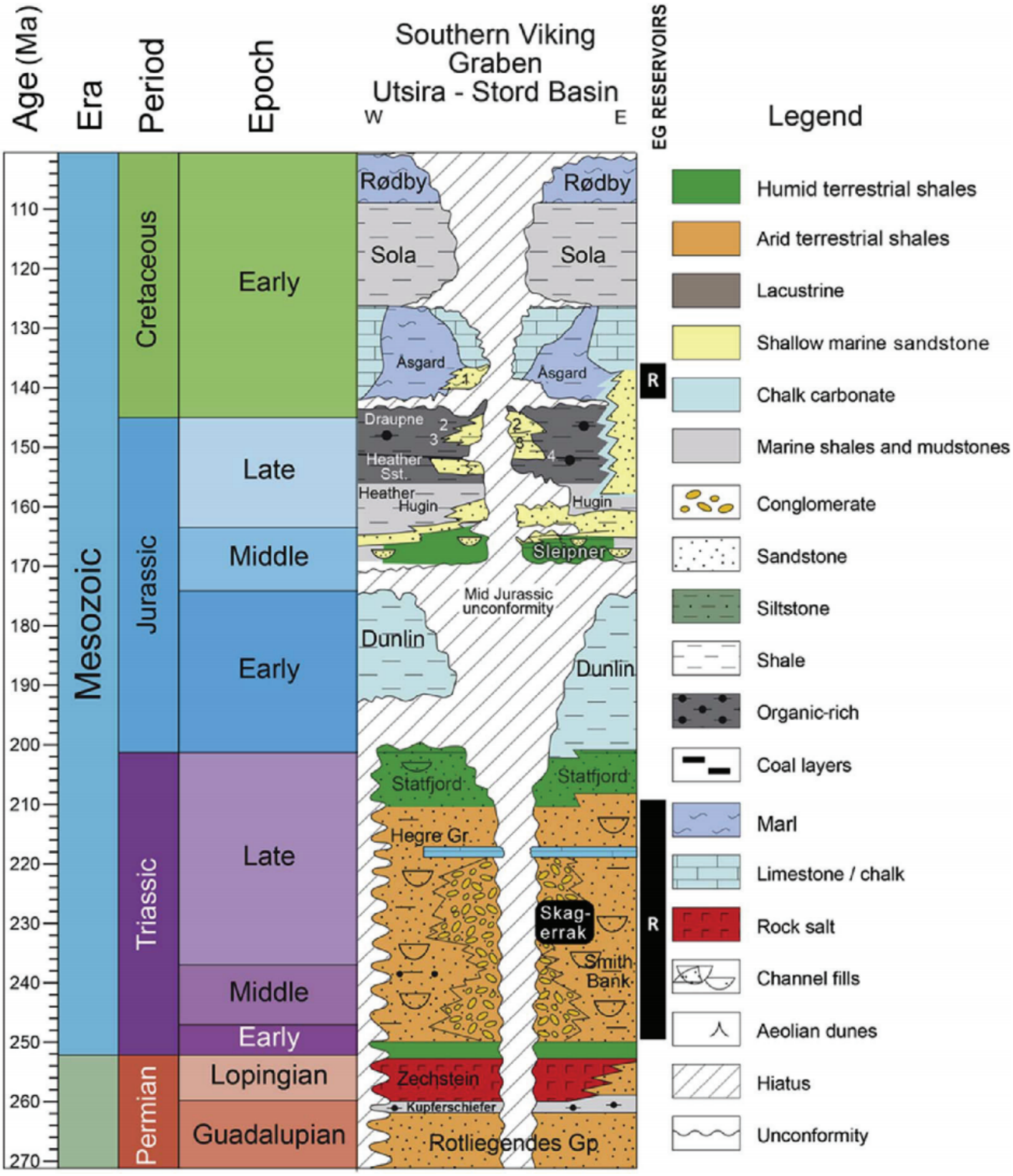

Figure 2.5: Stratigraphic column from Mahmic et al., 2018 for the Utsira High area.

Table 2.1: Table displaying the depth to formations and their corresponding groups and ages from NPD, 2021c, for each well in the dataset. X indicates missing formation and * means there is no group defined.

Age	Group	Formation	16/1-1	16/1-	16/1-3	16/1-4	16/1-5	16/1-6 A	16/1-7	16/1-8	16/1-9	16/1-10	16/1-12	16/1-13	16/1-15	16/1-15	16/1-17	16/1-18	16/1-19	16/1-23
Neogene	Nordland	Utsira	644	740	732	768	745	722	717	745	757	756	734	766	774	778	758	757	771	780
	Hordaland	Skade	908	930	1043	918	1002	866	920	963	939	954	1003	952	944	952	976	978	901	104
		Grid	1854	1660	1610	1539	1617	1530	1631	1556	158	1494	1633	1467	1553	1598	X	158	1501	1621
Paloecene	Rogaland	Balder	2207	1973	2125	1686	1896	1876	2130	1765	1979	1734	1727	1764	1766	1889	1667	1693	1727	1750
		Sele	2259	2018	2168	1696	1922	1914	2197	1781	2041	1744	1751	X	1778	1899	1678	1702	1738	176
		Lista	2361	2060	2219	1734	1932	1952	2263	1801	2090	1772	1777	X	1800	1920	1717	1742	1763	1809
		Hermod	2316	X	X	X	X	X	X	X	X	X	X	1787	X	X	X	X	X	X
		Heimdal	2402	2098	2423	X	X	2007	2327	X	2126	X	X	X	X	X	X	X	X	X
		Våle	2646	X	X	1817	2004	2056	X	1891	2176	1772	1837	1877	1879	2026	1789	1824	X	1879
Cretaceous	Shetland	Ekofisk	2734	2192	2458	1834	X	2163	2522	1897	2179	1860	1845	1888	1889	2043	1806	1840	1845	1901
		Tor	2763	2192	2458	X	X	2181	2560	X	X	X	1865	X	1906	2057	1822	1868	X	1916
		Hod	2926	2192	2458	X	2008	X	X	1913	X	X	1888	1917	1913	2064	1850	1878	X	1934
	Cromer Knoll	Sola	X	2236	2603	1860	X	X	2727	X	X	1890	1902	X	X	X	1860	1883	X	1943
		Åsgard	X	2236	2603	X	X	X	2727	X	2221	1890	1909	1918	1915	2067	1861	1885	1878	1946
Jurassic	Viking	Draupne	X	X	X	X	X	X	2747	1925*	X	1890*	1912	X	X	X	X	X	X	X
		Intra Draupne	X	X	X	X	X	X	X		X		X	X	X	X	X	X	X	X
		Intra Heather	X	2242	X	X	2020	X	X		X		X	1919	X	X	X	X	X	X
		Heather	X	2283	2707	X	2155	X	2918		2267		X	X	X	X	X	X	X	X
	Vestland	Hugin	X	X	X	X	X	X	X		X		X	X	X	X	X	X	X	X
		Sleipner	X	X	2730	X	2175	X	2953		2399		X	X	X	X	X	X	X	X
Triassic	Hegre	Skagerrak	X	2424	X	X	2247*	X	3083	1964*	2456	X	X	1960	X	X	1870	1894	X	1953
		Smith Bank	X	2620	2840	X		X	X		X	X	X	X	X	X		X	X	X
Permian	Zechstein		X	2713	3082	X	X	X	X	X	X	X	X	X	X	X	X	1985*	X	X
	Rotliegend		X	2808	3230	X	X	X	X	X	X	X	X	X	X	209	X		X	X
Devonian	Basement		X	2912	3440	1864	2265	X	X	X	X	X	X	X	1920	2069	1988	2360	1891	2094

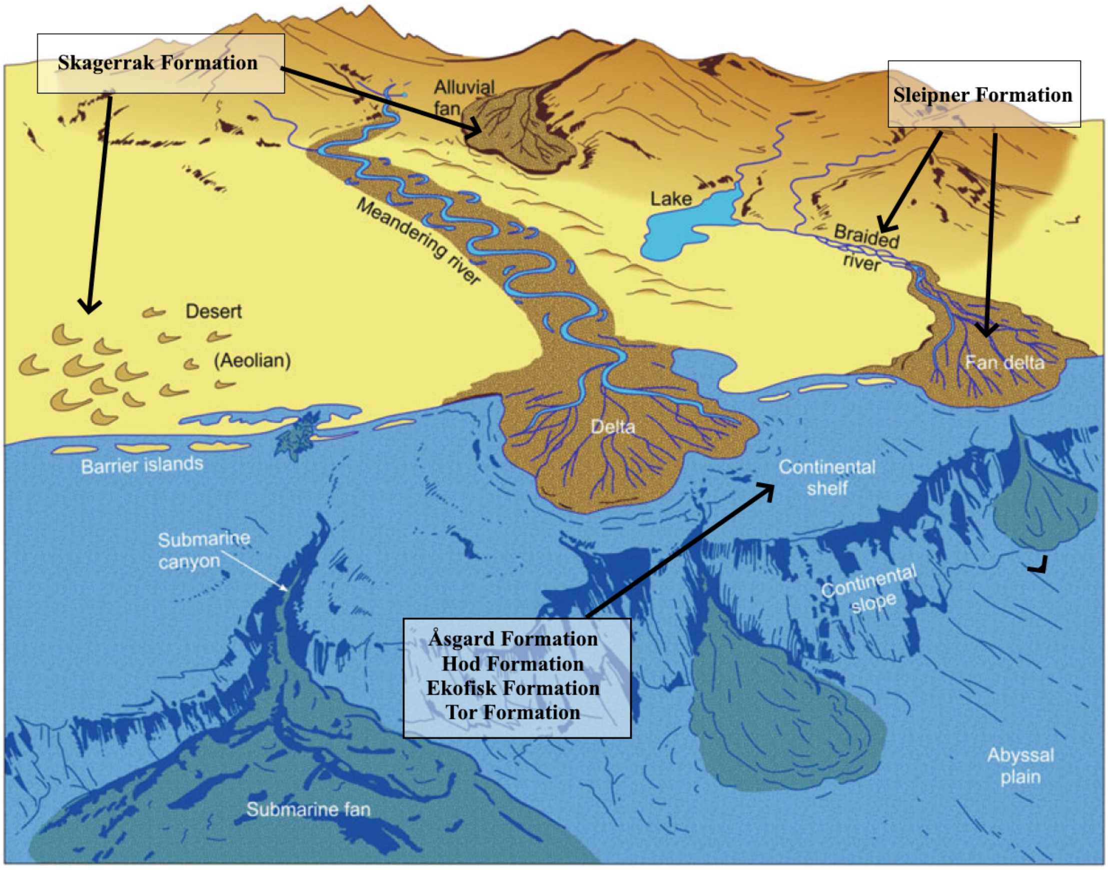

Figure 2.6: Figure showing the depositional regime of the the main formation discussed. Figure adapted from **bjorlykke2015**.

occur commonly (NPD, 2021c). The depositional enviroment for the formation was an open marine, low-energy shelf environment with well-oxygenated bottom water (NPD, 2021c).

2.3.3 Viking Group

2.3.3.1 Draupne Formation

The Draupne formation is comprised of dark grey-brown to black, usually non-calcareous, carbonaceous claystone. It is characterized by a very high radioactivity (often over $100 API$ units) due to its organic carbon content. Other log responses are low velocity, density and a high resistivity. Minor limesotne straks occur throughout, and also interbedded sandstones and siltstones which can cause a decrease in radioactivity (NPD, 2021c).

The depositional environment for the formation is a marine environment with restricted bottom circulation and often with anaerobic conditions. Where the formation contains sandstones, the origin is considered to be of turbiditic origin (NPD, 2021c).

2.3.3.2 Heather Formation

The Heater formation is comprised of dark grey, carbonaceous, silty claystone with thin limestone streaks. It is comprised in two different divisions by changes in dip and gap in biostratigraphical data, but the lithology remains similar (NPD, 2021c).

The Heather formation was deposited in an open marine environment (NPD, 2021c).

2.3.4 Vestland Group

2.3.4.1 Hugin Formation

The Hugin formation contains very fine to medium grained sandstone with frequently calcareous and glauconitic. Fair sorting and subangular to subrounded grains. Coarser layers and thin coal beds can occur (NPD, 2021c).

2.3.4.2 Sleipner Formation

The Sleipner formation consists of both non calcareous, fine to medium grained sandstone with occurring coarse and pebbly layers, and medium to dark grey silty claystones. Beds of mature black and massive coals is common (NPD, 2021c). The depositional environment of the Sleipner formation is found to be a fluviodeltaic coaly sequence.(NPD, 2021c)

2.3.5 Hegre Group

2.3.5.1 Skagerrak Formation

The Skagerrak formation was mostly deposited in a alluvial fans, and is comprised of conglomerates, sandstoens, siltstones and shales. Subordinate lithologies are anhydrites, dolomites and limestones. The sandstones are arkosic or highly lithic (NPD, 2021c).

Deposited as an alluvial fan, the Skagerrak formation is composited of sandstones with various siltstones and shales. Aeolian dunes alongside flash flood deposits are also occurring (Steel and Ryseth, 1990) (Mahmic et al., 2018).

2.3.5.2 Smith Bank Formation

Smith Bank Formation is on the Norwegian sector consisting of monotonous red to somewhat silty claystone. Conglomerates, marl, calcareous components like limestone and dolomite and lastly dark shale occurs in minor components (NPD, 2021c).

The depositional environment is a range of distal continental environments, with predominantly fine grained clasitcs deposited (NPD, 2021c).

2.3.6 Zechstein

Zechstein group is comprised of evaporates and carbonates with local clastic rocks occuring. In the basin-centre, halites are dominating while the basin margins contain limestones, dolomites and anhydrates (NPD, 2021c).

2.3.6.1 Kupferschiefer Formation

The Kupferschiefer formation is a thin, grey-black, radioactive, locally calcaerous organicly rich shale. Due to its radioactivity, it is easily distinguished in logs with a very large gamma ray response (NPD, 2021c).

2.3.7 Rotliegend Group

Rotliegend Group consists of clays, shales, sandstones and minor conglomerates. In the lower part, volcanic rocks and tuffaceous sediments are common. Deposited in a continetal, arid environment, the sediments are frequently red (NPD, 2021c).

2.4 Petroleum Systems

Exploration in the North Sea has been conducted for over 50 years and contains the majority of Norways largest fields showing a clear petroleum system in play. Definitions from Magoon and Dow, 1994 defines the needed elements to create a petroleum system to be

- Source rock

- Reservoir rock
- Cap rock
- Overburden

The cap rocks combined with overburden is important to trap and accumulate hydrocarbon volumes to satisfactory amounts for production to be deemd feasible. These elements will be discussed below.

2.4.1 Source Rocks

The primary source rocks in the Central North Sea are organic rich shales from the Draupne Formation. These were deposited in deep water under (Isaksen and Ledje, 2001) The Utsira high does not contain any very organically rich, jurassic shales. Long distance migration paths through the Gudrun Terrace from the South Viking Graben is suggested (Isaksen and Ledje, 2001). Figure 2.7 shows the depositional environment of the draupne formation. The burial depth increases westwards from the Utsira High approaching the South Viking Graben.

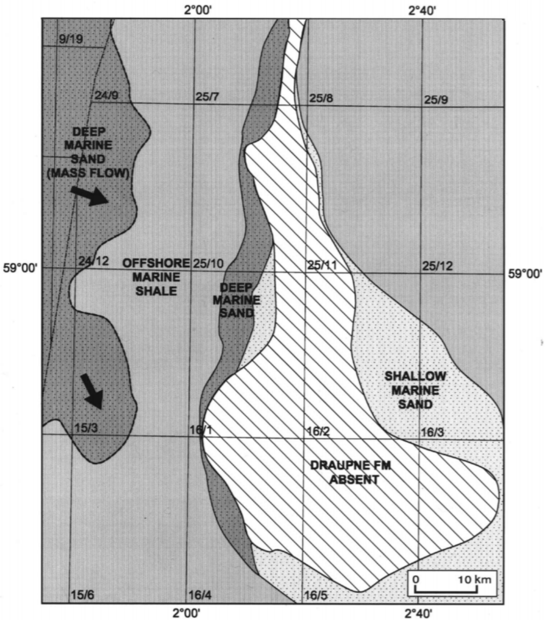

Figure 2.7: Map showing the depositional environments of the Draupne formation around the study area. The asbence of the Draupne Formation gives an outline of the Utsira High. Modified from Isaksen and Ledje, 2001

2.4.2 Reservoir Rocks

Dominant reservoir rocks in the central North sea are typically sandy formations of Jurassic age. The Triassic succession are either buried to deeply (e.g. Rotliegend sandstones) or eroded. However rotated fault block on the eastern side of the Utsira High has kept the Triassic Succession of the Hegre Group present (Gregersen et al., 1997). The key reservoir units targeted in this study are the Sleipner Formation of Jurassic age and the Skagerrak Formation of Triassic age. The Sleipner formation is a prominent reservoir rock in the central north sea producing from the Ivar Aasen field and the Sleipner Vest Field (Faleide et al., 2015a; NPD, 2021c).

Well correlation with flattened top in the Sleipner Formation is shown in figure 2.8. Remaining well correlations are shown in appendix D, figure D.1.

Additionally there is hydrocarbon shows in the underlying basement in the Edvard Grieg field. In the northern part of the Edvard Grieg field is a NWW-SEE trending fault dipping southwards, separating the Triassic succession from the rest of the reservoir, resulting in the fractured basement being the main reservoir unit (Riber et al., 2015; Trice et al., 2019).

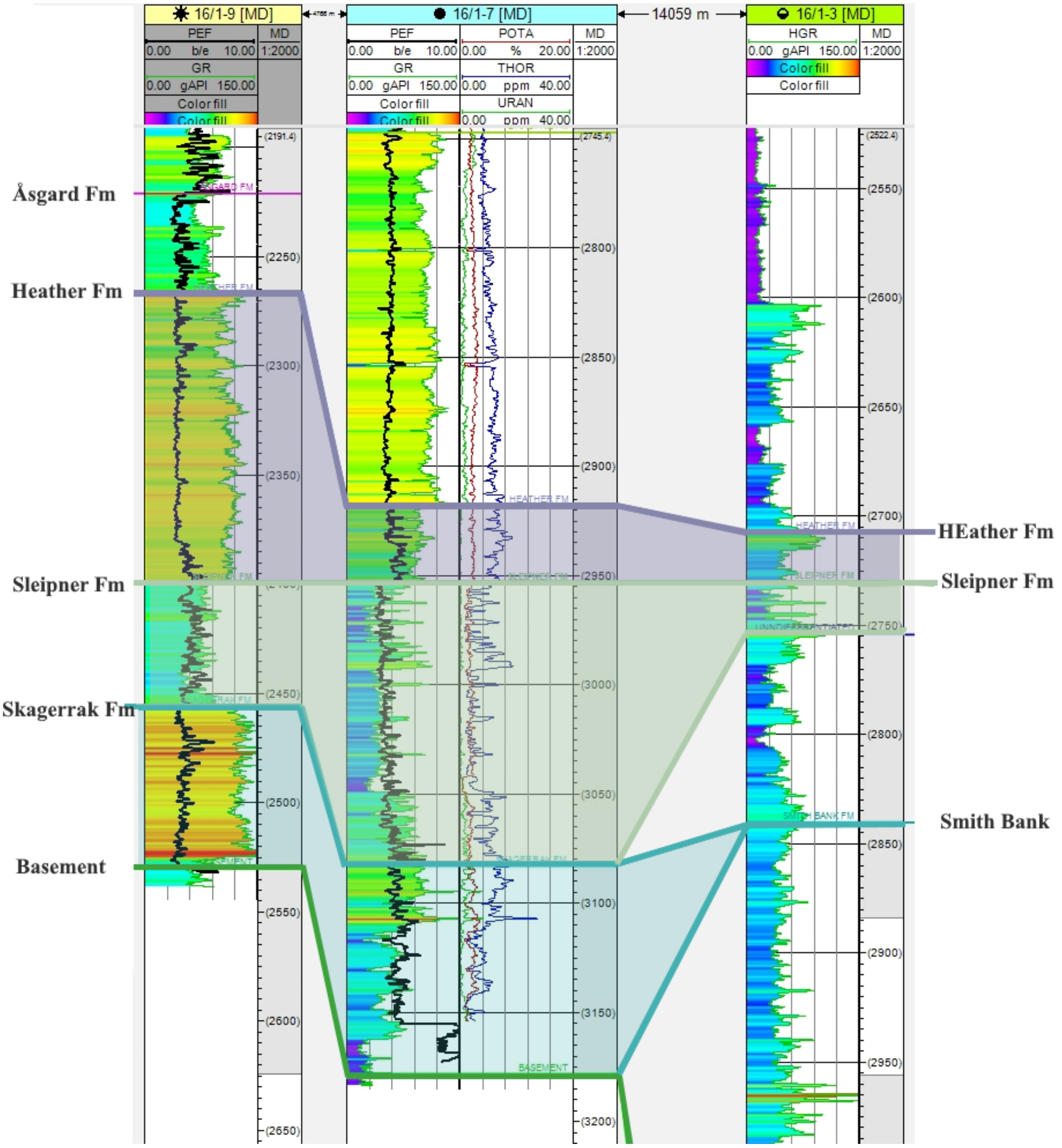

Figure 2.8: Well correlation of the Sleipner Formation conducted in Petrel.

2.4.3 Plays and trapping regime

The north sea can be divided into two petroleum plays, namely the Central Graben area and the northern North Sea Faleide et al., 2015b. For the Utsira High area, rotated fault block of Jurassic age constitutes the most important play (Isaksen and Ledje, 2001), along with fractured basements (Trice et al., 2019). This is visible from figure 2.9 from Rønnevik, 2015 showing transection of the Utsira High with prominent oil fields. The overlying seal on the utsira high varies. Early cretaceous shales are draped on the sourthern parts while the northern parts is sealed with Late Cretaceous chalk (Trice et al., 2019).

2.4.4 Pressure

Knowledge of the pressure regime in the reservoir is crucial. Not being able to compensate the reservoir pressure with the mud filtrate can result in hazardous blowouts where reservoir fluids rapidly and violently climb up to the surface (Bjørlykke, 2015b). For reservoir characterization, knowledge of the pressure can be very benefitial for the employment of rock physics models (see 3.5).

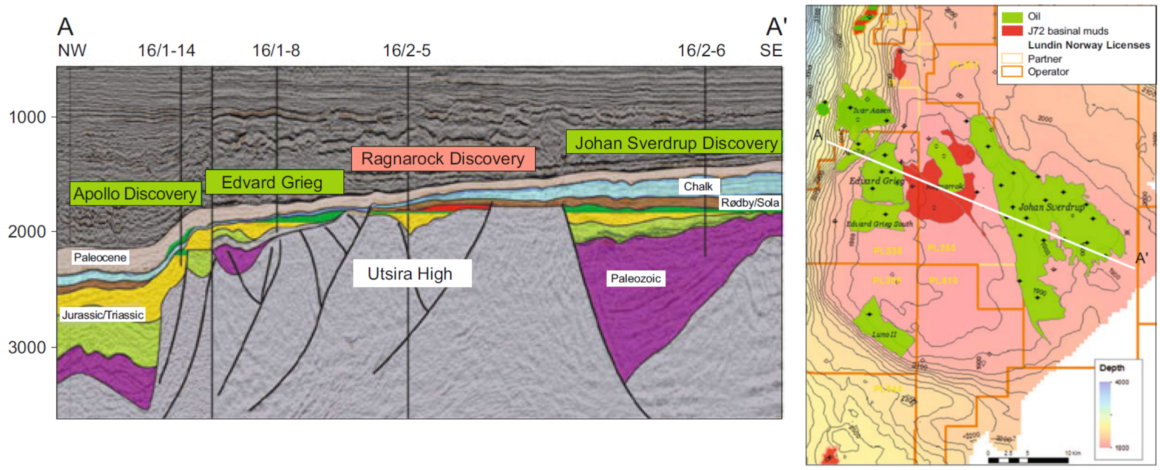

Figure 2.9: Seismic cross section of the Utsira High showing prominent oil fields in the area such as the Johan Sverdrup Field, Apollo and Edvard Grieg. (Rønnevik, 2015)

The effective pressure is defined as the difference between the pressure from the overburden subtracted with the pressure from the porepressure (see fig 2.10). The overburden can again be calculated with more care taking into account the water column of the sealevel, resulting in

$$P = g\left(\int_{Z_{MSL}}^{Z_{OB}} \rho_{fl} dz + \int_{Z_{OB}}^{Z} (\rho_m - \rho_{fl} dz\right) \tag{2.1}$$

where g is the gravitational constant, Z_{MSL} is the depth of mean sea level (assumed calculated from RKB), Z_{OB} is depth of the ocean bottom, Z is the depth of interest and ρ_m and ρ_{fl} are the density of the matrix and the fluid, respectively.

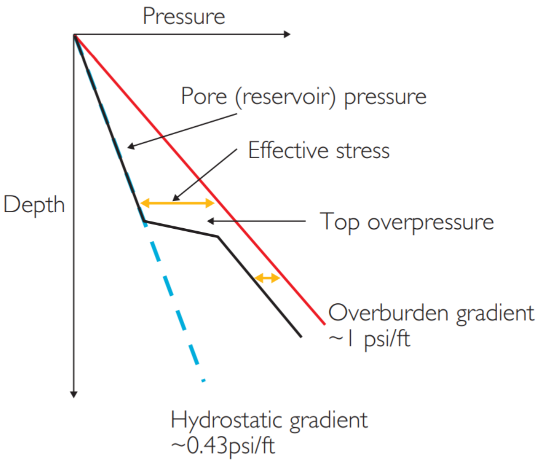

Figure 2.10: Figure showing pressure as a function of depth. Figure from Simm et al., 2014

CHAPTER 3

Research methodologies and theoretical background

3.1 Workflow

The overarching workflow for this study is shown in figure 3.1. Well log data was quality controlled prior to the analysis with the gathering of well top data. Uplift was estimed comparing the well log data to normal compaction trends from laboratoric measurements. The petrophysical analysis was carried out in Interactive Petrophysics, followed by rock physics diagnostics carried out in both IP and Hampson Russell. The AVO forward modelling was done completely in Hampson Russel.

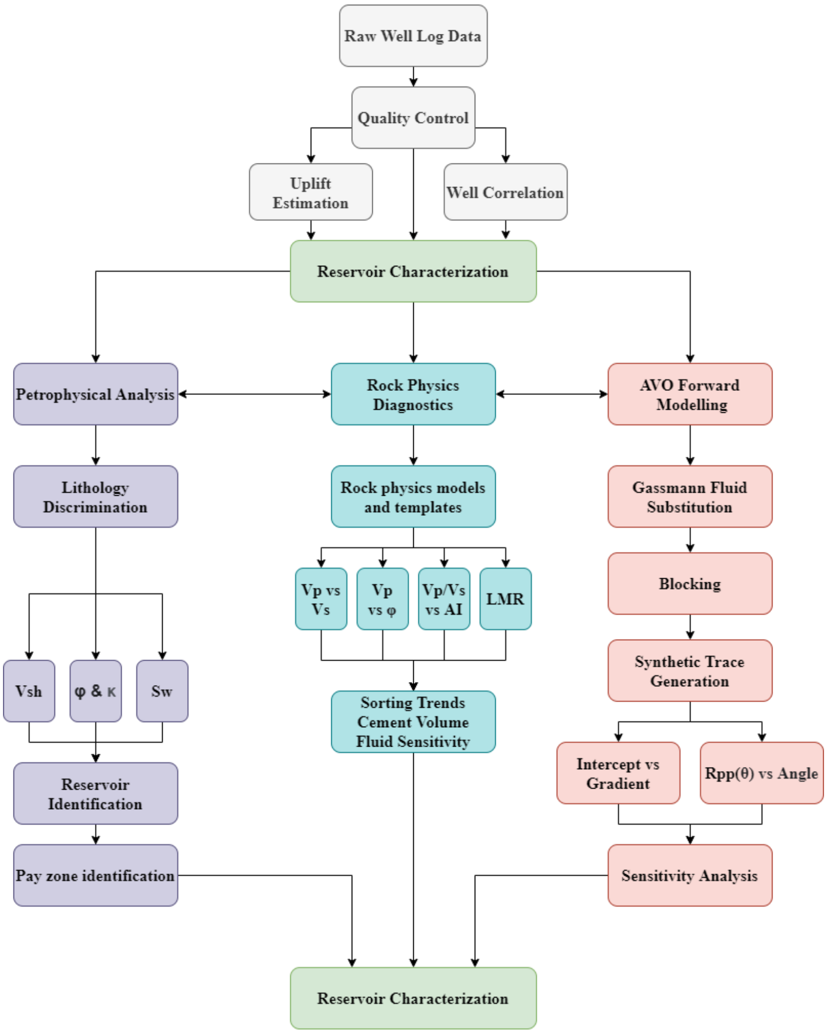

Figure 3.1: Workflow followed in this study.

3.2 Uplift Estimation

The porosity at deposition is wildly different for sandstones and clay/shale. Shales are deposited with a porosity of $60 - 80\%$, being quickly reduced by mechancial compaction processes from the overburden. Sandstones are usually deposited with a porosity of $36 - 40\%$ being more resilient to mechacnical compaction due to a more spherical shape of the grains. (Bjørlykke, 2015a; Simm et al., 2014)

Compaction regimes are divided into two groups: mechanical and chemical. Mechanical compaction occurs in the upper part of the strata where the loading from the overburden crushes the grains, repacks them and roatetes them. As the porosity decreases, the rock becomes denser, the bulk modulus (K) increases and the impedance increases. (Bjørlykke, 2015a)

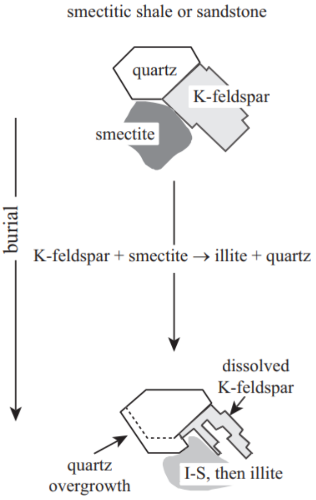

Figure 3.2: Figure from Lanson et al., 2002

The compaction regime changes abruptly to a chemical compaction domain when the temperature reaches $70 - 80°C$ (see fig 3.2). At this temperature, smectite becomes unstable and dissolves creating illite and quartz precipitaion. (Bjørlykke, 2015a)

The transition zone between mechanical and chemical compaction is usually very clear from inspecting V_P as just $2 - 4\%$ of quartz cementation can heavily increase the stiffness of the rock resulting in a huge spike in seismic velocities (Bjørlykke, 2015a). Estimation of uplift can be done by fitting the P-wave with with empirical formulas derived from lab measurements called NCT (Normal Compaction Trends. This study utilized the Mondol et al., 2007 to estimate the uplift and an example can be showing in fig 3.3. All wells estimated for uplift and transition zone is found in A.

Fitting empirical formulas of P-wave with increasing stress with the P-wave from the well logs yields an estimated uplift. Additionally, the transition zone between mechanical and chemical compaction can be identified by the abrupt increase in P-wave from the mechanical compaction trend.

The geothermal gradient is computed from the bottomhole temperature of the well log, and linearly approximated with equation

$$G = \frac{\Delta T}{\Delta z} = \frac{T_{BHT} - T_{OB}}{Z_{BTH} - Z_{OB}} \cdot 100° \tag{3.1}$$

where BHT is the bottom hole temperature and OB is the ocean bottom which in this study is set to 4°.

The findings of the uplift and the estimated temperaterue calculated by 3.1 are shown in table 3.1. All uplift and transition zone estimations are shown in A.

Uncertainties and comments about the uplift estimation and transition zone identification are

- Mechanical compaction trends may be used in accordance with the lithology in the study area.
- Formations containing carbonate occuring in the range of the transition zone may distort the V_P log, as carbonates have higher V_P than sillisiclastic sediments.

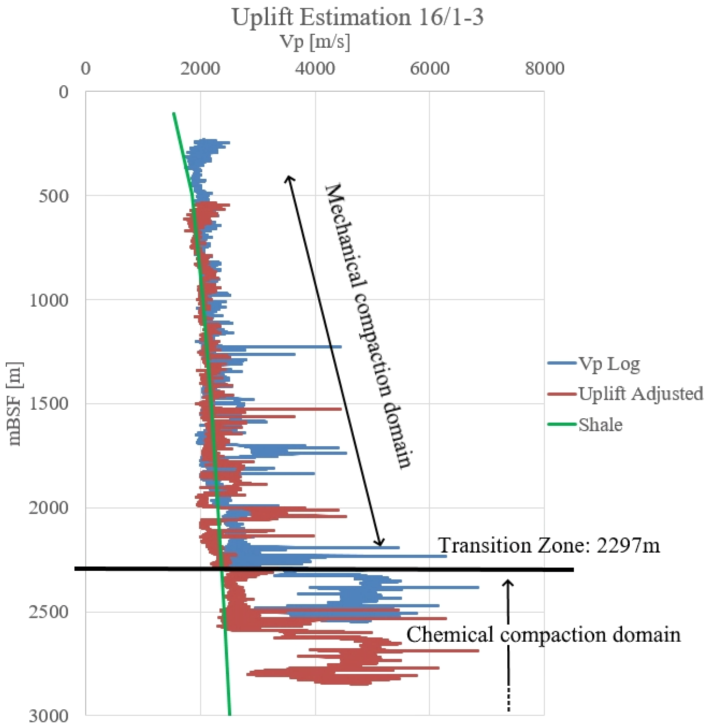

Figure 3.3: Example of fitting a V_P log with normal compaction trends from Mondol et al., 2007

Table 3.1: Uplift findings for all wells in the dataset. For interpretation of figures see A.

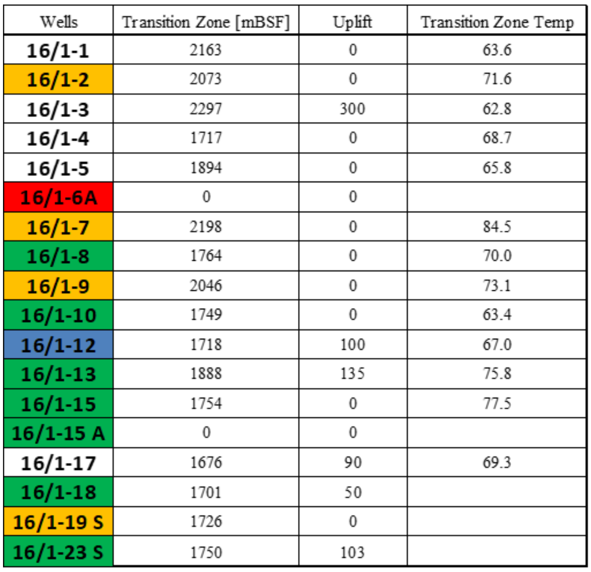

Wells	Transition Zone [mBSF]	Uplift	Transition Zone Temp
16/1-1	2163	0	63.6
16/1-2	2073	0	71.6
16/1-3	2297	300	62.8
16/1-4	1717	0	68.7
16/1-5	1894	0	65.8
16/1-6A	0	0	
16/1-7	2198	0	84.5
16/1-8	1764	0	70.0
16/1-9	2046	0	73.1
16/1-10	1749	0	63.4
16/1-12	1718	100	67.0
16/1-13	1888	135	75.8
16/1-15	1754	0	77.5
16/1-15 A	0	0	
16/1-17	1676	90	69.3
16/1-18	1701	50	
16/1-19 S	1726	0	
16/1-23 S	1750	103	

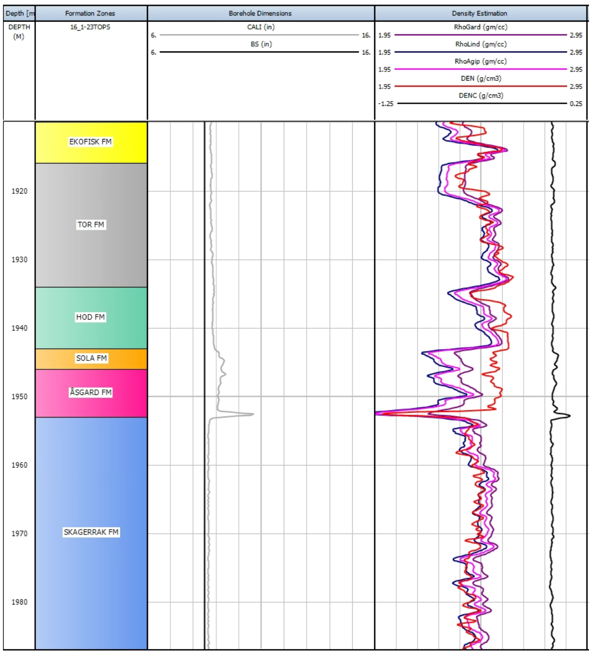

Figure 3.4: Excerpt from Interactive Petrophysics showing caving in the log as the caliper exceeds the bit size. Density estimations is procured to help combat the bad borehole environment.

- Some wells do not contain sufficent Vp coverage for uplift estimation to be sound.
- The uplift estimation with laboratoric mechanical compaction trends, while giving quantitative answer, are based on visual estimations and may therefore be treated as a qualitative measurement.

3.3 Quality Control of well logs

This subchapter covers how poor log data is identified and dealt with in order for a proper analysis and modelling of the well log data. Bad boreholes will be identified by the use of caliper log and density correction log.

Washouts can be identified from the caliper and density correction logs. The density and transit sonic log are very sensitive to bad borehole conditions, but the use of Gardner's equation (explained more in chapter 3.4.1.4) does help remove the underestimation (Simm et al., 2014). Identified bad log intervals are either omitted or fixed with substition depending on the availibility of estimation of the specific log.

3.4 Petrophysical Analysis

Petrophysical analysis is used to evaluate reservoir properties and hydrocarbon occurence in subsurface rocks on a fine scale. The sampling rate of the well log data included in this study is around ≈ 8 observations per meter, in stark contrast to seismic data which may only have a vertical resolution of around 10m (Yilmaz, 2001).

With well logs, which are measurements of geophysical quantities, one can establish good estimates for porosity, water saturation, permeablitiy and shale content. Along with lithology discrimination, identification of cap rock, reservoir rock and source rock can be conducted. Additionally information about the stratigraphy, depositional environment can also be uncovered.

Well logs are gathered by probes measuring resistivity, transit traveltime of both compressional and shear waves, wellbore dimensions, induced *and* passive radioactivity of formations of the walls of the well. These measurements can then be further altered by using mathematical relations along with empirical properties to give petrophysical quanties e.g. porosity and shale content. Comparing the estimated quantities with more precise measurements from cores and cutting done in laboratoric environments is crucial for maintaining valididty of the interpretation. (Mondol, 2015b)

This subchapter will explain the methods used for conducting the petrophysical analysis of the well log data. Firstly covering lithology discrimination with the use of shale volume, then fluid content estimation with fluid content estimation and finally permeability estimation in the target reservoir area.

3.4.1 Lithology Discrimination

For lithology discrimination there exists neutron-density log, gamma log, photoelectric log and spontaneous potential log. The spontaneous was not available in this study.

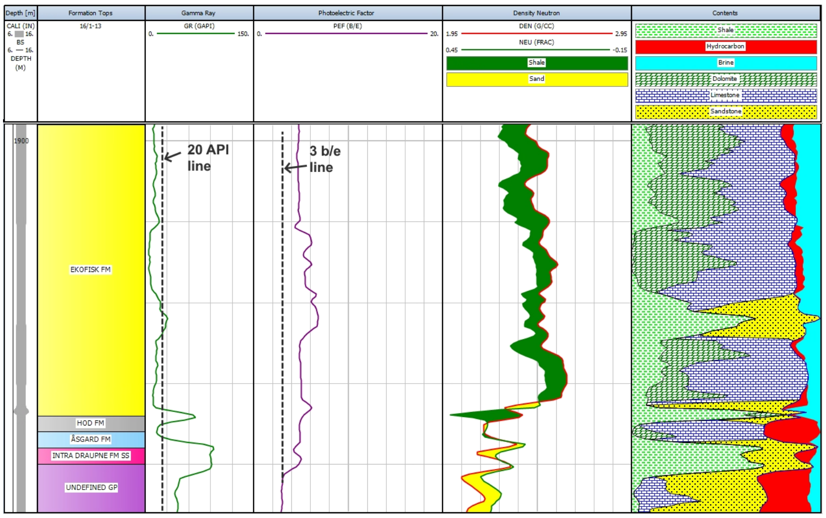

Figure 3.5: Figure showing the main logs providing lithology discrimination from well 16/1-13. Gamma ray, photoelectric factor and density-neutron combination with baselines and the resulting lithology, porosity and fluid content estimation computed in Interactive Petrophysics.

3.4.1.1 Gamma Ray Log

The gamma ray log, denoted as GR, is a high resolution log which records the natural gamma ray emissions in the borehole. It is measured in units API (American Petroleum Institute) (Mondol, 2015b; Rider, 1999)

The two gamma ray log tools availible are the standard gamma ray log and the spectral gamma ray log. The spectral gamma ray log decomposes the radiation into three main components: potassium (^{40}K), uranium (^{238}U,^{234}U,^{235}U) and thorium ^{232}Th (Klaja and Dudek, 2016)

High gamma ray readings indicate shales as clay contains radioactive isotopes, while low gamma ray readings may indicate reservoir rocks such as silisiclastic sandstones or calcerous lithologies such as dolomites and limestones. Organically rich shales very high gamma readings as they have abundant of uranium.

Depositional patterns can also be inferred by some extent from the GR log. The grain size is somewhat correlated with the gamma ray reponse as finer particles are more clay dominated. Gradual changes, either serrated or smooth, can therefore help give a better picture of the depositional environment (Mondol, 2015b).

Figure 3.6 from Mondol, 2015b shows different possible interpretations given different gradual GR logs. Cylindrical shapes indicate that the deposition was uniform with little deviation in shalyness with possible depositional facies being tidal sands, fluvial or turbidite sands, proximal deepsea fan or aeolian dune. "Bell shape" shows decreasing GR with depth, indicating an upwards fining response owing to point bars, fluvial channels, braided streams, turbidite channels, deltaic distributaries, proximal deep-sea fans , tidal- and alluval sand deposits. Funnel shapes are upwards coarsening and are deposited as crevasse splays, barrier bars, beaches, distrbutary mouth bars, distal deep-sea fan or delta marine fringes (Mondol, 2015b).

Smaller grains are often due to being containing clay, and so information about the depositional regime can be qualitatively established. Serrated GR trending to lower values indicating a (Mondol, 2015b)

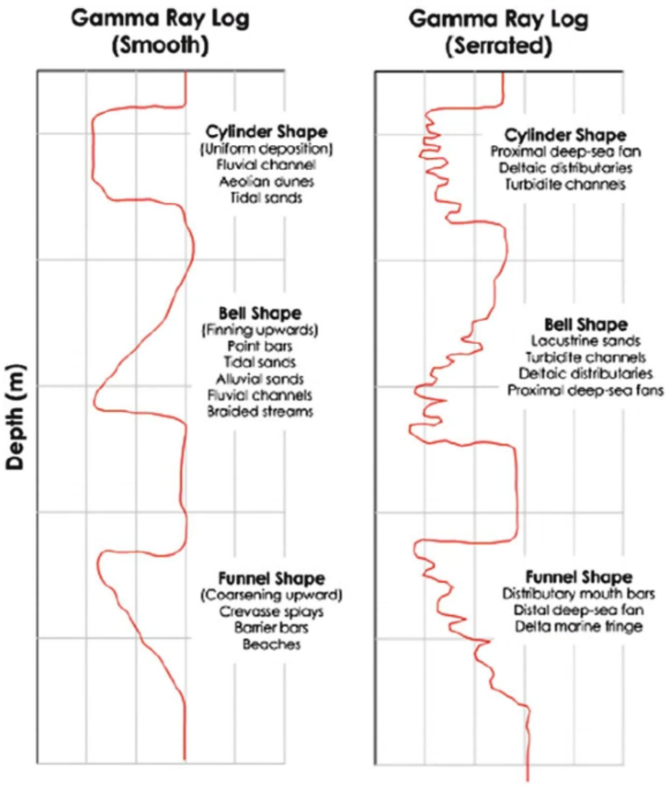

Figure 3.6: Figure showing different depositional environments and facies interpreted from GR log. Figure from Mondol, 2015b.

3.4.1.2 Spectral Gamma Ray

Spectral gamma ray are three logs which record Uranium (ppm), Thorium (ppm) and Potassium (%). Occurence of uranium in the regular gamma ray log negatively influences the estimation of shale rocks. Chlorite, glauconite, illite, kaolinite and smectite are five clay minerals which are of special interest for petroleum petrophysics (Klaja and Dudek, 2016).

Ratios of the spectral gamma logs can provide information about the clay minerals present. Th/U can provide information about the depositional environment and oxidation regime during deposition (Klaja and Dudek, 2016). The following ratios of Th/K are defined below and also shown in the Potassium (%) vs Thorium (ppm) space in fig 3.7.

- $Th/K < 0.6$ - Feldspars
- $0.6 < Th/K < 1.5$ - Glauconite
- $1.5 < Th/K < 2.0$ Micas
- $2.0 < Th/K < 3.5$ - Illite
- $3.5 < Th/K < 12$ - Mixed-Layered
- $12 < Th/K$ - Chlorite/Kaolinite

Glauconite is formed on the seabed in periods of low clastic input, indicating a marine shelf environment (Bjørlykke and Jahren, 2015).

The Th/U ratios indicate if the deposition was continental or marine and the oxidizing/reducing conditions. The classisifications from Klaja and Dudek, 2016 are:

- $Th/U > 7$ - continental environment, oxidizing conditions

- $Th/U < 7$ - marine environment
- $Th/U < 2$ - marine black shales, reducing conditions

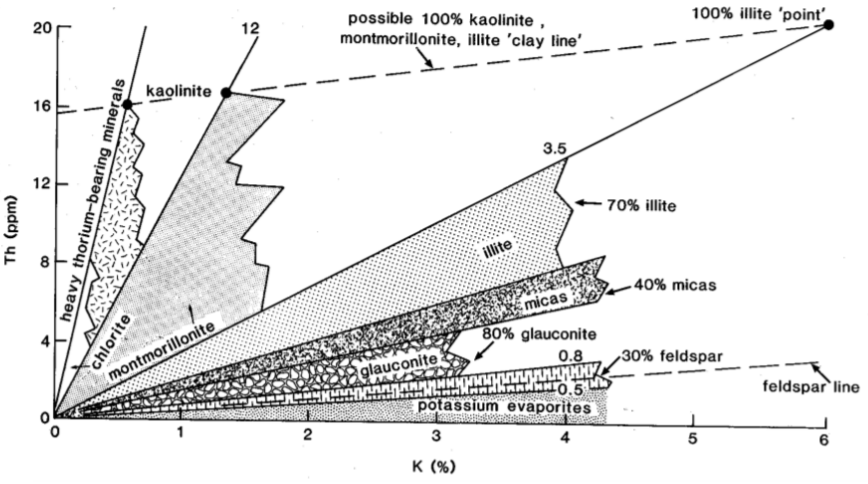

Figure 3.7: Thorium (ppm) vs Potassium (%) overlay for mineral identification. Figure from Glover, 2013.

3.4.1.3 Photoelectric Log

Logging density with a litho-density tool (LDT), there are two sensors: one measures the high energy gamma rays are also recorded, resulting in the addition of the photoelectric log. The photoelectric log is displayed in barns/electrons (b/e), where 1 barn = 10^{-24}cm^2, and ranges from 0 to 10 b/e. The photoelectric log is not dependent on the porosity or the fluids within the rock, but is sensitive to the mean atomic number of the formation and is therefore helpful for the lithology discrimination. (Mondol, 2015b)

Typical PEF responses are shown in table 3.2, with numbers from Bertozzi et al., 1981.

Table 3.2: Different PEF responses for lithologies. Numbers from Bertozzi et al., 1981

Lithology	PEF [b/e]
Quartz	1.80
Calcite	5.10
Dolomite	3.10
Shale	3.42

3.4.1.4 Density Estimation

For gaps in the data, density can be estimated by empirical equation based on the compressional velocity V_P with units km/s and comperssional slowness DT, with units us/ft. Different equations for estimating density is showing in table 3.3.

Table 3.3: Density estimations from literature. V_P (compressional velocity) is in units m/s and Δt (sonic transit time) is in units μ s/ft.

Author	**Equation**
Gardner et al., 1974:	$\rho = 0.23 V_P^{0.25}$
Bellotti et al., 1979, unconsolidated:	$\rho = 3.28 - \frac{\Delta t}{89}$
Bellotti et al., 1979, consolidated:	$\rho = 2.75 - 2.11 \frac{\Delta t - 47}{\Delta t + 200}$
Lindseth, 1979	$\rho = \frac{V_P - 3460}{0.308 V_P}$

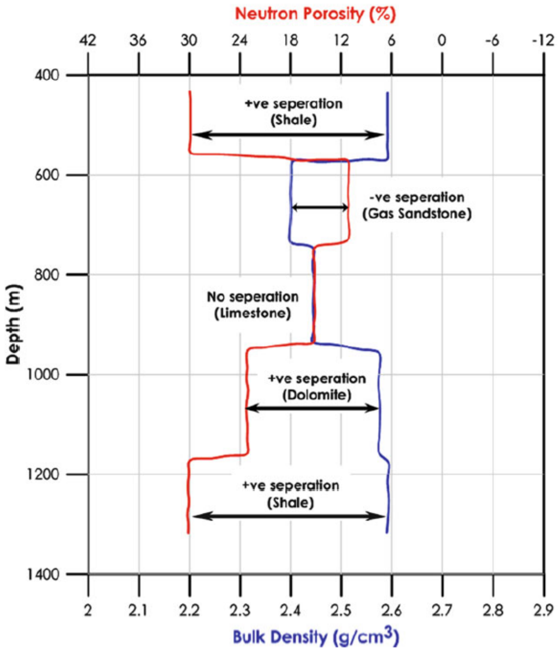

Figure 3.8: Neutron-density crossover for different lithologies all having 15% porosity. It is scaled for limestone as it shows no separation. Figure from Mondol, 2015b, modified from Rider, 1999

3.4.1.5 Neutron-Density

Neutron logs is recordings of neutrons emitted at a high velocity. The more hydrogen the more absorption and yields lower recordings. This is recorded back and gives is used to estimate Hydrogen Index. As water has more hydrogen that the surrounding rocks, the neutron log will be correlated to the porosity of the rock. Shales will give higher porosity as clay minerals contains more hydrogen than sandstones, called the shale effect. Oppositely, occurrences of gas in the pore spaces will result in a lower neutron porosity reading as gas contains less hydrogen per volume, called the gas effect (Mondol, 2015b).

The density log is measured by inducing gamma radiation into the formation rock and measuring the returning response with both short and long spaced detectors. The high energy returning gamma rays from Compton scattering help determine bulk density. If the formation rock has a high density, a high number of electrons scatter and attenuate the gamma rays resulting in a high gamma ray count recorded by the detectors, and opposite for a formation with lower density (Mondol, 2015b).

The neutron-density combination is a plot the density log over the neutron density log. They are both scaled for porosity of a given lithology. A clean-limestone scale assumes that the neutron porosity is 0 when the density is equal to the density of limestone, $2.70 g/cc$ [2], and when the neutron porosity is 100% that the density is 1.0 g/cc. (Rider, 1999) Different neutron-density combination responses to lithologies are shown in fig 3.8. A positive separation occurs with shale as the shale factor will yield a high neutron reading and a large bulk density. Occurences of gas will reduce the density and neutron porosity (due to gas effect) and called a negative separation. Limestone will not have a separation as the combination log is scaled for limestone (Mondol, 2015b).

3.4.1.6 Vsh Estimation

Gamma log can be used for shale volume estimation, V_{sh}, where one establishes the mean of both the lowest, “sandstone”-line readings, GR_{min}, and the highest, “shaly”-line, readings. (Mondol, N. H., 2015). Using these in the relationship from Mondol (2015) to create the Gamma Ray Index.

$$I_{GR} = \frac{\mathrm{GR}_{log} - \mathrm{GR}_{min}}{\mathrm{GR}_{max} - \mathrm{GR}_{min}} \tag{3.2}$$

---

[2] Pure calcite has a density of 2.71 g/cc

It should be noted that these “shaly/sandstones”-lines can change throughout the well and need to be estimated multiple times with care.

To calculate the V_{sh} one would then either assume a linear relationship, i.e. V_{sh}=I_{GR}, or use non-linear lower bounds showwed in table 3.4. These formulas for V_{sh} are also shown in figure fig:vsh with the values for $IGR = 0.5$ highlighted.

Table 3.4: Non-linear V_{sh} estimation equations from literature.

Author	**Equation**
Larionov, 1969 Young Rock:	$V_{sh} = 0.083 \cdot (2^{3.71 I_{GR}} - 1)$
Larionov, 1969 Old Rock:	$V_{sh} = 0.33 \cdot (2^{2 I_{GR}} - 1)$
Stieber et al., 1970:	$V_{sh} = I_{GR}/(3 - 2 \cdot I_{GR})$
Clavier et al., 1971:	$V_{sh} = 1.7 - \sqrt{3.38 - (I_{GR} + 0.7)^2}$

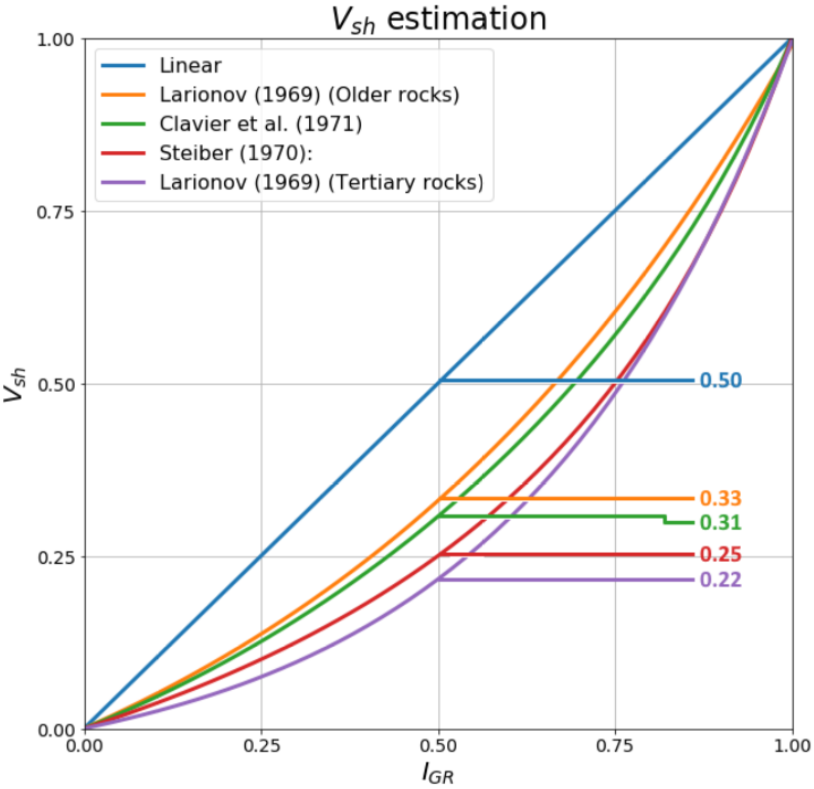

Figure 3.9: Plot showing the different equations Table 3.4 for estimating V_{sh} from I_{GR}. Different values of the equations evaluated at $I_{GR} = 0.5$ are also showing in the figure.

3.4.2 Porosity Estimations

Porosity is the volumetric fraction of a rock volume which contains pore fluids. Porosity is separated by the parts that can move freely inside the rock (effecitve or connected porosity) and what cannot (ineffective porosity).

$$\phi = \frac{\rho_{ma} - \rho_b}{\rho_{ma} - \rho_f} \tag{3.3}$$

Where ρ_{ma} is the matrix density , ρ_f is the formation bulk fluid which is the immediately occurring fluid around the borehole, normally mud filtrate, and ρ_b is the measured, bulk density log. (Mondol, 2015b) The rock matrix density and pore fluid density needs to known to get the best identification of porosity. Typical density values are listed in table 3.5.

Porosity estimations from solely neutron or density does not give an accurate figure as they are prone to giving falsehoods with occurrence of gas and shale as explained in 3.4.1.5. Calculating a root

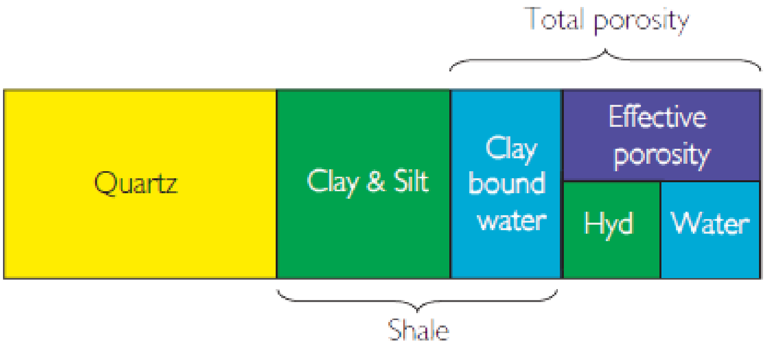

Figure 3.10: Diagram showing how the different constituents and liquid content compares to porosity and lithology in a shaly sandstone. Modified from Simm et al., 2014

Table 3.5: Density values for sandstone and different water in units g/cc. Modified from Asquith et al., 2004

	ρ_{ma}
Sandstone	2.648
Salt mud	1.1
Fresh water	1.0
Gas	0.7

mean square of these quantities would yields a better estimation (Mondol, 2015b; Rider, 1999) and is caluated as;

$$\phi_{ND} = \frac{\sqrt{\phi_N^2 + \phi_D^2}}{2} \tag{3.4}$$

where ϕ_N is the neutron density and ϕ_D is the neutron-density porosity.

From a petrophysical view a rock is comprised of four main constituents which are matrix, clay, water (brine) and hydrocarbon(shown diagrammatically in figure 3.10). The estimation of porosity is previously described only discriminating between volume of fluids compared to volume of rock. Shales which are mixed in with the sandstone carry water needs to be adjusted for to obtain the effective porosity. The effective porosity adjusts for the clay bound water and is calculated by

$$\phi_E = \frac{\rho_{ma} - \rho_b}{\rho_{ma} - \rho_{fl}} - V_{cl}\frac{\rho_{ma} - \rho_{cl}}{\rho_{ma} - \rho_{fl}} \tag{3.5}$$

where ϕ_E is the effective density, ρ_{ma} is the matrix density, ρ_b is the bulk density, V_{cl} is the wet clay volume, ρ_{fl} is the fluid density.

3.4.3 Sonic Transit Time Log

The sonic log records the travel time of an acoustic pulse through the rock. It thereby is affected by pore fluids, the cementation, compaction, pore distribution. It is usually recorded in slowness denoted as Δt, the inverse of velocity, and with units us/ft in the range of $40 - 140$us/ft (Mondol, 2015b) From the sonic log one can estimate the porosity of the formation by use of Wyllies time average equation

$$\phi_s = \frac{\Delta t_{log} - \Delta t_{matrix}}{\Delta t_f - \Delta t_{matrix}} \cdot \frac{1}{C_p} \tag{3.6}$$

Here the Δt_{log} is the measured interval transit time, Δt_{matrix} is the interval transit time of the matrix, Δt_f is the interval transit time fluid alone and C_p is the compaction factor. Typical values for the interval transit time of different rock matricies are shown in table ??.

Table 3.6: Compressional velocity and interval transit time for different rock matricies. Modified from Asquith et al., 2004

	V_{ma} **[km/s]**	Δt_{ma} μ**s/ft**
Sandstone	5.49-5.98	55.5 to 51.0
Limestone	6.4	47.7
Dolomite	7.0	43.5
Anhydrite	6.1	50.0
Salt	4.6	67.0

The compaction factor C_p is calculated by

$$C_p = \frac{\Delta t_{sh} \cdot C}{100} \tag{3.7}$$

where Δt_{sh} is the interval transit time of an adjacent shale and C is a constant which usually equals 1.0.

With the presence of hydrocarbons, the sonic-log derived porosity can overcompensate. An adjustment is madeby Hilchie (Asquith et al., 2004):

$$\phi = \phi_s \cdot 0.7 \quad \text{(gas)} \tag{3.8}$$

$$\phi = \phi_s \cdot 0.9 \quad \text{(oil)} \tag{3.9}$$

3.4.4 Water Saturation Estimation

Saturation is the fraction of a given fluid type in the pores of a porous rock. The fluid content can be either brine, oil or gas. It is normal to express the saturation of the pore fluid by the water saturation, S_w, as the hydrocarbon saturation is equal to $S_h = 1 - S_w$.

Resistivity is an electric propertiy (units $\Omega - m$) that measures the the given materials ability to resist flow of an electric current. As rock grains and matrix is highly non-conductive conductive clay types? , the resistivity log becomes almost entirely a function of the porefluids (Asquith et al., 2004). In a borehole, it is recorded by

The resisitvity log is measured by passing a known electrical current through the formation and recorded by (Mondol, 2015b)

The Resistivity log is helpful discriminating fluid content as most rocks are good insulators which results in the electric current flowing through the pore spaces. Resistivity is the inverse of conductivity, and is measured between 2 and 4 electrodes in the borehole wall.

When drilling, drilling mud is being pumped into the well to overcome the formation pressure, resulting in intrusion into the borehole wall. There are three zones of indicating the level of intrusion. The flushed zone is where the all the native fluid have been replaced with the drilling mud, the invaded zone where there is a partial mix, and the uninvaded zone which only contains the native fluid. The resistivity of the drilling mud is important to know as it affects the resistivity measured in the flushed and invaded zone. Freshwater based mud yields a higher resistivity reading (Mondol, 2015b)

Archies first equation is based upon the estimation of the formation factor F, satisfying:

$$R_0 = F \cdot R_w \tag{3.10}$$

where R_0 is the resistivity of the rock and R_w is the resisitvity of the formation water. The formation factor can be calculated by eq. 3.11.

$$F = \frac{a}{\phi^m} \tag{3.11}$$

Where$a$ is the turtuosity factor which is a function of the complexity of the fluid path in the rock, (Asquith et al., 2004), m is the cementation exponent which varies with grain size and grain size distribution and ϕ is the porosity of the rock. With the formula for estimating the resisitvity of the brine saturated rock, R_0, Archies 3rd equation (eq. 3.12) shows how to calculate the water saturation S_W as a function of the measured resistivity R_t

$$S_w^n = \frac{R_0}{R_t} \tag{3.12}$$

Combining equations 3.10, 3.11 and 3.12 and solving for S_W gives Archie's Law:

$$S_W = \left(\frac{a}{\phi^m}\frac{R_w}{R_t}\right)^{\frac{1}{n}} \tag{3.13}$$

Where S_W is the saturation, a is the tortuosity factor, ϕ is the porosity, n is the saturation exponent, R_w is the resistivity of the formation water and m is the cementation exponent. The saturation exponent is commonly set to $n = 2$. The cementation exponent indicates the increase in resistivity due to the pore network. Typically for consolidated sandstones this lies between $1.8 < m < 2.0$. The tortuosity factor is the square root of tortuosity which is a measure of the fluid path through a rock. (Mondol, 2015b)

Archie's law have problems is a naive approach but robust. The requirements of 3 unknown parameters, a, n and n, to solve for one value may provide heavy uncertainties. (need citation for this argument)

3.4.4.1 Net-to-gross

There exists widely used terminology to describe rocks ability to store and transmit fluids, defined upon thickness and thickness rations. (Worthington and Cosentino, 2005) The terminologies are explained below and can be schematically seen in 3.11.

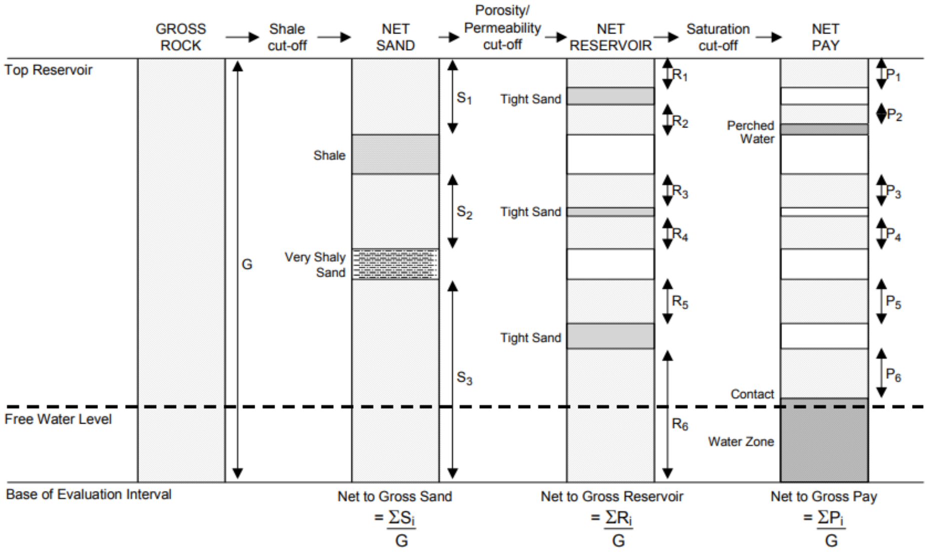

Figure 3.11: Figure from Worthington and Cosentino, 2005

- Gross - the total volume of the rock inside the evaluation interval. As this study only contains one-dimensional borehole data, volume and height will be equivalent.
- Net sand - the sum of rocks that may have reservoir properties inside the evaluation interval. Sand is meant to represent clean sedimentary rocks, with the cutoff parameter being V_{sh}.
- Net reservoir - the sum of rocks that do have reservoir properties inside the evaluation interval. This is calculated by using porosity, ϕ, or additionally permeability, k, as cutoff parameters on the net sand intervals such that net-reservoir is a rock capable of storing and transmitting hydrocarbons.

Table 3.7: Proposed cut-off values from Worthington and Cosentino, 2005

Lithology	Cut-off parameter	Range of values
Sandstones	V_{sh}	$0.3 - 0.5$
	ϕ	$0.06 - 0.08$
	S_w	$0.5 - 0.6$

- Net pay - the sum of rocks that have both reservoir properties and contains hydrocarbons. Pay is calculated applying a satisfactory value of S_h ($S_h = (1 - S_w)$) on all the "net reservoir" intervals. The name "pay" has evolved from not only being a description of the rock itself, but to carry an economical aspect as whether the rock can be economically produced from
- Net-to-gross - the thickness ratio of the net intervals and the gross. It can be calculated by either of the sand, reservoir or pay intervals.

For a sandstone reservoir, proposed cutoff values are shown in table **??**

3.4.5 Permeability prediction

Permeability is the measurement of how well a fluid can flow through a medium. Evaluating permeability in a target pay zone is important for assessing the productivity of the area. Darcys law (Darcy, 1856) is defined as

$$Q = -k\frac{A}{\mu}\frac{\Delta P}{L} \tag{3.14}$$

Where Q is the flow rate, k is the permeability, A is the cross section, mu is the viscosity, ΔP is the pressure difference over the length of the medium, L. The permeability k has units of m^2 but is commonly shown with the unit Darcy (1 Darcy = $0.986923 \cdot 10^{-12} m^2$) or milliDarcy (1000 mD = Darcy). For an intuitive understand of the unit Darcy can calculate a water saturated rock permeability of 1 Darcy, a pressuregradient of 0.1 MPa/cm to yield a 1 cm/s flow rate (Mavko et al., 2009).

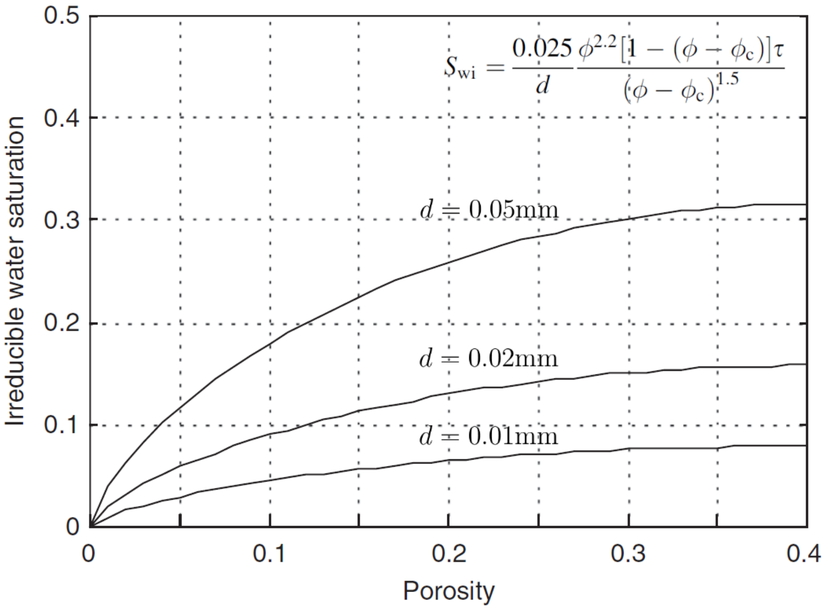

Figure 3.12: The irreducible water saturation as a function of porosity, plotted for three pore throat sizes, d = $0.05, 0.02 and 0.01$mm. Tortuosity τ is set to 2. Figure modified fromMavko et al., 2009

The Kozeny-Carman equation for permeability (κ_{KC}) is given in 3.15.

$$\frac{\kappa_{KC}}{d^2} = \frac{10^9}{72} \frac{(\phi - \phi_c)^3}{[1 - (\phi - \phi_c)]^2 \tau^2} \tag{3.15}$$

d is the pore throat size, τ is the tortuosity (length of flow path over length of sample), and ϕ and ϕ_c are the porosity and the critical porosity.

Some qualitative measurements are possible from the resistivity and caliper log (evaluating how far the mud filtrate penetrates the rock wall), however absolute measurements are only ever possible with lab measurements of cores extracted from the well.

The equations used for estimating permeability is shown in table **??** with constants fitted for the desired fluid, oil or gas. The recurrent idea of these equations are that the permeability is inversely proportional to the irreducible water saturation, S_{wirr}, which is the lowest water saturation a rock can obtain when oil and gas are displacing the water. Smaller grain sizes have thinner capillaries resulting in larger capillary forces and an increased S_{wirr}. This is in figure 3.12 by combining the Kozeny-Carman equation (eq 3.15) and Darcy's Law (eq 3.14) and plotting for different pore sizes.

Qualitative estimates of permeability can also be done by looking at separations in logs. Separation of R_t and R_x give indication the penetration of mud filtrate when hydrocarbons are present.

Table 3.8: Equations from literature used to estimate permeability. Equations are from *Crain's Petrophysical Handbook* 2021

Author/Name	**Equation**
Timur (1968) :	$k = 10^4 \phi_e^{4.5} / S_{wirr}^2$
Logarithmic- linear for sandstones	$\log_{10} k = C \log_{10} \phi_e + D$
Wyllie-Rose formula (Timur Parameters):	$k = 3400 \phi_e^{4.4} / S_{wirr}^2$

3.5 Rock Physics Diagnostics

Rock physics is the important link between seismic and reservoir properties. This chapter will explain in part how to calculate the fundamental elastic parameters and delve into the rock physics trends and templates. Rock physics templates are displayed as crossplots, with seismic properties plotted over each other to help give insight into the effects of porosity, sorting, pore pressure, cementation, lithology and fluid content on the seismic properties. These templates are meant to aid in the description of petrophysical analysis, but characteristics from the templates

The rock physics templates need to be calibrated with the basin play, but the direction a rock takes in the crossplot given a certain scenario remains the same (Avseth, Mukerji et al., 2010).

3.5.1 Fundamentas / Calculation of elastic parameters

Elastic parameters explains how a medium react when stress is exerted upon it. The bulk modulus, K, describes the change in volume when stress is applied, defined as (Simm et al., 2014)

$$K = \frac{S}{\Delta V / V} \tag{3.16}$$

The Shear modulus, μ, describes the rigidity of the rock when tangiental stress is applied, defined as

$$\mu = \frac{\text{shear stress}}{\text{shear strain}} \tag{3.17}$$

Most fluids do not have any resistance to shearing and thereby it is assumed that the shear modulus is zero (Simm et al., 2014).

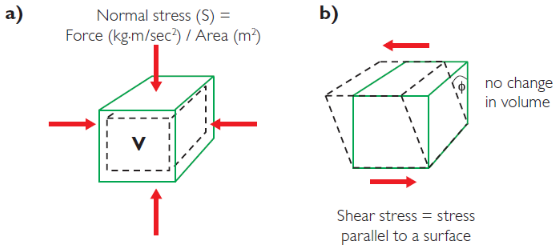

Figure 3.13: Figure showing volume and shape changes due to stress being excerted upon an idealized cube. a) shows the bulk modulus K, where stress compresses the volume, whereby b) shows tangiental stress causing shape change and no change in volume. Figure from Simm et al., 2014

Compression and shearing in a borehole environment are measured through V_P and V_S, with the following equations (Simm et al., 2014):

$$V_P = \sqrt{\frac{k + 4/3\mu}{\rho}} \tag{3.18}$$

(3.19)

$$V_S = \sqrt{\frac{\mu}{\rho}} \tag{3.20}$$

The particle motion relative to the propagation direction for these body waves can be seen in figure 3.14

Rearranging 3.18 with respect to K and μ gives Simm et al., 2014

$$K = \rho \left(V_P^2 - \frac{4}{3} V_S^2 \right)$$

$$\mu = \rho V_S^2$$

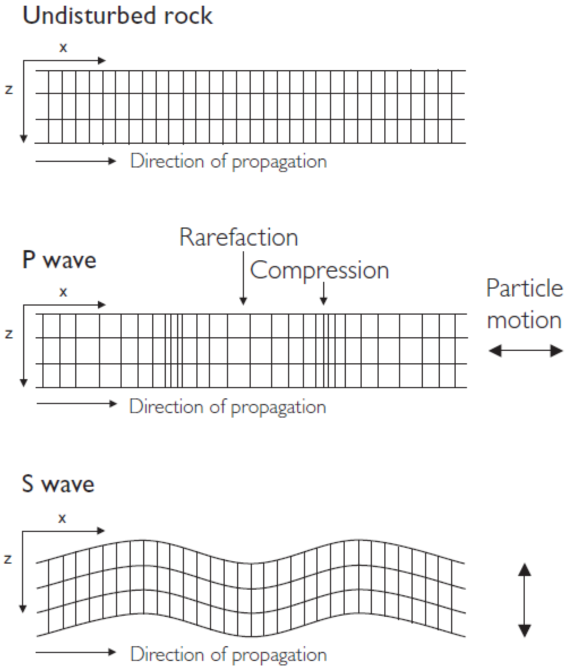

Figure 3.14: Figure showing the propagation direction and particle motion of P-wave (compression) and S-wave (shearing). Simm et al., 2014

Poisson's ratio, ν, is a measure of the fractional change in width divided by the fractional change in length under uniaxial compression (Simm et al., 2014)

$$\nu = -\frac{\text{Transverse strain}}{\text{Longitudinal Strain}} = -\frac{\Delta w/w}{\Delta l/l} \tag{3.21}$$

The poissions ratio can also be expressed in terms of log measured quantities and elastic components:

$$\nu = \frac{\frac{1}{2}\left(\frac{V_p}{V_s}\right)^2 - 1}{\left(\frac{V_p}{V_s}\right)^2 - 1} \tag{3.22}$$

$$\tag{3.23}$$

$$\nu = \frac{2K - 2\mu}{2(3K + \mu)} \tag{3.24}$$

Quartz have a lower V_P/V_S ratio than most other minerals, making silisiclastic sandstones having lower poissons ratio than shales. Rocks containing hydrocarbons have a lower V_P (especially gas) and slightly higher V_P resulting in the bulk rock having a much lower Poissons ratio than if the rock was water bearing (Simm et al., 2014).

As rock physics is the bridge between reservoir properties and seismic properties, the rock formation is viewed as an effective medium. As the scale of seismic is indifferent to grain sizes and pore geometries, an effective medium can be calculated to simulate the same seismic results with less degree of complexity. To create an effective medium, the physical quantities such as density and bulk modulus of all the different constituents contained in the rock needs to be known. These constituents can be either water saturation, S_w, porosity, ϕ, and their counterparts such as hydrocarbon saturation, $(1 - S_w)$, and rock matrix $(1 - \phi)$.

The effective density of a rock can be calculated by a weighted average of the density constituent as seen in eq. 3.25.

$$\rho_{\mathrm{b}} = \phi\rho_f + (1 - \phi)\rho_g \tag{3.25}$$

And the density of the fluids can also be calculated by using the a weighted average

$$\rho_{fl} = S_w \rho_w + (1 - S_w)\rho_{hc} \tag{3.26}$$

Where ρ_{fl} is the density of the fluids, S_w is the water saturation, ρ_w is the density of brine and ρ_{hc} is the density of hydrocarbons.

3.5.2 Empirical models and V_s prediction

For some of the logs, see the table nr, no V_s data is not available. This raises the importance of V_s estimation, where equations from literature are commonly used (see 3.9). These methods are mostly linear relations between V_p and V_s, with parameters like shalyness and porosity being predetermined.

Table 3.9: Vs prediction equations from literature

Author(s)	**Description**	**Equation [km/s]**
J. P. Castagna, M. L. Batzle et al., 1985	Mudrock equation	$V_s = 0.862V_p - 1.172$
J. P. Castagna and Backus, 1993	Clastic rock	$V_s = 0.804V_p - 0.856$
Krief et al., 1990	Wet sand	$V_p^2 = 2.213V_s^2 + 3.857$
Krief et al., 1990	Gas sand	$V_p^2 = 2.282V_s^2 + 0.902$
Krief et al., 1990	Shaly Sand	$V_p^2 = 2.033V_s^2 + 4.894$
Han et al., 1986	Clay < 25%	$V_s = 0.754V_p - 0.657$
Han et al., 1986	Clay > 25%	$V_s = 0.842V_p - 1.099$
Han et al., 1986	Shaly sand, $\phi < 15\%$	$V_s = 0.764V_p - 0.662$
Han et al., 1986	Shaly sand, $\phi > 15\%$	$V_s = 0.853V_p - 1.137$
Greenberg and J. Castagna, 1992	Sandstone	$V_s = 0.804V_p - 0.856$
Greenberg and J. Castagna, 1992	Shale	$V_s = 0.770V_p - 0.867$

Han et al., 1986 provides equations providing V_P data dependant on porosity and clay content for different effective pressures. They are shown in table 3.10. The main findings of the was that increasing clay content reduces the V_P of the rock. Care should be taken into consideration as the Han et al., 1986 equations were fitted to laboratoric data which does not always transfer to rocks with differing lithologies.

Table 3.10: Table showing Han et al., 1986 clay equations, fitted for different effective pressures. C is the clay content.

Effective Pressure	V_P [km/s]
40 MPa	$V_P = (5.59 - 2.18C) - 6.93\phi$
30 MPa	$V_P = (5.55 - 2.18C) - 6.96\phi$
20 MPa	$V_P = (5.49 - 2.17C) - 6.43\phi$
10 MPa	$V_P = (5.39 - 2.02C) - 7.08\phi$
5 MPa	$V_P = (5.26 - 2.02C) - 7.08\phi$

3.5.3 Theoretical bounds

For mixtures of different rock constitutents, theoretical bounds are useful for displaying the range physical properties. The two most primitive mixing bounds are the Voigt and Reuss bounds (see fig. 3.17 for geometric intuition). A Voigt average assumes that all the layers are strained equally as the load axis is coming in parallel with the layering. This distributed the load axis and will yield the upper bound as it is effectively governed by the elastic moduli of the hardest layer. With the iso-strain case, the load axis is perpendicular to the layering and the stress is therefore equally distributed.The straining of the layers will differ as the softest layers will have more impact on the elastic moduli, thereby making this a lower bound.

For practical purposes, a further average of the bounds make a good estimation for a wanted elastic moduli (Avseth, Mukerji et al., 2010). The equations for these two bounds can be found in figure 3.17 and in table 3.11.

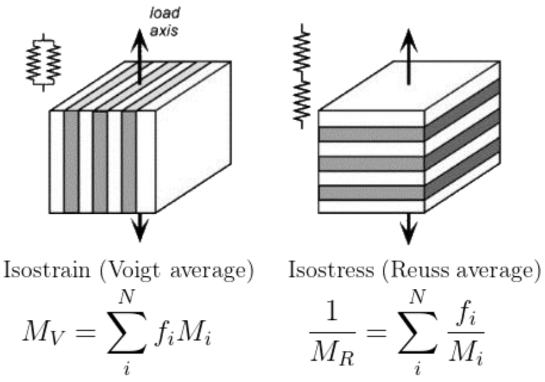

Figure 3.15: Geometric interpretation of the Voigt and Reuss bounds. The dark and the lighter colored layers represent harder and softer materials. Under the isostrain, every layer is experiencing the same amount of straining due to the load axis being distributed equally on the layers, as pointed out in the small figure in the upper left corner. In the isostress, all the layers are experiencing the same amount of stress from the load axis, but is the straining will differ in the harder and softer layers. Modified from Omar et al., 2016

Table 3.11: Mixing laws from literature (Avseth, Mukerji et al., 2010). The Voigt-Reuss-Hill average is an average of the upper and lower bound.

Author	**Equation**
Voigt (arithmetic mean):	$M_V = \sum_i^N f_i M_i$
Reuss (harmonic mean):	$\frac{1}{M_R} = \sum_i^N f_i \frac{1}{M_i}$
Voigt-Reuss-Hill:	$M_{VRH} = \frac{M_V + M_R}{2}$

Hashin Strick Man bounds are the narrowest theoretical bounds without speciyfing anything about the geometry of the individual constituents other than spherical grains. (Avseth, Mukerji et al., 2010) They are given as

$$K^{HS\pm} = K_1 + \frac{f_2}{(K_2 - K_1)^{-1} + (K_1 - 4\mu_1/3)^{-1}} \tag{3.27}$$

$$\mu^{HS\pm} = \mu_1 + \frac{2f_2}{(\mu_2 - \mu_1)^{-1} + 2f_1(K_1 + 2\mu_1)/[5\mu_1(K_1 + 4\mu_1/3)} \tag{3.28}$$

Where f is the volumetric fraction of the constituents, and K and μ are the respective bulk and shear moduli of the constiuents. The upper bound is found by subscripting the stiffest material to 1 and the lower bound with the softest material as 2 (Avseth, Mukerji et al., 2010).

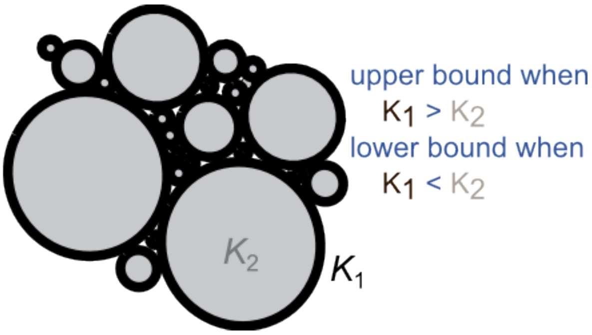

Figure 3.16: Geometrical representation of the Hashin-Shtrikman bounds. All grains are assumed spehrial with varying radius. SubSurfWiki, 2021a

3.5.4 Contact models

For rocks in the subsurface, the porosity of the rocks is a

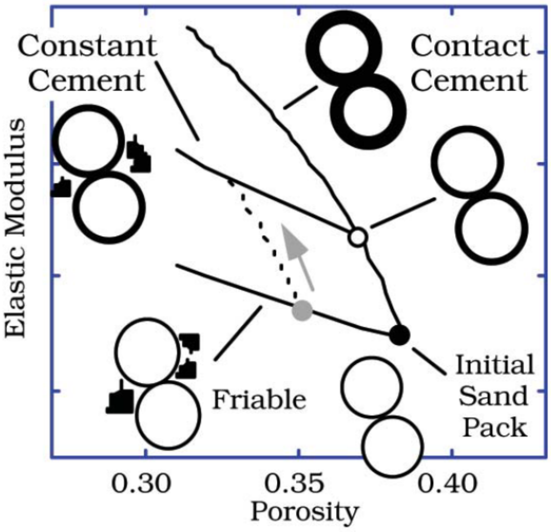

Figure 3.17: Contact models visualized graphically with the modelled grain contacts shown. Friable sand displays the sorting trend where grains are passively added into the porespaces, the Contact-Cement shows the diagenesis trend where uniformly increasing cement around the grains are the porosity reducing factor. The Constant Cement line starts at a fixed point of contact cement where grains are passively added into the porespaces. Figure from Avseth, Jørstad et al., 2009a

The friable-sand model, introduced by Dvorkin and Nur, 1996, describes how V_p, V_s or any other value dependant on the bulk moduli, changes with deteriorating sorting. The end member, typically around critical porosity $\phi_c = 40$ % , represents well sorted packing where the elasticity is defined at the grain contacts. Deteriorating sorting is defined in this model by adding smaller grains in the porespaces. The end member of critical porosity to 0% porosity is interpolated using the lower Hashin-Shtirkamn bound (see eq. 3.27), giving the heuristical argument that passively filling the porespaces with grains is the softest way of stiffening the rock. (Avseth, Mukerji et al., 2010)

For the dry, well sorted end member, Hertz-Mindlin theory (Mindlin, 1949) gives the dry rock elastic moduli

$$K_{HM} = \left[\frac{n^2(1-\phi_c)^2\mu^2}{18\pi^2(1-\nu)^2}P\right]^{\frac{1}{3}} \tag{3.29}$$

$$\mu_{HM} = \frac{5-4\nu}{5(2-\nu)}\left[\frac{3n^2(1-\phi_c)^2\mu^2}{2\pi^2(1-\nu)^2}P\right]^{\frac{1}{3}} \tag{3.30}$$

where ϕ_c is the critical porosity (porosity where grains are no longer in contact), P is the effective pore pressure, ν is the poissions ratio and n is the coordination number.

The coordination number is the average number of grain contacts per grain, and can be approximated by porosity (Muprhy, 1982)

$$n = 20 - 34\phi + 14\phi^2 \tag{3.31}$$

The end member is then interpolated from ϕ_c towards 0% porosity by the lower Hashin-Shtrikman bound:

$$K_{dry} = \left[\frac{\phi/\phi_c}{K_{HM}+4\mu_{HM}/3} + \frac{1-\phi/\phi_c}{K+4\mu_{HM}/3}\right]^{-1} - \frac{4}{3}\mu_{HM} \tag{3.32}$$

$$\mu_{dry} = \left[\frac{\phi/\phi_c}{\mu_{HM}+z} + \frac{1-\phi/\phi_c}{\mu+z}\right]^{-1} - z \tag{3.33}$$

where $z = \frac{\mu_{HM}}{6}\left(\frac{9K_{HM}+8\mu_{HM}}{K_{HM}+2\mu_{HM}}\right)$.

The contact cement mode, or "cement sand model", was the solution of a contact problem solved by Dvorkin, Nur and Yin, 1994. With burial, a sandstone will notice cementation in between grains and this model assumes the cementation is acting uniformly around the sand grains. The reinforcement of grain contacts by cementation will drastically increase the bulk moduli of the rock, and therefore small changes in porosity will have a great impact on bulk moduli (and physical values dependant on the bulk moduli like V_p and V_s. A more detailed explanation of the equations are found in Dvorkin, Nur and Yin, 1994.

The constan cement model is a model introduced by Avseth, Dvorkin et al., 2000. It is, mathematically, a mix between the friable sand- and the contact cement model as it is modelling passively adding grains in the porespaces with the sand grain matrix already containing a fixed amount of constant cement uniformly covering the grains. The maxmimum porosity end member is found along the contact cement line and interpolated towards 0% porosity by using the friable-sand model. Mathematically, the procedures remains the same as for the friable sand model, substituting the Hertz-Mindlin endpoint with the contact cement model.

3.5.5 Gassmanns' equation

Gassmann equation (Gassmann, 1951) is a robust equation for modelling fluid substitution in a rock. By knowing the porosity effective bulk moduli of fluid saturated rock, the bulk moduli of the mineral, dry rock frame and the in-situ fluid, one can calculate the new bulk moduli by using the equation:

$$K_{sat} = K_{dry} + \frac{\left(1-\frac{K_{dry}}{K_m}\right)^2}{\frac{\phi}{K_{fl}}+\frac{1-\phi}{K_m}-\frac{K_{dry}}{K_m^2}} \tag{3.34}$$

$$\mu_{sat} = \mu_{dry} \tag{3.35}$$

K_{sat} is the fluid saturation bulk modulus, K_{dry} is the dry, matrix bulk modulus, K_m is the bulk modulus of the mineral grains, K_{fl} is the bulk modulus of the fluid to be substituted in and ϕ is the porosity. As the shear modulus is indifferent to fluids it remains unchanged. If the fluid that is going to be substituted in is comprised of different fluid types, this would be computed as an effective bulk modulus of the fluid content. The K_{dry} and μ_{dry} also needs to be calculated from the bounds described in 3.5.3. Figure 3.18 shows a schematical figure comparing the complexities of a real rock (Scanning Electron Microscope from Mahmic et al., 2018) at a small level to a modelled grain stucture with a more primitive texture and identical grains. At a more macroscopic level, there are negligible differences between the two representations of the rock.

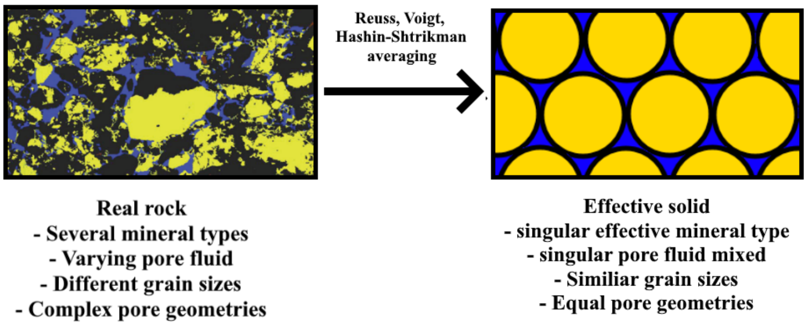

Figure 3.18: Left hand side showing Scanning Electron Microscope from the conglomerate from the Skagerrak Formation from Mahmic et al., 2018. The sorting is poor, with multiple grain minerals, complex pore structure and varying porefluid. Right hand side showing an idealized model with simpler grain minerals, similar pore structure and.

The change in density due to fluid substitution is done by

$$\rho_b^{new} = \rho_b^{old} - \phi(\rho_f^{old} - \rho_f^{new}) \tag{3.36}$$

Gassmann subsitution is a robust equation, in that there are some caveats which should be followed, but does not give highly unreasonable results when disobeyed (Avseth, Mukerji et al., 2010). The limitations are given in M. Batzle and Wang, 1992 as:

- Closed rock - Assumed that there is no flow in or out of the rock body.
- Interconnectivity - All porespaces are assumed connected and have free movement to distribute the fluids.
- Low frequency - The wave induced pore pressures have time to reach equilibrium during a seismic period.
- Isotropic rocks - the bulk moduli are the same in every direction of the rock. Rocks are always at least slightly anisotropic but using the Gassmann equation on the measured V_p and V_s values yield satisfactory results.
- Homogeneous mineralogy - Assumed that the whole rock body shares the same shear and bulk moduli. Usually, an average between the upper and lower Hashin-Shtrikman bounds is used (equation 3.27).
- The saturation of the pore fluid is equally distributed. The effective bulk moduli of the fluid is computed by the Reuss average, and the effective fluid density by the Voigt average.
- The fluids wholly fills the pore spaces and is frictionless, i.e. low viscosity.

3.5.6 Construction of rock physics templates (RPTs)

Rock physics templates (RPTs) to evaluate fluid and lithology was popularized by Avseth and Odegaard, 2004, mainly by the V_P/V_S vs AI crossplots. The RPTs are basin specific and needs to be fitted to different basins as different temperature, burial depth and pressure, lithology and mineralogy controls the RPT overlays.

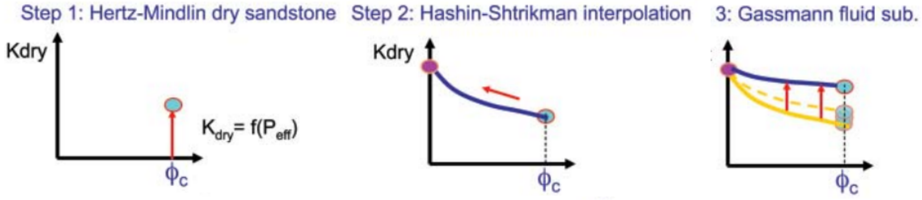

Figure 3.19: Step by step recipe for rock physics templates generation. Starting with the Hertz-Mindlin theory end point, interpolated to the 0 porosity end member and finally saturated by use of the Gassman equation. For more detail of the equations see 3.5.4 and 3.5.5. Modified from Avseth, Jørstad et al., 2009b

Figure 3.19 shows the stepwise generation of the rock physics templates. First the point of critical porosity is calculated by employing Hertz Mindlin contact theory on the dry grains under a calculated effective pressure. Then the Hashin-Sthrikman bounds are calculated on decreasing porosity until the bounds reach the mineral point of 0% porosity. The lower Hashin-Sthrikman bound dictates the looses way to reduce porosity and indicates that the porosity reduction is due to sorting, while the upper Hashin-Sthrikman bound is the stiffest way to reduce porosity and is coupled with cementation. Lastly the gassmann fluid substitution is employed by substituting in the different pore fluid compositions. The figure shows the generation of a RPT generated for a K vs ϕ crossplot, but is also valid for V_P/V_S vs I_P crossplots, where differing hydrocarbon saturation gives multiple points.

For the calculation of the inital K_{DRY} calculated from the Hertz-Mindlin contact theory, typical values can be used from literature. These are shown in the table 3.12

3.5.6.1 Porosity vs Elastic Moduli

Crossplot of porosiy versus elastic moduli (K or μ) or values dependent on elastic moduli (AI, V_P, V_S) are very helpful for understanding what porosity reduction in the sandstones are geologically goverened

Table 3.12: Elastic properties for different solid minerals (Simm et al., 2014)

	Bulk Modulus (GPa)	Shear Modulus (GPa)	Density (g/cc)	V_P (km/s)	V_S (km/s)	Poisson's ratio
Quartz	36.6	45.0	2.65	6.038	4.121	0.064
Clays (approx)	41.0	17.0	2.68	4.900	2.500	0.324
Calcite	76.8	32.0	2.71	6.640	3.436	0.317
Dolomite	94.9	45.0	2.87	7.347	3.960	0.295

by. The lower and upper Hashin-Shtrikman bounds displays the softest and stiffest way to reduce porosity. Porosotiy reduction with sorting is the softest, while cementation (diagenesis) of the grains is the stiffest. Dependent on the initial degree of

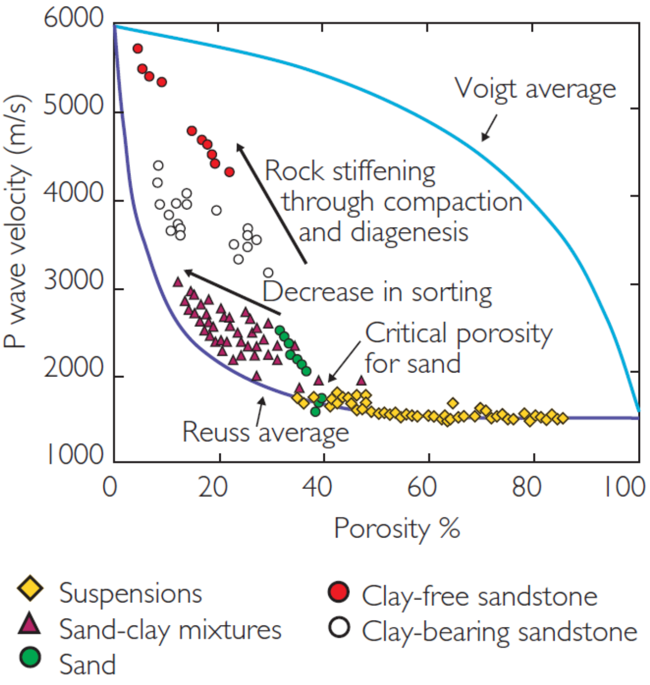

Figure 3.20: Porosity vs P-wave crossplot with data from Han et al., 1986, **yin1992** and Hamilton, 1956. The Voigt average indicates the stiffest way to reduce porosity, and is an upper bound for porosity reduction related to compaction and diagenesis, meanwhile the Reuss average indicates the softest way to reduce porosity due to differences in sorting of the grains. Figure from Simm et al., 2014

The friable sand and constant cement model is assumed to fill the porespaces with the same mineralogy as the rock matrix. Experiments in using different lithologies such as clay was done by Marion et al., 1992. The increasing clay volume generated a very specific response in the V_P vs ϕ crossplot (see figure 3.21, where increasing clay was added to the volume until the porespace was filled. When the porespace is filled up, increasing clay content begins to remove the contacts of the quartz grains resulting in the matrix going from grain suppoerted to clay supported, decreasing the V_P. The porosity will also see a slight increase in this region due to the bound porewater in the added clays.

3.5.6.2 V_P/V_S vs AI

The V_P/V_S vs AI is a rock physics template proposed by Avseth and Odegaard, 2004. It is a crossplot of V_P/V_S and AI, the acoustic P-wave impedance, superimposed with the overlays of the mineral points of reservoir rocks such as quartz with incremental increases in porosity and water saturation as shown in figure 3.22. It aids in quality controlling the petrophysical interpretation visually. V_P/V_S as a good lithology and fluid indicator.

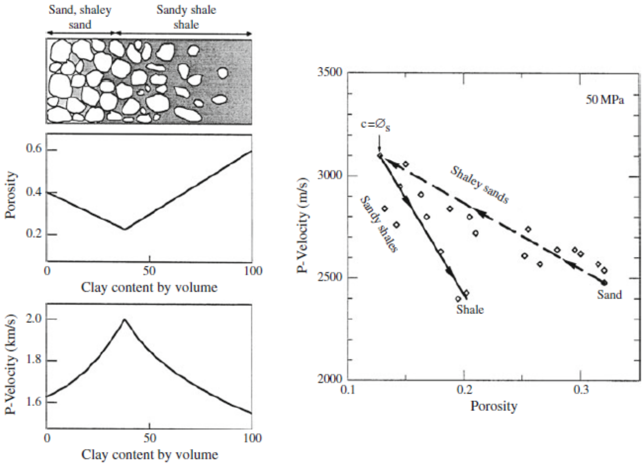

Figure 3.21: Increasing shale content leaves a distinctive inverted V shape, signalling that rock has gone from a grain supported to a clay suppoerted matrix. Figure from adapted from Avseth, 2015; Marion et al., 1992

Gas decreases V_P dramatically due to low bulk modulus. It does not affect the shear modulus but does however decrease the overall bulk modulus of the rock, making the V_S slightly larger. Both these effects on the seismic velocities bring the V_P/V_S ratio lower. The acoustic impedance is the product of density and V_P and is therefore mostly sensitive to porosity

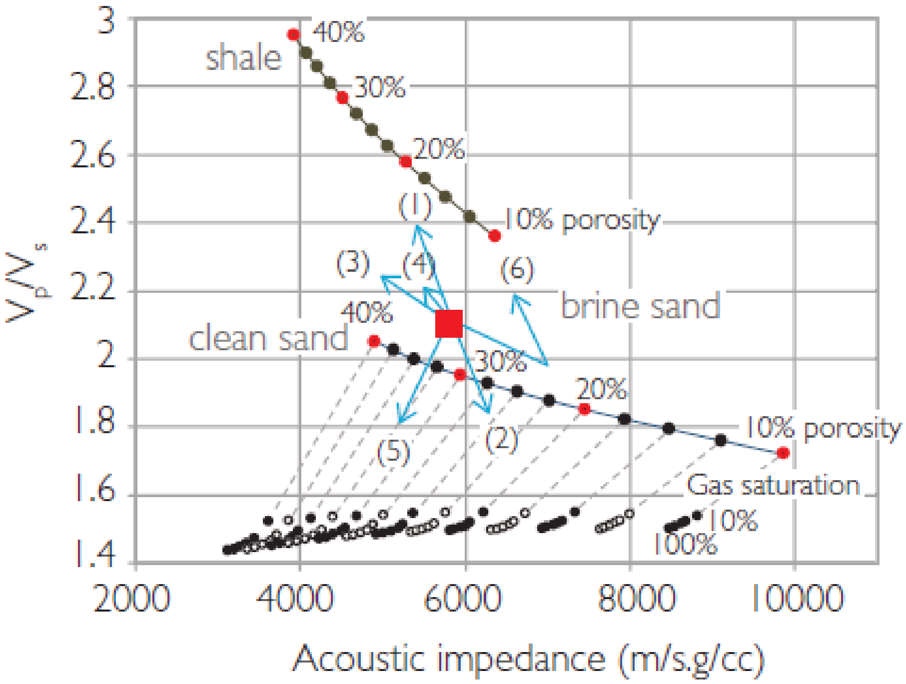

Figure 3.22: Rock physics template of the V_p/V_s vs AI cross plot (Simm et al., 2014). The different trend responses for a typical brine filled sandstone are (1) increase in shalyness, (2) increase in cementation , (3) increase in porosity, (4) decrease in effective pressure, (5) increase in hydrocarbon saturation and (6) increase in dispersed shale content

In figure 3.22, the red box indicates an idealized rock data point and shows trendlines increasing effect of different scenarios. Increasing shalyness (1) will move the rock to the shale line, increasing cementation (2) will decrease the porosity of the rock and strengthen the rock resulting in lower V_P/V_S and AI, increase in porosity (3) will move the rock along the increasing porosity line, decreasing effective pressure (4) will give a slight increase in both V_P/V_S and AI, increasing hydrocarbon saturation will, especially for gas, greatly lower V_P/V_S ratio and somewhat AI and finally increased dispersed shale content will reduce the porosity until a certain level of shale is reached when the rock starts moving towards the shale trend (Avseth and Odegaard, 2004).

The template shown in figure 3.22 assumes a quartz dominated sand, but the sands can also be feldspar rich (Arkose) which yields different curves. The overlay is computed by Hertz-Mindlin contact theory at critical porosity and extrapolated towards mineral point by using the lower Hashin-Shtrikman bound and Gassmann's equations to substitue in different pore fluids. The overlays are therefore basin dependent as the effective pressure, mineralogy and temperature needs to be accounted for when cross plotting.

3.5.6.3 LMR

LMR is a crossplot template by Goodway et al., 1997 (shown in figure 3.23) which can help determine lithologies and gas saturations from measured rock properties. LMR stands for Lambda Rho vs Mu Rho ($\lambda\rho \times \mu\rho$), where λ is Lamé's first parameter $\lambda = K - 2/3\mu$ and μ is the shear modulus. Both are multiplied with the density, ρ.

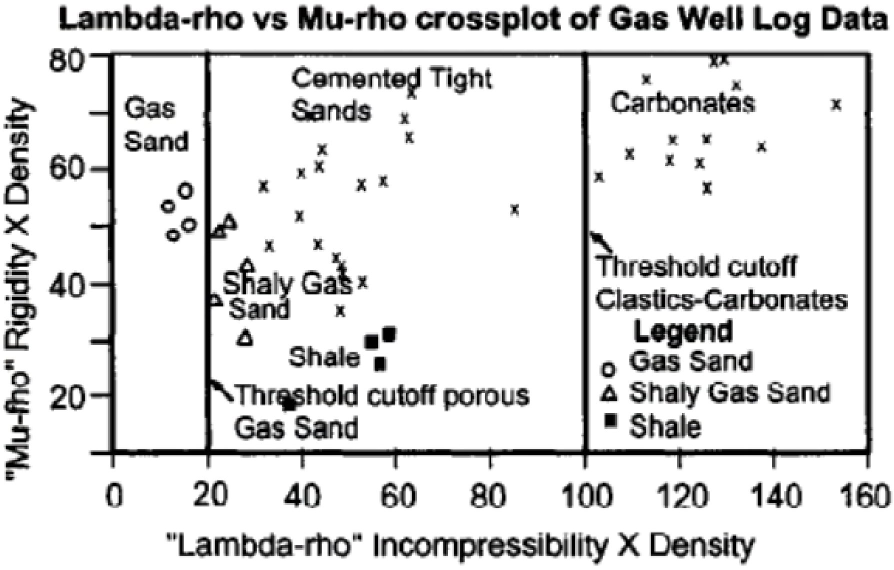

Figure 3.23: Template for From Goodway et al., 1997

$$\lambda\rho = I_P^2 - 2I_S^2 \tag{3.37}$$

$$\mu\rho = I_S^2 \tag{3.38}$$

The $\lambda\rho$ term is a measure of the incompressibility, while $\mu\rho$ measure of the rigidity. The LMR aids in fluid discrimination as well as a lithology identifier. A figure showing the different cutoff values for estimating lithology and pore fluid content is shown in figure 3.23. With different lithologies having different elastic moduli, typical lithology zones is spotted in the LMR crossplot. Shales have a low rigidity owing to its flaky geometry, while carbonates have a high rigidity and imcompressiblity (Simm et al., 2014). The degree of cementation in sandstones increases both the rigidity and incompressiblity. As gas does not influence the rigidity, they are separated by the thresholds defined by Goodway et al., 1997 at 20 $\lambda\rho$.

3.5.6.4 V_p vs V_s

The cross plot of V_P vs V_S is useful for displaying fluid effects, especially for gas, as it mainly displays the ratio of V_P/V_S. Comparing the data with background trends for the V_P vs V_S cross plot, see chapter 3.5.2 and table 3.9), outliers can be detected. Since V_S is indiscriminate for fluids and instance V_P is heavily influenced by the occurrence of gas, large inclusions of gas is easily visible in the data.

3.6 AVO

AVO (Amplitude variation with offset) is a phenomenon in seismic in which the amplitude on a boundary in the subsurface changes with increasing offset. It is was popularized nearly 40 years ago by Ostrander, 1984. The increases in amplitude follows a trend for porous, water bearing rocks and so datapoints in the seismic which have a separatation from this line are called AVO anomalies which can be a direct hydrocarbon indicator (DHI). AVO analysis can give insight into the porefluids and the lithology for a targeted information (Avseth, 2015).

AVO have had pitfalls in the past with lithological-, tuning- and overburden effects and have also been prone to errors with seismic processing and acquisition effects yielding a false positive. However in later years, 3D seismic have improved alongside with more S-wave logging, subsequently improving AVO analysis. (Avseth, 2015)

3.6.1 Fundamentals / Generation of a synthetic seismogram

A synthetic seismogram is created by convoluting a seismic pulse, wavelet, with the reflectance boundary co in the subsurface.

The equation for finding the P-wave reflectance for zero offset ($\theta = 0$) is given in 3.39. Z_i and ρ_i are the impedance and the density, respectively, of the layer of layer i. The P-wave reflectance can be either positive or negative, and will occur as a trough or a peak in the seismogram.

$$R(\theta = 0) = \frac{Z_2 - Z_1}{Z_2 + Z_1} = \frac{V_{P2}\rho_2 - V_{P1}\rho_1}{V_{P2}\rho_2 + V_{P1}\rho_1} \tag{3.39}$$

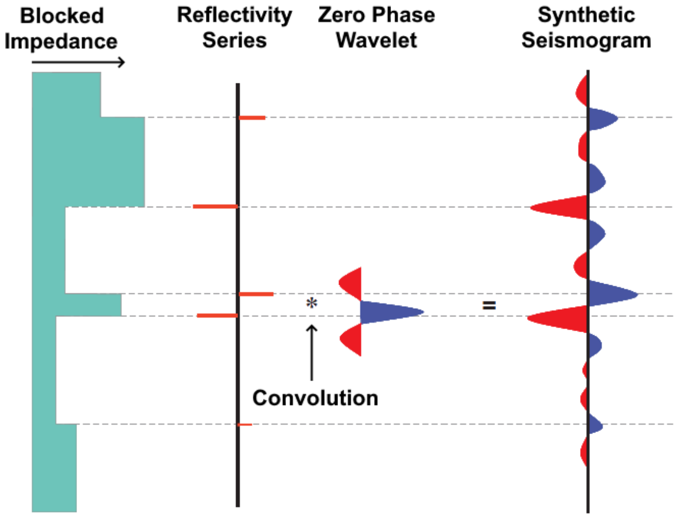

Figure 3.24: Figure showing the process of synthetic seismogram generation. The Modified from Simm et al., 2014

By using the density and P-wave velocities measurements from a well, one can construct the reflectivity series. After cleaning up and quality controlling the density and P-wave logs, multiplying them together returns the accoustic impedance for the borehole. By using the equation 3.39 one can compute the zero offset reflection series for the borehole, which finally is convoluted with a wavelet to generate the syntethic seismic. Usually the wavelet chosen is of great importance. Extraction and estimation of the wavelet from the seismic data is very critical to modelling (Simm et al., 2014). However in this study the Ricker wavelet will be used in the absence of seismic data.

Wavelet is a mathematical function which divides a function into frequency components that studies each component with a resolution that matches its scale (Mondol, 2015b). A wavelet is a transient signal, meaning it has finite duration. There are different wavelets with different characteristics. A symmetric wavelet with maximum at $t = 0$ is called a zero phase wavelet (Yilmaz, 2001)

Vertical resolution is the minimum thickness which can separate two events in seismic (Mondol, 2015a). It is calculated by the tuning thickness, $\lambda/4$, a fourth of the seismic wavelength related to the dominant frequency of the wavelet.

$$\frac{\lambda}{4} = \frac{1}{4}\frac{V_P}{F_d} \tag{3.40}$$

where F_d is the dominant frequency.

With increasing depth, seismic velocties increase but the dominant frequency will decrease as the earth acts like a filter. Typical ranges of V_P in the subsurface are between 2 to 5 km/s and 50 to 20 Hz for the dominant frequency F_d (Yilmaz, 2001). Tuning thickness for these ranges of values are shown in table 3.13.

Table 3.13: Adapted table from Yilmaz, 2001 displaying indicating the decrease of vertical resolution with depth.

V_P [m/s]	F_d [Hz]	$\lambda/4[m]$
2000	50	10
3000	40	18
4000	30	33
5000	20	62

Tuning effects can occur if the reflectors are too narrowly spaced from each other which creates interferences in the wavelets. This effect is commonly shown by using the wedge model (fig 3.25). With decreasing bed thickness of the wedge, the limit of vertical resolution is reached at the tuning thickness. The upper and lower boundary of the wedge is not possible to distinguish leaving, thereby overestimating the thickness of the wedge. At the tuning thickness the ampltide reaches its maxima before being vanishing due to destructive interference (Yilmaz, 2001).

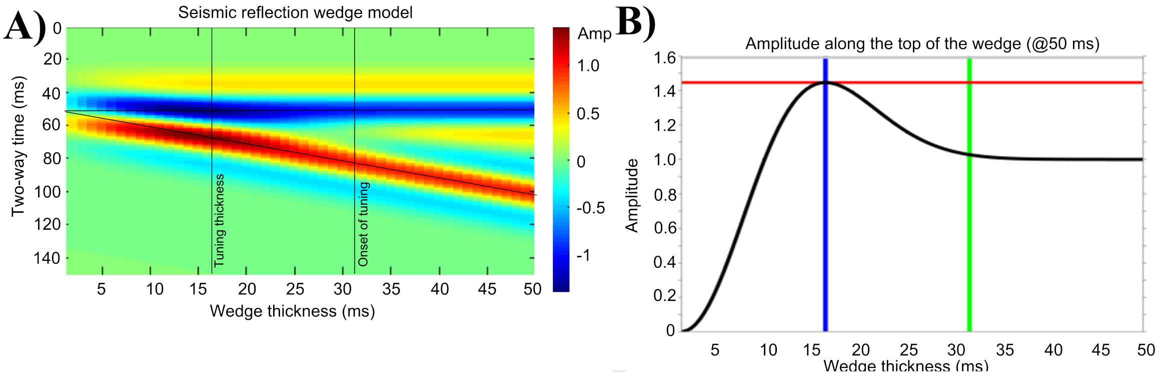

Figure 3.25: Figure showing the wedge model. A) 2D synthetic seismic is generated on a wedge with decreasing thickness. B) Ampltide of the wedge at the top of the reservoir, showing the constructive interference at tuning thickness before increasing destructive interference below the tuning thickness. Figure from SubSurfWiki, 2021b

Theoretically the tuning thickness is slightly larger than the vertical resolution (Simm et al., 2014).

3.6.2 Reflection Coefficient with Offset

The previous section 3.6.1, creation of zero offset synthetic was mainly discussed. However AVO is the change of amplitude with offset or angle. To display and interpret the results from AVO forward modelling, theoretic models for the reflectivity dependant on the angle is discussed below.

Assuming a surface between two solid media, an incident ray with incoming angle not equal to 0 will create four outgoing waves: A reflected P- and S-wave and a refracted P- and S-wave. The angles of these waves can be calculated by the use of Snells law Mondol, 2015a:

$$\frac{\sin\theta_1}{V_1} = \frac{\sin\theta_2}{V_2} = p \tag{3.41}$$

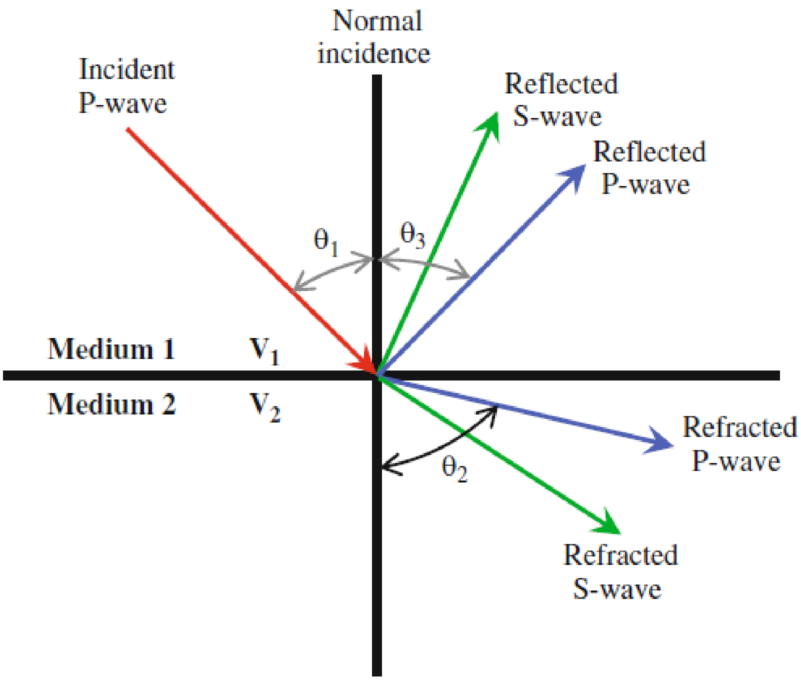

Figure 3.26: Figure showing the geometrical representation of Snells law (eq. 3.41. FromMondol, 2015a

Where V_1 and V_2 are the velocities in media 1 and 2m, θ_1 is the incidende of the angle within media 1, θ_2 is the angle of the refracted wave in media 2. The geometrical representation of this figure is shown in figure 3.26

The Zoeppritz equations (Zoeppritz, 1919) first gave a complete solution to explaining the change in amplitude with varying offset, but suffered from being complex and removed of intuitive, geophysical meaning (**avseth2014**). An approximation of the Zoeppritz equation is given by Richards and Aki, 1980

$$R(\theta_1) \approx \frac{1}{2}(1 - 4p^2 V_S^2)\frac{\Delta\rho}{\rho} + \frac{1}{2\cos^2\theta}\frac{\Delta V_P}{V_P} - 4p^2 V_S^2 \frac{\Delta V_S}{V_S} \tag{3.42}$$

The Δ-terms are calulcated as a difference between the upper and the lower medium at an interface (following the notation from figure 3.26). With no indexing on ρ, V_P or V_S, an average of the layers are computed as shown below:

$$\begin{aligned} p &= \frac{\sin\theta_1}{V_{P1}} & \theta &= (\theta_1 + \theta_2)/2 \approx \theta_1 \\ \Delta\rho &= \rho_2 - \rho_1 & \rho &= \frac{1}{2}(\rho_2 + \rho_1) \\ \Delta V_P &= V_{P2} - V_{P1} & \rho &= \frac{1}{2}(V_{P2} + V_{P1}) \\ \Delta V_S &= V_{S2} - V_{S1} & \rho &= \frac{1}{2}(V_{S2} + V_{S1}) \end{aligned}$$

A further approximation was done by Shuey, 1985, utilizing the same notation of mean and differences of the layers

$$R(\theta) \approx R(0) + G \cdot \sin^2\theta + F\left(\tan^2\theta - \sin^2\theta\right) \tag{3.43}$$

where

$$\begin{aligned} R(0) &= \frac{1}{2}\left(\frac{\Delta V_P}{V_P}\frac{\Delta \rho}{\rho}\right) \\ G &= \frac{1}{2}\frac{\Delta V_P}{V_P} - 2\left(\frac{V_P}{V_S}\right)^2\left(\frac{\Delta \rho}{\rho} + 2\frac{\Delta V_S}{V_S}\right) \\ F &= \frac{1}{2}\frac{\Delta V_P}{V_P} \end{aligned}$$

The F term in eq. 3.43 dominates at far offsets, but since the typical range of angles used in AVO analysis are less than 30°, the equation can further simplified to two terms (Shuey, 1985):

$$R(\theta) \approx R(0) + G \cdot \sin^2 \theta \tag{3.44}$$

3.6.3 Upscaling

To bridge the frequency gap between seismic and well log data, upscaling is required. There are different methods for scaling up the well log data for proper synthetic seismic to be generated. Well log data,

Backus average is essentially an averaging of the elastic moduli, instead of the seismic properties such as velocities. It calculates the M and μ properties from the equations $\mu = V_S^2\rho$ and $M = V_P^2\rho$, averaged over a given length. The averaging is done by using the Voigt bound (arithmetic average) for the density and Reuss bound (harmonic average) for the moduli (Simm et al., 2014). The procedure is therefore stepwise

- (1) Calulating the raw bulk modulus K and shear modulus μ from the V_P, V_S and ρ logs.
- (2) Finding the lower reuss bound (harmonic average) of K, μ and ρ in the intervals defined by the desired upscaling thickness.
- (3) Computing the upscaled V_P and V_S with the harmonically averaged logs of K, μ and ρ.

3.6.4 AVO Classification

This study will utilize single interface AVO plots. V_P, V_S and density ρ will be used to compute impedances around the boundaries, upscaled to a satisfactory scale and employed on the Zoepprtiz algorithm provided by the Hampson Russel Software TM. The output will be a fitted curved of the reflection coefficient dependent on the angle of offset.

The AVO response parametrized by the intercept and gradient can be crossplotted and then classified (see fig 3.27). A positive gradient means the reflection will increase with offset, while a negative gradient means the reflection will decrease with offset. The AVO classifications scheme is defined by Rutherford and Williams, 1989, with the class 4 being extended by J. P. Castagna and Swan, 1997 and are explained below.

3.6.4.1 Class 1 anomalies

Class 1 is characterized by high impedance sands, resulting in a large zero degree reflection with a negative gradient resulting in decreased reflection with increasing offset. With higher impedance than the overlying caprock, these sands are stiffly packed are heavily affected by compaction. The gradient is affected by the zero degree offset reflection and the difference of poission's ratio on the interface between shale and sandstone (Rutherford and Williams, 1989).

3.6.4.2 Class 2 anomalies

Class 2 sands have almost no impedance difference between the shale-sand interface and is typically moderately compacted. A polarity change can occur (denoted as a class 2p) if the zero degree reflection is greater than zero, as it characterized by a negative gradient. (Rutherford and Williams, 1989).

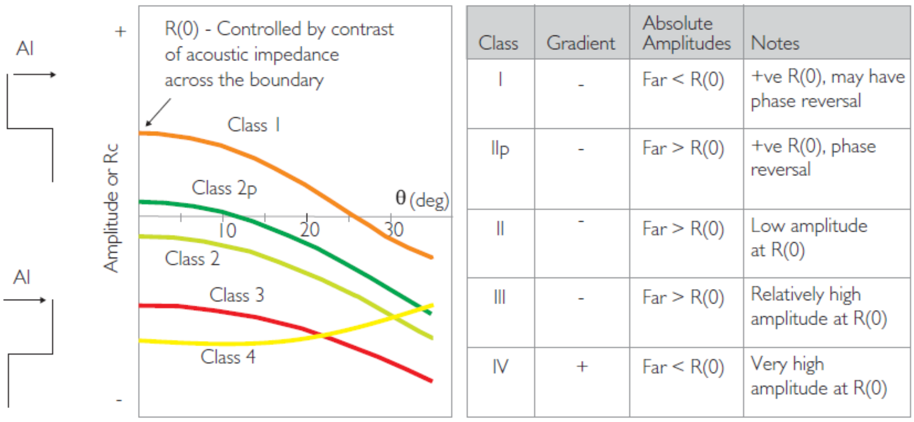

Class	Gradient	Absolute Amplitudes	Notes
I	-	Far < R(0)	+ve R(0), may have phase reversal
IIp	-	Far > R(0)	+ve R(0), phase reversal
II	-	Far > R(0)	Low amplitude at R(0)
III	-	Far > R(0)	Relatively high amplitude at R(0)
IV	+	Far < R(0)	Very high amplitude at R(0)

Figure 3.27: Figure showing showing different AVO classes. FromSimm et al., 2014

3.6.4.3 Class 3 anomalies

Class 3 sands are characterized by low impedance sands. These sands are shallower being unconsolidated and less compacted (Rutherford and Williams, 1989). Sands that generated class 3 avo anomalies are assosciated with bright spots, a direct hydrocarbon indicator in seismic surveying (Avseth, 2015).

3.6.4.4 Class 4 anomalies

Class 4 sands are sands with negative intercept but with a positive gradient. The postiive gradient is due to soft, gas saturated sands being overlain by stiff shales having a slightly greater V_P/V_S ratio than the underlying sand. It is relatively rare and sometimes assumed to be a false positive in seismic when identifiying bright spots **??**.

CHAPTER 4

Petrophysical Analysis

4.1 Results

This chapter contains the results of the petrophysical analysis carried out in Interactive Petrophysics. The targeted formations are mainly the Jurassic Sleipner formation and Triassic Skagerrak formation. The basement is also oil bearing on the Utsira High, but this will not be the main focus of this study and will only be briefly discussed. Each target formation will be presented with a well log interpretation from Interactive Petrophysics which best presents the overall impression of the formation. Well log displays from all the wells are shown in appendix B.The data from 16/1-15 A did not contain data from the mesozoic interval of the well and was therefore omitted from the analysis.

Thickness maps generated in Petrel is shown in figure 4.1. The maps were generated by convergent interpolation method inside block 16/1. Note that the map of the basement is depth to top.

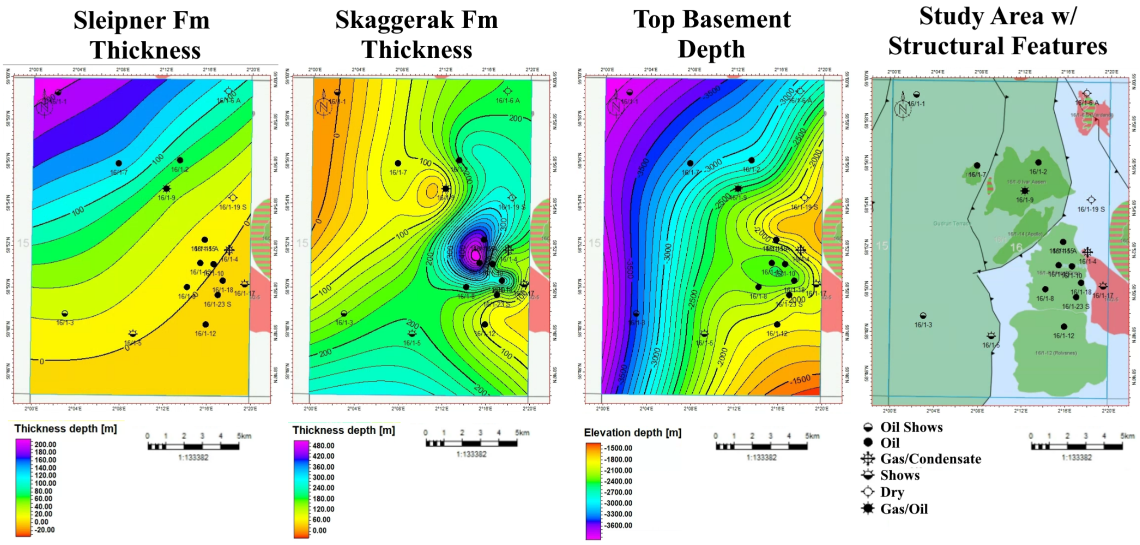
Sleipner Fm Thickness

Skaggerak Fm Thickness

Top Basement Depth

Study Area w/ Structural Features

Figure 4.1: Thickness maps of Sleipner and Skagerrak, with depth to basement map and study area incl. structural features for references. Sleipner and Skagerrak has increments of 20m and basement has increments of 100m.

Shale volume was estimated from the gamma ray log and Larionovs Equation (Old Rock Shale Estimation) with quality control from the neutron-density crossover and PEF log. The arkosic nature of the skagerrak formation results in a high GR reading, and so additionally pictures of core cuttings was used to ensure correctly drawn baseline GR values (Rønnevik et al., 2017). For the water saturation (S_w), Archie's equation was used with default values of n and m. The effective porosity was estimated with the neutron density combination for all wells expect 16/1-2 where the neutron log was unavailble for the target reservoirs and density was used for estimation of porosity. Bad borehole conditions due to washouts and cavings (caliper >> bit size), which heavily disrupts the density log, was corrected by splicing the density log with Gardner's equation (see chapter 3.4.1.4).

Table 4.1: Table showing identified reservoir and pay zones for key reservoirs in the dataset.

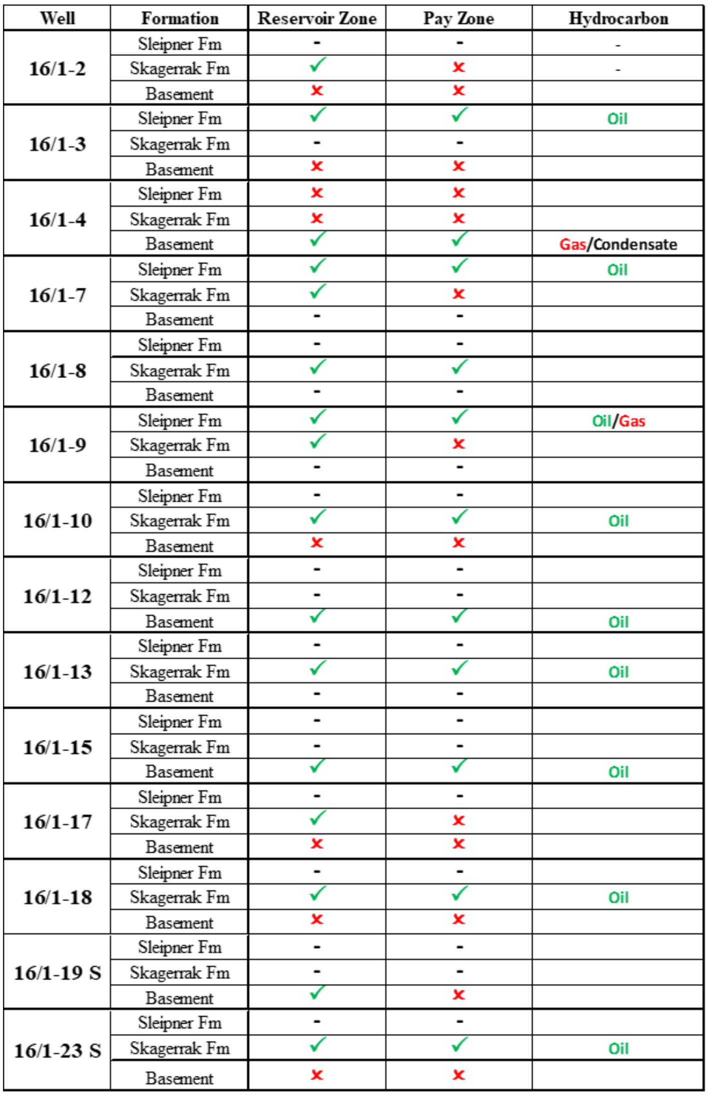

Well	Formation	Reservoir Zone	Pay Zone	Hydrocarbon
16/1-2	Sleipner Fm	-	-	-
	Skagerrak Fm	✓	✗	-
	Basement	✗	✗	
16/1-3	Sleipner Fm	✓	✓	Oil
	Skagerrak Fm	-	-	
	Basement	✗	✗	
16/1-4	Sleipner Fm	✗	✗	
	Skagerrak Fm	✗	✗	
	Basement	✓	✓	Gas/Condensate
16/1-7	Sleipner Fm	✓	✓	Oil
	Skagerrak Fm	✓	✗	
	Basement	-	-	
16/1-8	Sleipner Fm	-	-	
	Skagerrak Fm	✓	✓	
	Basement	-	-	
16/1-9	Sleipner Fm	✓	✓	Oil/Gas
	Skagerrak Fm	✓	✗	
	Basement	-	-	
16/1-10	Sleipner Fm	-	-	
	Skagerrak Fm	✓	✓	Oil
	Basement	✗	✗	
16/1-12	Sleipner Fm	-	-	
	Skagerrak Fm	-	-	
	Basement	✓	✓	Oil
16/1-13	Sleipner Fm	-	-	
	Skagerrak Fm	✓	✓	Oil
	Basement	-	-	
16/1-15	Sleipner Fm	-	-	
	Skagerrak Fm	-	-	
	Basement	✓	✓	Oil
16/1-17	Sleipner Fm	-	-	
	Skagerrak Fm	✓	✗	
	Basement	✗	✗	
16/1-18	Sleipner Fm	-	-	
	Skagerrak Fm	✓	✓	Oil
	Basement	✗	✗	
16/1-19 S	Sleipner Fm	-	-	
	Skagerrak Fm	-	-	
	Basement	✓	✗	
16/1-23 S	Sleipner Fm	-	-	
	Skagerrak Fm	✓	✓	Oil
	Basement	✗	✗	

The cutoffs for net and pay estimation were set to $\phi \leq 0.06$, $S_w \leq 0.6$ and $V_{sh} \leq 0.5$. Another cutoff requirement was also to set the minimun thickness of both net and pay to be atleast 1 meter.

Lithology terminologoies by bin size of V_{sh} are (assuming only sand and shale present):

- $0 - 25\%$ is sand
- $25 - 50\%$ is shaly sand
- $50 - 75\%$ is sandy shale
- $75 - 100\%$ is shale

Porosity terminologies for describing reservoir quality are

- $0 - 5\%$ is insignificant
- $5 - 10\%$ is poor
- $10 - 15\%$ is fair
- $15 - 20\%$ is good
- $20 - 25\%$ is excellent

Permeability terminologies for describing hydrocarbon reservoir properties are

- $1 - 10mD$ is poor
- $10 - 100mD$ is good
- $100 - 1000mD$ is excellent

4.1.1 Sleipner Formation

Petrophysical results for the Sleipner Formation found in the wells are shown in table 4.2. An overview of the well log interpretation of well 16/1-9 is shown in figure 4.2, showing some key logs including reservoir and pay zones, hydrocarbon saturation, permeability and lithology interpretation.

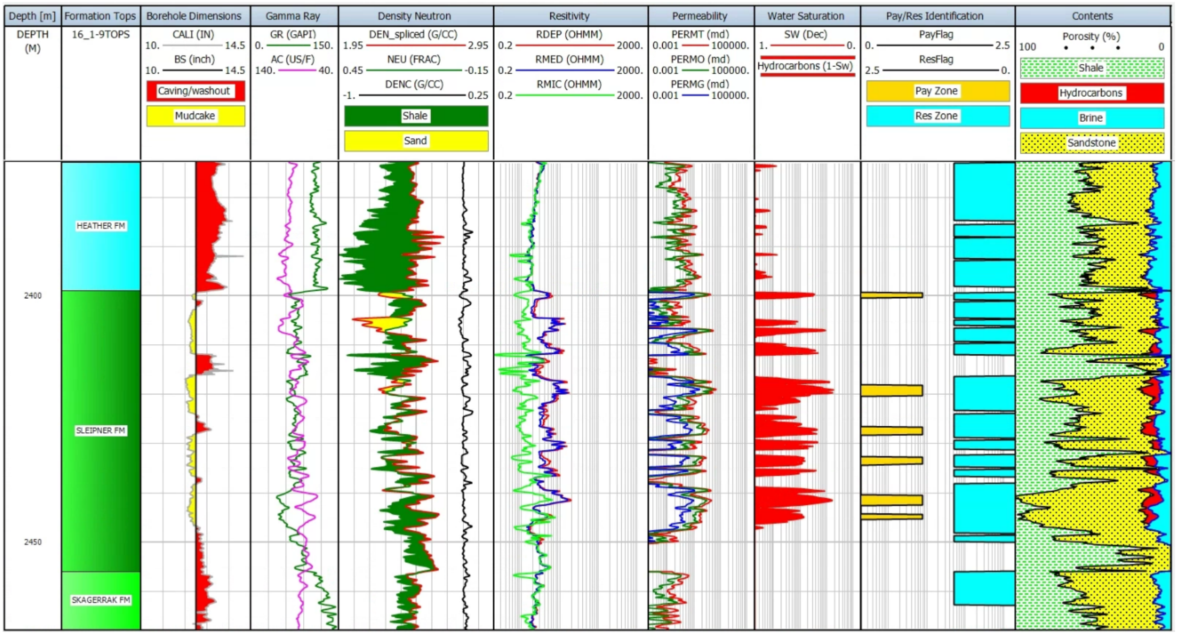

Figure 4.2: Overview of well log intepretation from 16/1-9 (Ivar Aasen Discovery) with hydrocarbon saturation, effecitve porosity, reservoir and pay intervals and lithology identification included. Black dots · of S_W and ϕ indicate core measurements.

The Sleipner formation occurs in 3 wells bored in the dataset (16/1-2, 16/1-7 (West Cable) and 16/1-9 (Ivar Aasen Discovery). It averages around 0.19 shale volume, with well 16/1-2 showing the largest shale volume almost categorized as a sand. The net reservoir part of the Sleipner formation carries an average of 15% porosity, with well 16/1-3, 16/1-7 and 16/1-9 showing, respectively, excellent, good and fair porosites. All wells contain around $7-9$ meters of pay and are listed below with net pay and water satuation, S_W:

- 16/1-3 : 8.88m pay with $S_W = 0.252$
- 16/1-7 (West Cable Discovery): 7.65m pay with $S_W = 0.314$
- 16/1-9 (Ivar Aasen Discovery): 9.45m pay with $S_W = 0.457$

Table 4.2: Petrophysical results for the Jurassic Sleipner formation showing reservoir properties found in each well. "Res" indicates values extracted from intervals satisfying the reservoir criteria and "Pay" are values extracted from intervals satisfying the pay criteria.

Sleipner Formation								
Well	Zone Depth [mRKB]	Gross	Net Res	N/G Res	ϕ Res	V_{sh} Res	Net pay	S_W Pay
16/1-3	2730-2754	24	11.63	0.484	0.247	0.194	8.88	0.252
16/1-7	2953-3083	130	76.23	0.586	0.165	0.162	7.65	0.314
16/1-9	2399-2456	57	40.64	0.713	0.135	0.21	9.45	0.457

4.1.2 Skaggerak Formation

The Skagerrak formation is most frequently occuring reservoir rock from the mesozoic within the dataset, occuring in 8 wells. The petrophysical results for the Skagerrak Formation are shown in table

4.3. An overview of well log interpretation of a characteristic well displaying the Skagerrak formation is shown in fig 4.3. Two tracks of well zones are displayed, with the leftmost being data from NPD and the other being from well correlation and pictures of core samples.

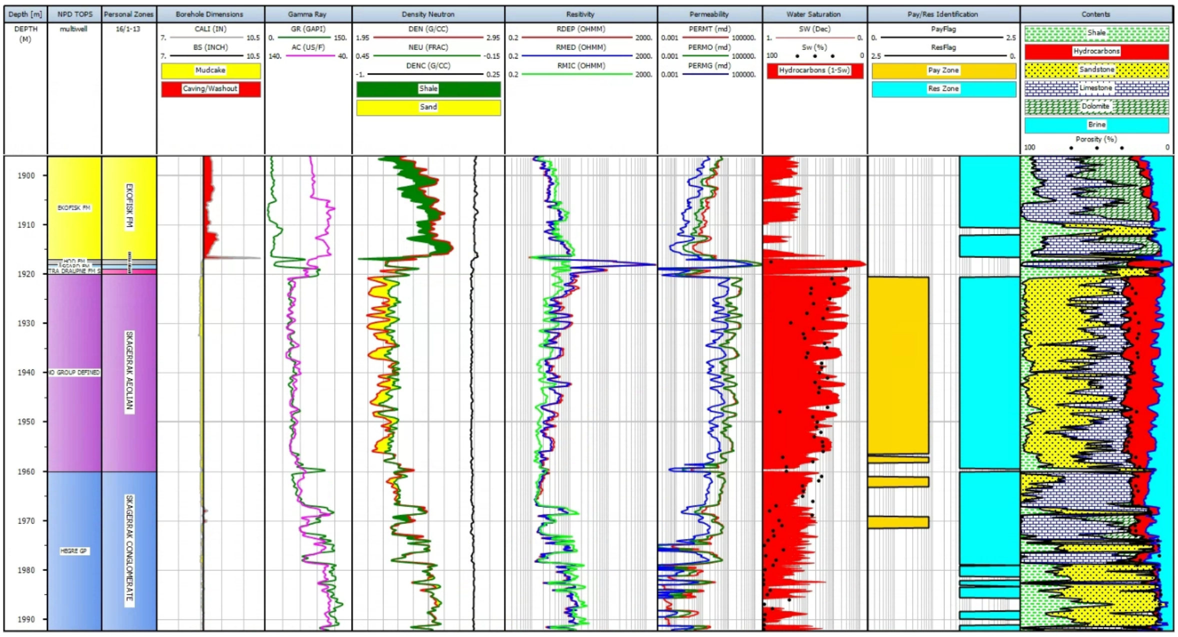

Figure 4.3: Overview of well log intepretation from 16/1-13 (Edvard Grieg Field) with hydrocarbon saturation, effecitve porosity, reservoir and pay intervals and lithology identification included. Black dots · of S_W and ϕ indicate core measurements.

The average shale volume of the skaggerak formation is ≈ 0.22, ranging from very clean sandstones with $V_{sh} = 0.094$ to shaly sandstones $V_{sh} = 0.322$. The porosities of net reservoir in the dataset shows a low spread in values, with an aveage of $\approx 13\%$. The net-to-gross ratios are overall lower than the sleipner formation, but in the study area the Skagerrak formation yields a higher thickness and more occurences.

Table 4.3: Petrophysical results for the Triassic Skagerrak formation showing reservoir properties found in each well. "Res" indicates values extracted from intervals satisfying the reservoir criteria and "Pay" are values extracted from intervals satisfying the pay criteria.

Skagerrak Formation								
Well	Zone Depth [mRKB]	Gross	Net Res	N/G Res	ϕ Res	V_{sh} Res	Net pay	S_W Pay
16/1-2	2424-2620	200	178.92	0.895	0.142	0.136	-	-
16/1-7	3083-3184.90	101.90	20.27	0.199	0.130	0.138	-	-
16/1-8	1925-2201.31	276.31	116.22	0.421	0.156	0.206	1.22	0.533
16/1-9	2456-2644.21	88.21	47.45	0.538	0.104	0.256	-	-
16/1-10	1894-2105.02	253.02	34.9	0.138	0.125	0.222	17.07	0.465
16/1-13	1920-2303.12	383.12	276.45	0.722	0.142	0.288	41.61	0.376
16/1-17	1870-1988.00	343.12	38.87	0.692	0.116	0.322	-	-
16/1-18	1894-1985.00	91.00	59.28	0.651	0.120	0.232	9.14	0.539
16/1-23	1953-2094.00	141.00	111.56	0.791	0.123	0.094	12.04	0.507

5 of the 9 wells penetrating the Skagerrak formation and containing pay, all which are drilled in the Edvard Grieg field. These pay zones, along with the water saturation in the pay zone interval, are:

- 16/1-8 (Edvard Grieg discovery): 1.22m pay with $S_W = 0.533$
- 16/1-10 (Edvard Grieg 1st Appraisal): 17.07m pay with $S_W = 0.465$
- 16/1-13 (Edvard Grieg 2nd Appraisal): 41.61m pay with $S_W = 0.376$

- 16/1-18 (Edvard Grieg 4th Appraisal): 9.14m pay with $S_W = 0.539$
- 16/1-23 S (Edvard Grieg 5th Appraisal): 12.04m pay with $S_W = 0.507$

4.1.3 Basement

The basement had net reservoir in four of the wells in the study area. The petrophysical results are presented in table 4.4. A overview of the well interpretation that penetrated an oil bearing part of the basement is shown in fig 4.4. The well is 16/1-12 situated in the Edvard Grieg field. Core measurements are provided as the black dots in hydrocarbon saturation track and porosity track.

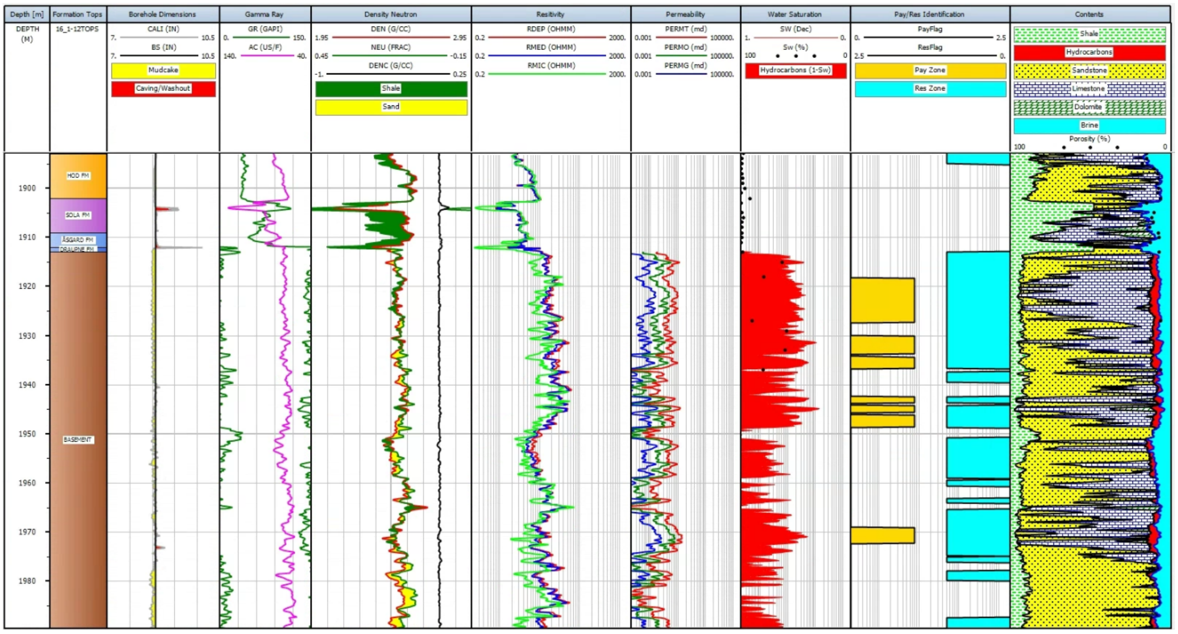

Figure 4.4: Overview of well log intepretation from 16/1-12 (Edvard Grieg Field) with hydrocarbon saturation, effecitve porosity, reservoir and pay intervals and lithology identification included. Black dots of S_W and ϕ indicate core measurements.

The wells only drilled through the top part of the basement, but the gross depth for each of the wells can be sufficient enough to make some remarks about the reservoir characteristics. The basement shows good N/G ratios on the Utsira High ranging from $0.437 - 0.559$ with well 16/1-19 S being on the Gudrun Terrace and showing 0.01. The porosity of the basement is overall poor, with the exception of well 16/1-4 showing 14.9% porosity. V_{sh} measurements were procedurally carried out, but may carry great uncertainties due to basement. V_{sh} ranges mostly from $0.14 - 0.185$ with the exception of $V_{sh} = 0.015$ in well 16/1-19 S.

Table 4.4: Petrophysical results for the Triassic Skagerrak formation showing reservoir properties found in each well. "Res" indicates values extracted from intervals satisfying the reservoir criteria and "Pay" are values extracted from intervals satisfying the pay criteria.

			Basement					
Well	Zone Depth [mRKB]	Gross	Net Res	N/G Res	ϕ Res	V_{sh} Res	Net pay	S_W Pay
16/1-4	1864-2007	143	62.44	0.437	0.149	0.185	40	0.431
16/1-12	1913-2057.3	144.3	80.67	0.559	0.096	0.14	26.21	0.484
16/1-15	1920-2150.11	230.11	106.96	0.465	0.094	0.182	5.79	0.481
16/1-19 S	1891-1993	101.83	1.07	0.01	0.064	0.015	0	-

4.1.4 Permeability estimation

Permeability was estiamted by the use the use of Timur's equations and the Morris Biggs oil and gas formulas. Qualitatively measurements of permeability was estimated by the separation of the caliper-bit size log, indicating mudcakce when the caliper was larger. Separation of the shallow and deep resistivity also helped understand permeability as the horizontal depth of the infiltration of the mudfiltrate could be established. Permeability-porosity cross plot is shown in figure 4.5, showing a nice correlation between Timur equation and Morris Biggs oil equation. A track excerpt from IP shown in fig 4.6 shows the correlation of the Timur equation and the Morris Biggs oil equation with mudcake present and separation of resisitvity logs.

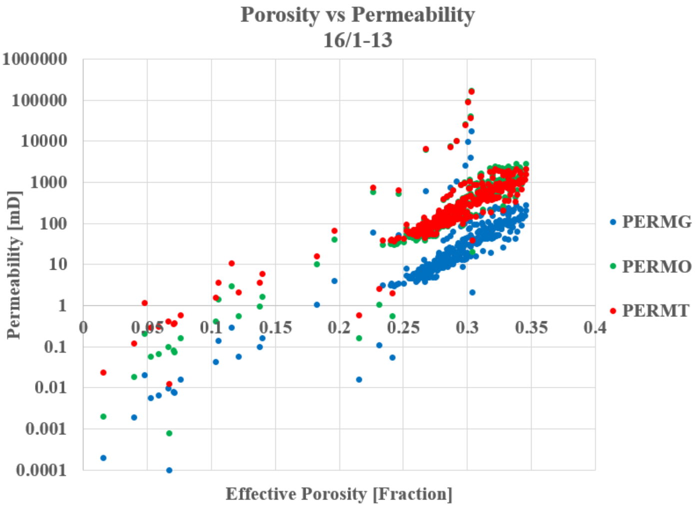

Figure 4.5: Effective porosity vs Permeability plot for the hydrocarbon bearing part of well 16/1-13, Skagerrak Formation. Data are Morris-Biggs gas · , Morris-Biggs Oil formula · and Timur equation · .

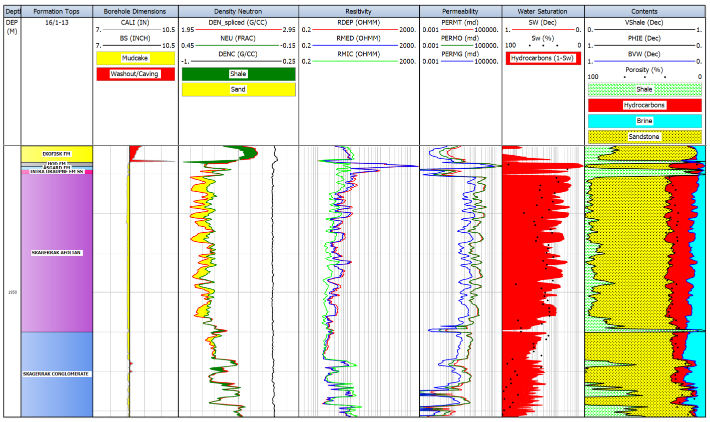

Figure 4.6: Track excerpt from IP showing the correlation between Timur and Morris Biggs oil. Mudcakes and separation of resistivity logs are present from 1917m RKB to 1966m RKB.

4.1.5 Depositional Enviorment

The identification of dominant clay minerals was done by crossplotting thorium vs potassium logs (see fig 4.7a-4.8b). The well logs containing spectral gamma is shown in table 4.5.

Table 4.5: Wells containing spectral gamma measurements and their corresponding fields

16/1-7	16/1-10	16/1-13	16/1-15	16/1-18	16/1-19 S	16/1-23 S
West Cable	Edvard Grieg 1st Appraisal	Edvard Grieg 2nd Appraisal	Edvard Grieg 3rd Appraisal	Edvard Grieg 4th Appraisal	Ivar Aasen 4th Appraisal	Edvard Grieg 5th Appraisal

Figure 4.7a shows the crossplot of Potassium vs Thorium for well 16/1-7 (West Cable Discovery). The Heather formation plots well defined within the mixed clay layers region, while the sleipner formation ranges ranges from glauconite, micas, illite, smectite and kaolinite. The skagerrak formation is shows more constrained clay minerals with mostly plotting in the illite and mixed clay layers region, with occurences of smectite.

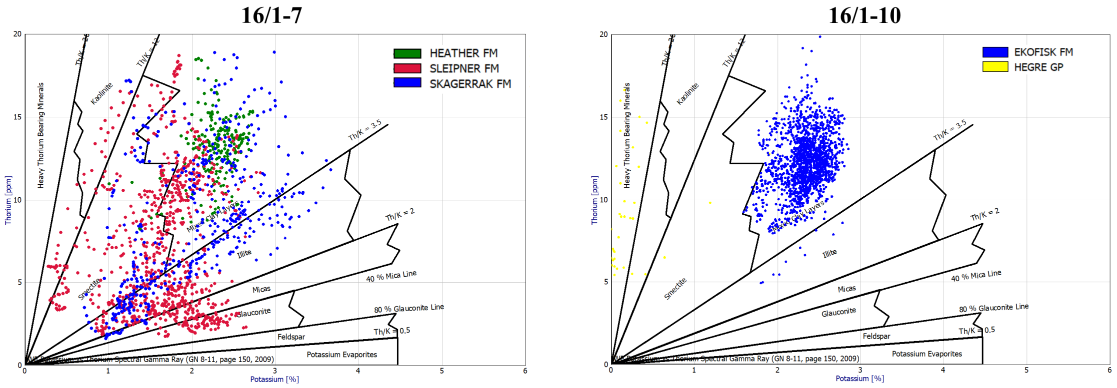

(a) 16/1-7 (West Cable Discovery) showing the Heather-, Sleipner- and Skagerrak Formation.

(b) 16/1-10 (Edvard Grieg 1st Appraisal) showing the Ekofisk- Skagerrak Formation.

Figure 4.7: Potassium vs Thorium Spectral Gamma Crossplots for well 16/1-7 (West Cable Discovery) and 16/1-10 (Edvard Grieg 1st Appraisal). Template is digited from Glover, 2013

Well 16/1-10 (Edvard Grieg 1st Appraisal) is shown in figure 4.7b, with the cretaceous seal of the Ekofisk formation almost wholly consisting of mixed clay layers. The Hegre Group, containing the skagerrak formation, shows severly anomouls behaviour with close to no response in Potassium.

Well 16/1-13 (Edvard Grieg 2nd Appraisal) shows the Hegre Group clay minerals ranging from glauconite to micas and illite to most dominantly mixed clay layers (fig 4.8a). The no group defined [3] clay content is between the micas and the glauconites. Intra Draupne-, Åsgard-and Hod Formations are the thin cretaceous layers which contained HC. The Ekofisk formation is the acting seal in this well, plotting with low Potassium and Thorium levels indicating absent shale volume and are intepreted as chalk.

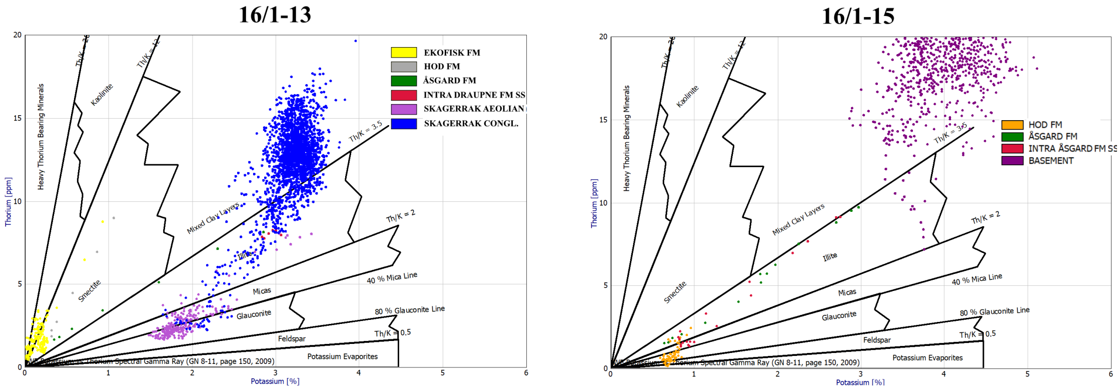

(a) 16/1-13 (Edvard Grieg 2nd Appraisal)

(b) 16/1-15 (Edvard Grieg 4th Appraisal).

Figure 4.8: Potassium vs Thorium Spectral Gamma Crossplots for well 16/1-13 (Edvard Grieg 2nd Appraisal) and 16/1-15 (Edvard Grieg 4th Appraisal). Template is digited from Glover, 2013

Well 16/1-15 (Edvard Grieg 3rd Appraisal) shows the Hod and Intra Åsgard Formation SS (fig 4.8b) plotting with low Thorium and Potassium levels, ranging from potassium evaporites, feldsar and glauconite. With increasing proximity to the the hydrocarbon bearing basement, the SGR response increases along the illite/smectite-illite/mixed clay layers boundary. The basement is of non sedimentary origin and therefore plots almost outside the template from Glover, 2013.

Well 16/1-18 (Edvard Grieg 4th Appraisal) displays the Skagerrak Formation (red) and the Hegre Group (blue) (fig 4.9a)with highly increased potassium response, plotting outside the template from Glover, 2013. The Hod Formation is plotted in the feldspar and glaucinites zone, with the underlying

---

[3] Formation top data from NPD

Sola- and Åsgard Formations plotted in the illite and micas zones.

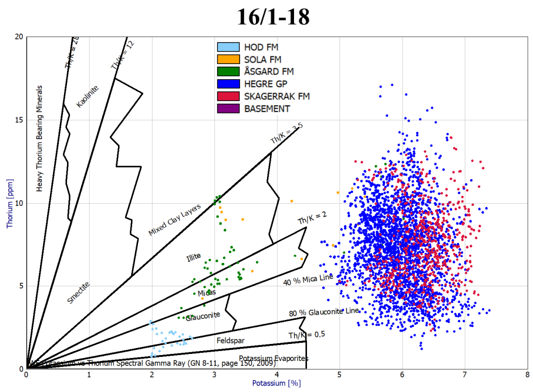

(a) Potassium vs Thorium Spectral Gamma Crossplot of well 16/1-18. Template is digited from Glover, 2013

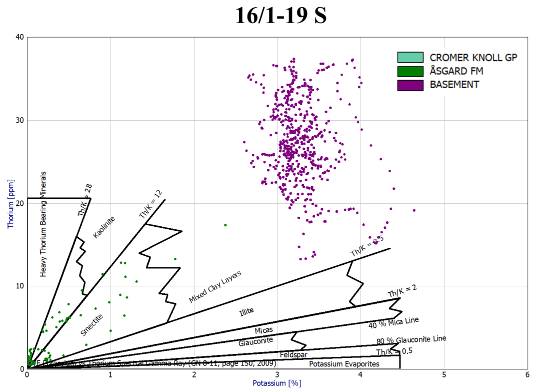

(b) Potassium vs Thorium Spectral Gamma Crossplot of well 16/1-19. Template is digited from Glover, 2013

Well 16/1-19 S (Ivar Aasen 4th Appraisal) is plotted with the Cromer Knoll Group, Åsgard Formation and the Basement. The Åsgard Formation shows most values having very low response on both Thorium and Potassium, with some datapoints increasing inot the kaolinite and smectite zone. The basement is again plotting outside the boundary of the template.

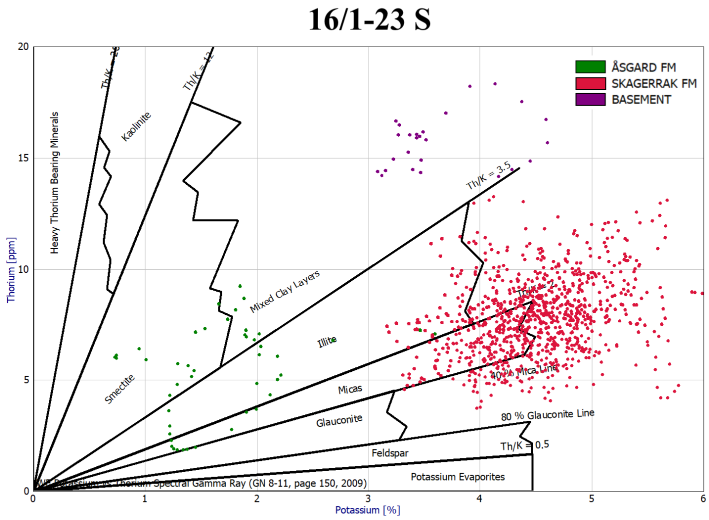

Figure 4.10: Potassium vs Thorium Spectral Gamma Crossplot of well 16/1-23. Template is digited from Glover, 2013

Well 16/1-23 S (Edvard Grieg 5th Appraisal) is shown in figure 4.10 with the Åsgard Formation, Skagerrak Formation and the basement plotted. The Åsgard Formation is plotted in the smectite, illite and mixed clay layers regions, with some datapoints inside the mica region. The Skagerrak Formation shows large values for Potassium, plotting outside the mica-glauconite-illite regions.

Spectral gamma quantites can also be plotted as their ratios, namely Th/K to portray the dominating clay minerals and Th/U to help determine continental- or marine deposits and reducing or oxidizing environment (see 3.4.1.2).

Figure 4.12b shows the Th/K and Th/U ratios determining dominant clay minerals and a general classification of depositional regime for well 16/1-7 (West Cable). The cap rock Heather Formation shows marine deposits with oxidizing enviroments, which continues downwards into the Sleipner Formation. The depositonal regime changes at 3050 MD where the regime oscillates between continental and marine deposits.

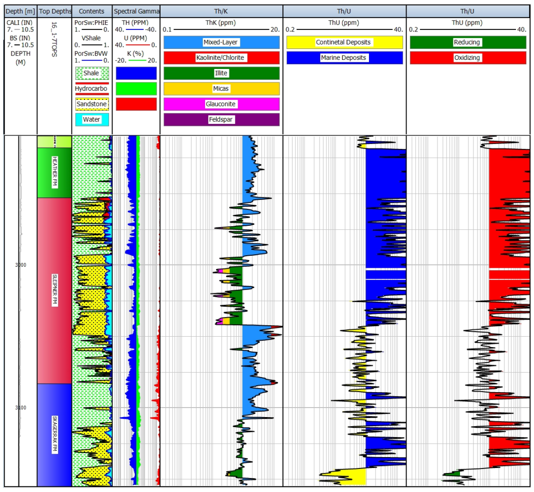

(a) Track display of well 16/1-7 (West Cable Discovery) the interpreted lithology and fluid contents alongside dominant clay mineral and general determination of depositional regime.

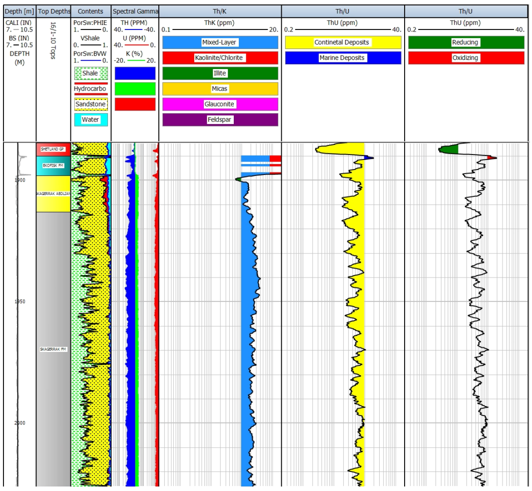

(b) Track display of well 16/1-10 (Edvard Grieg 1st Appraisal) the interpreted lithology and fluid contents alongside dominant clay mineral and general determination of depositional regime.

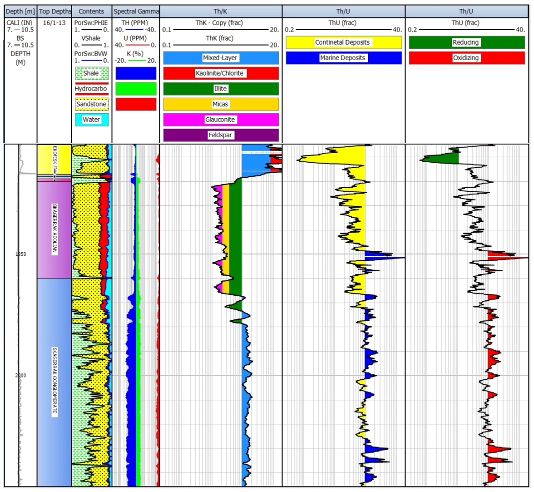

(a) Track display of well 16/1-13 (Edvard Grieg 2nd Appraisal) showing the interpreted lithology and fluid contents alongside dominant clay mineral and general determination of depositional regime.

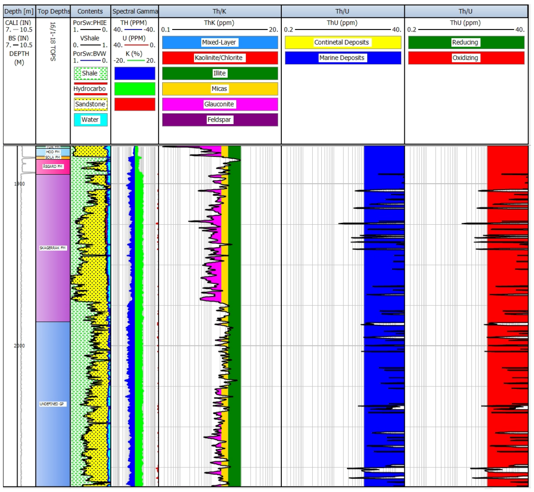

(b) Track display of well 16/1-18 (Edvard Grieg 4th Appraisal) showing the interpreted lithology and fluid contents alongside dominant clay mineral and general determination of depositional regime.

Additional spectral gamma track logs can be found in appendix B, figure 4.12b and 4.12b.

4.2 Discussion

This subchapter discusses the results shown above, and goes into detail about depositional trends and hydrocarbon potential of the Triassic and Jurassic reservoirs. A brief overview of the Net-to-Gross, porosity and shale volume for the Triassic and Jurassic targets are shown in figure 4.13.

The Edvard Grieg field contains oil in primarily the Triassic successions of the Hegre Group, most dominantly the Skagerrak Formation. There are also occurrences of hydrocarbons in basement rocks from Devon and thinly draped cretaceous layers over the Triassic successions. The discussion below will focus on the Jurassic and Triassic succession, followed by a brief discussion of the petrophysical analysis and findings related the basement and cretaceous units.

4.2.1 Jurassic reservoirs

The Jurasssic discoveries contained in the study area are dominantly owed to the Sleipner formation with some hydrcarbon occurences in the Intra Heather Sandstone Unit. The Jurassic reservoirs are

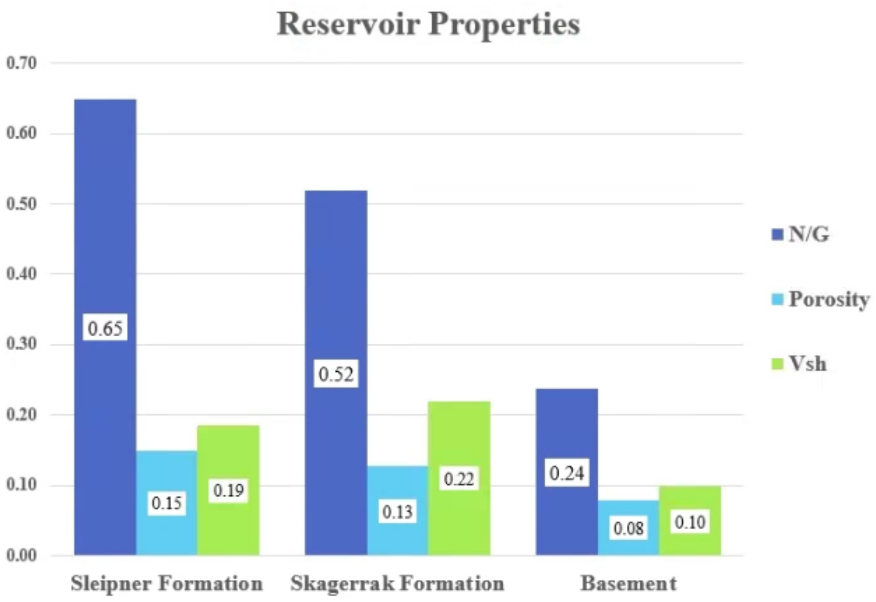

Figure 4.13: Average Net-to-Gross values for the relevant reservoirs in the study.

occurring on the flanks of the Utsira High, owing to Jurassic unconformity. The Sleipner formation showed pay similar sum of net pay in all ways. The porosity of the reservoir at 16/1-3 and 16/1-7 (West Cable) exhibit values up to $\phi = 0.3$ near the top of the reservoir, before quickly decreasing towards $15 - 10\%$. Well 16/1-9 (Ivar Aasen Discovery) shows a more constant vertical distribution of porosity with more spurious points approaching $\phi = 0.2$.

The thickness distribution within the Ivar Aasen field is greatly smaller than within the West Cable discovery, which is situated further out on the Gudrun Terrace.

Core photos are only availible for well 16/1-9 and will be used to compare with findings in the petrophysical analysis.

4.2.1.1 Sleipner Formation

The Sleipner Formation was deposited in a coalescing fluvio-deltaic environment which is evident from the serrated, funnel shaped gamma ray log. Well 16/1-7 (West Cable Discovery) shows and upwards increasing, serrated gamma ray log indicative of deltaic distributaries. The spectral gamma ray log indicates a high spread of clay minerals, with large amounts of illite, glauconite and smectite for the West Cable Discovery (16/1-7). The temperature of the reservoir is here at 85-87°C, indicating the reservoir is well below the transition zone where smectite is transforming into illite. The presence of glauconite suggests parts of the depositional environment was deposited in a shallow water shelf environment. These points are located in the lower half of the Sleipner Formation.

Hydrocarbon identification was carried out by visual inspection of the degree of separation in the neutron-density crossover plot. Large separations was indicative of gas while smaller, but positive separations was indicative of oil. The sonic log was also used since gas significantly decreases V_P, while oil is more similar to brine.

The fluid contacts and top of reservoir was interpreted by comparing separations of, when availible, shallow and deep resisitvity. As mud filtrate heavily effects the shallow resistivity, separation between shallow and deep is indicated by the presence of hydrocarbons, as none of these wells did not use OBM[4].

Well 16/1-3, situated on the Grudrun Terrace, was found to be containing hydrocarbon but is omitted from the discussion due to very poor log quality with higly deviatoric caliper- and density correction log, and unreasonable water saturation calulcations. The log overview can be found in appendix B, figure B.5.

---

[4] Oil Based Mud

Figure 4.14: Core photos of the Sleipner Formation in well 16/1-9 (Ivar Aasen Discovery). Left side from 2418m RKB with showing sandstone with possible carbonate clasts. Right side from 2426m RKB showing a more dense carbonate section.

16/1-7 (West Cable Discovery): The reservoir is interpreted to only contain oil, with the top of the reservoir situated at 2953m RKB. The oil water contact is mainly determined from the end of the interpreted water saturation at 2968m RKB, as there were no shallow resistvity availible. NPD, 2021c presents 2969.4 as the OWC, giving a 11m net oil sand which is higher than the pay zone of 7.65m found in this study.

16/1-9 (Ivar Aasen Discovery): Gas was interpreted at the top of the reservoir, starting at 2399m RKB, as the formation showed a great neutron-density separation. The GOC [5] was intepreted at 2407m RKB, resulting in a gas cap of 8m. The OWC was not easily spottable, as the neutron-density crossover quickly deteriorated along. The interpretation of the OWC was at 2446m RKB with the closure of the resistivity logs. NPD, 2021c reports no visible OWC and reports oil shows downwards into the Skagerrak Formation.

Below the gas cap occured very shaly intervals which may result in compartments of the reservoir, such as 2412 – 2415m RKB which shows poor porosity and no oil saturation. Approaching 2426m RKB, core photos indicate increasing carbonate and carbonate clasts which reduces the vertical permeability inside the reservoir.

4.2.2 Triassic reservoirs

The triassic reservoirs of the Skagerrak Formation showed, on average, lower reservoir properties on N/G, porosity and shale volume. However the upper part of the Skagerrak Formation did show excellent reservoir qualities, with porosites ranging up to $\phi = 0.3$. Figure 4.15 shows two core photos from well 16/1-13 (Edvard Grieg 2nd Appraisal) and 16/1-23 S (Edvard Grieg 5th Appraisal), showing the two entierly different sortings found in the Skagerrak Formation.

---

[5] Gas-Oil contact

The interpreted results from the Triassic Skagerrak Formation of the Hegre Group are discussed below. Only the target reservoirs containing pay intervals are discussed and hence well 16/1-17 (Jorvik Prospect) is omitted.

Figure 4.15: Core photos of the Skagerrak Formation. Left hand side is from well 16/1-13 (Edvard Grieg 2nd Appraisal) showing cross stratified sandstone from depth 1928m RKB, exhibiting 1000mD. Right hand side from 16/1-23S (Edvard Grieg 5th Appraisal) showing poorly sorted conglomerate from depth 1958m RKB, with highly deviatoric permeability of an approximate 100mD.

4.2.2.1 Skagerrak Formation

During the deposition of the skagerrak formation, the climate was arid and continental with flash floods creating fluvial surfaces. The depositional environment is dominated by poorly sorted conglomerates from alluvial fans, with occasional aeolian deposits. Well 16/1-13 shows greater porosity in the upper part of the Skagerrak formation as core measurements classifies it as aeolian sandstone.

NPD, 2021c describes the depositional environment of the Skagerrak Formaiton as a coalescing system of prograding alluvial fans. Alluvial fans suffer from poor sorting and results in heavily degraded porosity, evident from the petrophysical analysis. However upper parts of the Skagerrak Formation in 16/1-10 and 16/1-13 high porosity, hydrocarbon bearing sandstones are interpreted as non-conglomeratic sands of continental depostional regime.

The spectral gamma ray indicates the skagerrak formation mostly consisting of continental deposits [6]such as in 16/1-10 (Edvard Grieg 2nd Appraisal) with occasional occurences of marine deposits as shown in the more eastward well 16/1-13 (Edvard Grieg 3rd Appraisal).

The seal for the Skagerrak Formation varies, but is consisting of Late Cretaceous shales or chalks. The list of the following cap rocks are

- 16/1-2 (Ivar Aasen Field): Heather Formation (Shale)
- 16/1-8 (Edvard Grieg Discovery): Hod Formation (Shale)

---

[6] With the exception of 16/1-18 (Edvard Grieg 4th Appraisal) showing anomalously low Uranium values resulting in an interpretation of oxidizing, marine depositions.

- 16/1-10 (Edvard Grieg 2nd Appraisal): Ekofisk Formation (Chalk)
- 16/1-13 (Edvard Grieg 3rd Appraisal): Ekofisk Formation (Chalk)
- 16/1-17 (Jorvik Prospect): Åsgard Formation (Shale)
- 16/1-18 (Edvard Grieg 4th Appraisal): Åsgard Formation (Shale)
- 16/1-23 S (Edvard Grieg 5th Appraisal): Åsgard Formation (Shale)

16/1-2 (Ivar Aasen Field): Well 16/1-2 was drilled in 1976 through the Ivar Aasen field and was dismissed as not carrying oil. The resistivity measured with 6FF40 induction and spherically focused resistivity tools did not generate a hydrocarbon response. (Johansen et al., 2018). The well does however show fair porosity with overall low shale content. Three large spikes in the shale volume however, situated at 2442, 2457 and 2502m RKB are spotted which may contribute to reduced veritcal permeability.

16/1-8 (Edvard Grieg Discovery): Top oil is interpreted at 1925 m RKB, with separation of resistivity logs. The density-neutron shows highly oscillating crossover from positive to negative, with a general decreasing trend with depth inside the reservoir. The caliper log showed the same oscillating trend, which can have interfered with the density measurements as shown with the large values exhibited by the density correction log. The oil water contact is ambigious due to the separatation of the resistivity log never fully ceasing and multiple crossovers of neutron-density. Core measurements were therefore helped to establish an OWC at 1960m RKB. Estimates from NPD, 2021c established the OWC by the use of pressure data and reports no oil shows below 1966 m RKB.

16/1-10 (Edvard Grieg 1st Appraisal): Oil was found at 1989m RKB with a sharp decline in neutron and separation in the resistivity logs. The OWC was very hard to detect and is ambigiously drawn at 1950m RKB with with fairly constant density, closure of resistivity logs and very non-continous water saturation. Core measurements of water saturation have a mismatch with the S_W calulcated from Archie's equation as it is unable to match both the highs and the lows of the water saturation. Limestone inclusions is interpreted from the photoelectric log at around 1925m RKB, which matches the core photos indicating a banded layer of carbonates.

16/1-13 (Edvard Grieg 2nd Appraisal): Top oil was identified at 1917 m RKB, with the with the Hod, Åsgard and Intra Draupne Formations draped above. The boundary of the top of the reservoir was found by insepcting the separation of the deep and medium depth resistivity logs crossing over the shallow resisitvity log. The neutron-density crossover log did also start showing a continous separation starting at this depth interval. This separation coinsides with the one given from NPD, 2021c.

The separation terminates at the depth of the aeolian part of the Skagerrak Formation with an interpreted, slightly barrier of shale at the change towards the conglomeratic, alluvial part of the skagerrak formation. The spectral gamma ray tracks interprets the dominant clay mineral in this region is illite. The caliper-bit size log combo indicates a possible decrease in permeability for this region. Below this point the separation of the resisitivty logs and the positive crossover of the neutron-density log continues until 1966 m RKB and is interpreted as the oil-water contact, which is in accord with drilling statements from NPD, 2021c.

16/1-18 (Edvard Grieg 4th Appraisal): Oil was identified at 1894 mRKB, and a OWC interpreted to be at 1956m RKB with the density-neutron-and resistivity log separation closing. Below the OWC, a large inclusion of limestone is interpreted from the photo electric log. NPD, 2021c writes that no OWC was found, but does report a 66m oil column.

A large inclusion of shale was interpreted at 1900 − 1905m RKB, reducing the water saturation and acting as a vertical separation in the reservoir. The gamma ray log is fairly constant at high values, but is shown by spectral gamma to be the result of severly high Potassium values, indicating that the reservoir is highly arkosic.

16/1-23 (Edvard Grieg 5th Appraisal): Oil was identified at 1953m RKB with separation of neutron-density and resistivity logs, and the OWC at 2006m RKB with the closure of those log combinations. NPD, 2021c reports a gross oil coumn of 66m, yielding an difference of 17m.

The Skagerrak Formation showed no heavy inclusion of shale and exhibited fair to good porosites. Some sporadic inclusions of limestone was interpreted, but did not decrease the hydrocarbon saturation.

The spectral gamma ray logs indicated the reservoir containing Illite, micas and glauconite, with abnormally high potassium values indicating arkosic sandstones.

No mudcake was identified in the reservoir. The core photo from 4.15 shows a poorly sorted conglomerate with excellent permeability which is disagreeing with the permeability estimates from the Timur and Morris Biggs Oil equation only yielding 36mD and 18mD, respectively.

4.2.3 Basement and Cretaceous Units

The Edvard Grieg field contains mainly oil inside the Triassic Skagerrak Formaiton. However a NWW to SEE trending fault dipping southwards results in the basement being the reservoir in the northern part of the field. (SOURCE). There are also some wells, 16/1-13 (Edvard Grieg 3rd Appraisal) and 16/1-15 (Edvard Grieg 4th Appraisal) which have hydrcarbons contained within the thinly draped Cretaceous layers. Figure 4.16 shows core photos of the basement and the Intra Åsgard Formation SS from well 16/1-15 (Edvard Grieg 4th Appraisal).

Fractured basement is difficult to intepret due to its non sedimentary origin. Results are nevertheless discussed in a short fashion here, respecting that the interpretation is heavily uncertain. The pre-devonic fractured basement shows the worst reservoir quality, with porosities averaging at $\phi = 8\%$ with a N/G of 0.24. The contributor to the porosity and permeability in the basement are mainly the fractures.

Figure 4.16: Core photos from well 16/1-15 (Edvard Grieg 4th Appraisal) showing to the left the Pre-Devonian Basement from depth 1924 – 1924.5m RKB and to the right the Intra Åsgard Formation SS from depth 1918 – 1918.5m RKB.

16/1-4: Gas is identified at 1864m RKB, with great separation in the density-neutron and the resistivity logs. The OWC is interpreted at 1909m RKB with the water saturation sharply decreasing. The caliper log is highly deviatoric resulting in the interpretation being highly dubious since thevdensity- and V_P log are heavily affected.

16/1-15 (Edvard Grieg 3rd Appraisal): Oil was identifed starting at 1917m RKB, starting in the Cretaceous Intra Åsgard Formation. A very large separation indicates tremendous oil saturation in this interval, with the saturation sharply declining into the underlying Pre-Devonian basement. The OWC was identified at 1972m RKB by the separation of resistivity logs reduced while NPD, 2021c reports an OWC at approximately 1965m RKB. The caliper and bit size log shows a mud cake occuring down to the OWC, indicitaing a very permeable basement. The basement shows a fair to poor porosity with no large deviation in gamma ray log.

The Intra Åsgard Formation exhibits an effetive porosity up to 28%, and is defined by NPD, 2021c as a chalky arenite.

16/1-12 (Rolvsnes Field): Oil was estiamted at 1913 mRKB with the separation of the resistivity logs. The neutron-density showed a slight separation alongside the resistiviy down to an ambigious

OWC around 1959m RKB. Core measurements of water satuartion were sparse in the basement interval and showed a reasonable fit with the estimates from the Archie Equation. Lithology estiamtion and was conducted routinely and is not representative of the igneous lithology.

4.2.4 Quality control by core measurements

The wells, where provided, is quality checked by the use of core measurements provided. These measurements help guide both porosity, water saturation and permeability estimates. More detailed analysis of the core measurements are discussed below with comparisons from published literature.

Core studies with XRD (X-ray powder diffraction) and SEM (scanning electron miscroscope) has been conducted by Mahmic et al., 2018 on well 16/1-10, 16/1-13, 16/1-18 and 16/1-23 S, all situated in the Edvard Grieg field. Two main lithological groups were identified within the Skagerrak formation, conglomerates and sandstones, which again were divided into either sandy or silty conglomerate and interbedded opr large scale cross-bedded sandstone. Integranular volume and porosities from the study is shown in fig 4.17.

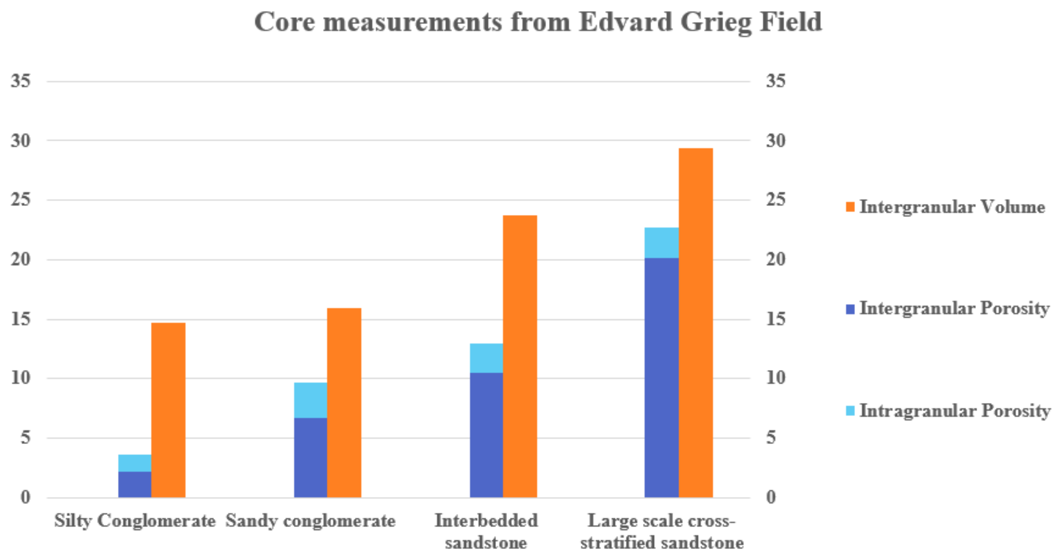

Figure 4.17: Intergranular porosity, intragranular porosity and intergranular volume from Mahmic et al., 2018 on their 4 classified lithofacies. The silty conglomerates showed the most reduction from diagensis, while the large scale cross-stratified sandstone was the most resilient.

SEM of the large scale cross-stratified sandstone and the sandy conglomerae from Mahmic et al., 2018 shown in figure 4.18. The difference sorting is highly apparent, with the sandy conglomerate reported losing most of its intial porosity due to mechanical compaction 19.3% comapred to porosity loss from cementation 3.2%. The large scale cross-stratified sandstone lost 14.2% due to porosity and 4.5% to cementation. The difference in feldspar content is highly evident, which yield abnoramlly high values of Potassium found in spectral gamma crossplots. Carbonate cement is more present in the finely sorted sandstone (3.0%) compare to the conglomerate (0.9%).

The porosity difference between these two lithological groups are most easily identified with the different degrees of sorting. The intergranular porosity in the conglomerates carry lower porosites of around 2.2 – 6.7% for the sandy and silty, respctively, and 10.5 – 20.1% for the interbedded and large scale cross-bedded sandstone, respectively Mahmic et al., 2018. The conglomeratic part of the skagerrak formation was also found suffering from carbonate cement and authigenci clay filling up the pore spaces more so than the sandstone units (Mahmic et al., 2018), which is explains the difference in intergranular volume and the porosity.

4.2.5 Uncertainties

The uncertainties regarding the petrophysical analysis presented and discussed in this chapter are:

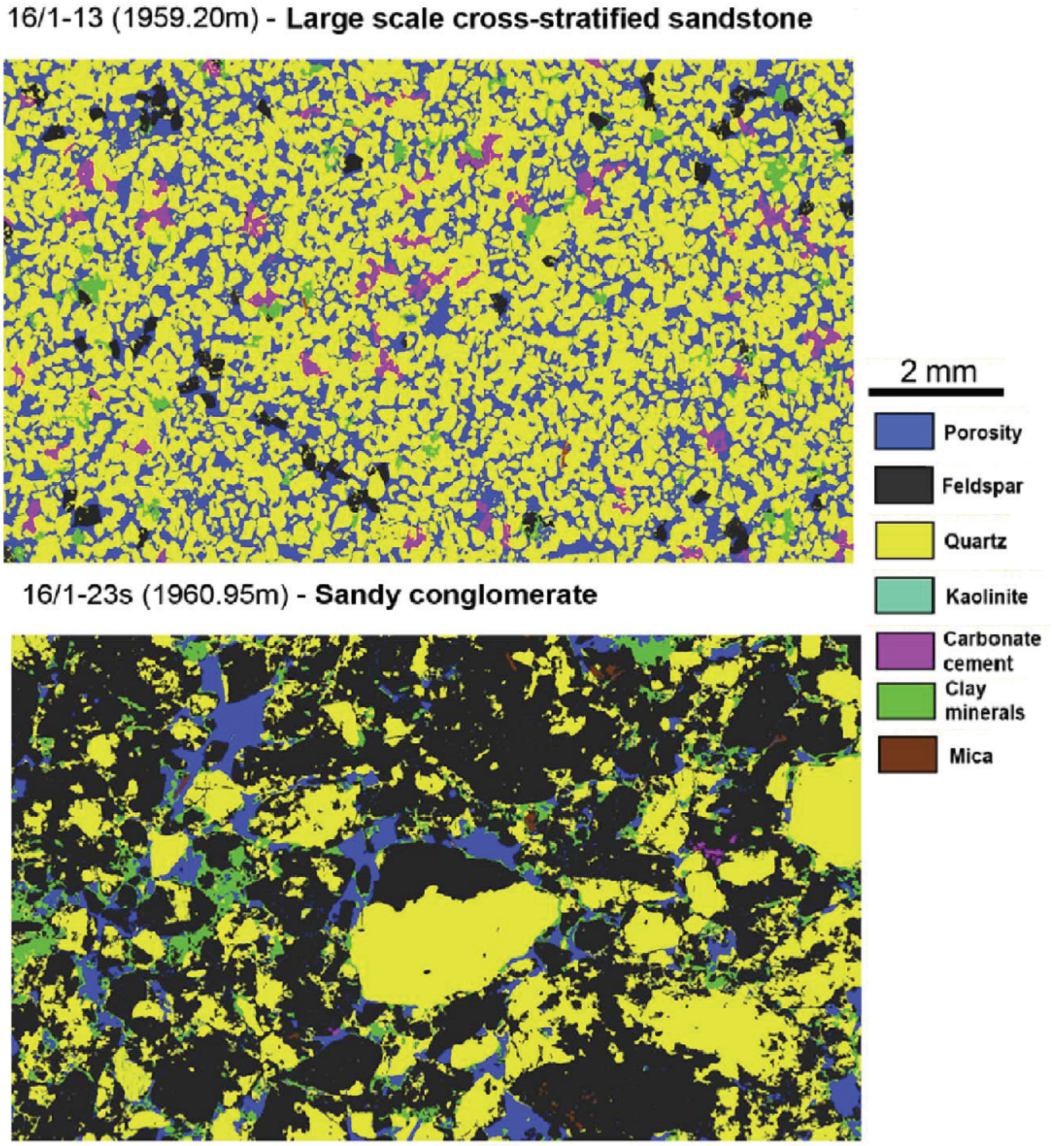

Figure 4.18: SEM from Mahmic et al., 2018 showing the large scale cross stratified sandstone in the upper part of the Skagerrak Formation in well 16/1-13 (Edvard Grieg 2nd Appraisal) and the sandy conglomerate from the lower part of the Skagerrak Formation in well 16/1-23 S (Edvard Grieg 4th Appraisal).

- Older wells carried high caliper logs and where omitted for more detailed analysis. These wells are displayed in appendix B
- The physical properties of the mud filtrate where at large unknown, but where drilled with Performadrill (a water based mud)(NPD, 2021c) in the target horizons.
- Shale volume estimation was carried out by visual inspection, compared with lithology discrimination of the density-neutron log crossover. For the arkosic sandstones of the Hegre group, thorium logs were used for shale estimations where spectral gamma log were available. Shale volume estimation can also be distorted by heavy minerals occuring.
- Porosity estimation was carried out by using squared average of density and neutron estimates of porosity. Baseline neutron and density values for wet and dry clay used were the default values in Interactive Petrophyiscs and may carry uncertainties.
- Water saturation was carried out with Archie's equation and carries uncertainties in the various constants (see 3.4.4). Estimation of the resitvity value of the in situ water and the mud filtrate was additional unknown parameters which may carry uncertanties.

- Permeability estimates are carried out by empirical equations from literature and should be treated as a qualitative set. Although they were compared with core measurements to establish soundness of analysis, core measurements where not always available and did not carry extensive coverage of target formations.

CHAPTER 5

Rock Physics Diagnostics

5.1 Results

The results from rock physics diagnostics by rock physics templates are presented in this chapter. Rock physics properties computed from well logs in the previous chapter are cross plotted with varying petrophysical quantites such as shale volume, porosity and water saturation. These cross plots are then compared with rock physics templates which are theoretically and empirically derived trend lines for quality controlling interpretation in reservoir units. It should be noted that background trends are basin specified and need to be fitted to the geology in the underlying area for best fit.

The reservoirs studies in this chapter are the reservoir units are situated in the Ivar Aasen field and the Edvard Grield field and are showed below. The wells contain pay in the

- 16/1-2 (Ivar Aasen Field)
- 16/1-7 (West Cable Discovery)
- 16/1-8 (Edvard Grieg Discovery)
- 16/1-9 (Ivar Aasen Discovery)
- 16/1-10 (Edvard Grieg 1st Appraisal)
- 16/1-13 (Edvard Grieg 2nd Appraisal)
- 16/1-15 (Edvard Grieg 3rd Appraisal)
- 16/1-18 (Edvard Grieg 4th Appraisal)
- 16/1-23 (Edvard Grieg 5th Appraisal)

Well 16/1-15 (Edvard Grieg 3rd Appraisal) mostly contains oil in the Pre-Devonic basement but is routinely analysis in the same fashion to highlight the difference in lithology from the Mesozoic, sillisiclastic reservoirs.

5.1.1 V_P vs V_S

The availability of V_S data is shown in figure **??** with primarily the older wells missing those logs. A plot of all wells containing both V_P and V_S is shown in fig 5.1. The mudrock line from Greenberg and J. Castagna, 1992 and the clastic rock equation is plotted alongside a regression fitted line. The data is constrained by evaluating all samples which contain $S_W = 1$ from the petrophysical analysis. The equations from the literature heavily overestimates V_S at high values. The missing log intervals of interest in i.e. 16/1-2 and 16/1-4 were therefore estiamtion with the linear regression fit. Comparisons between the Han Shaly line for $\phi < 15\%$ still overcompensate related to the regression line.

$$\text{Regression Line :} \quad V_S = 0.680V_P - 0.594 \tag{5.1}$$

$$\tag{5.2}$$

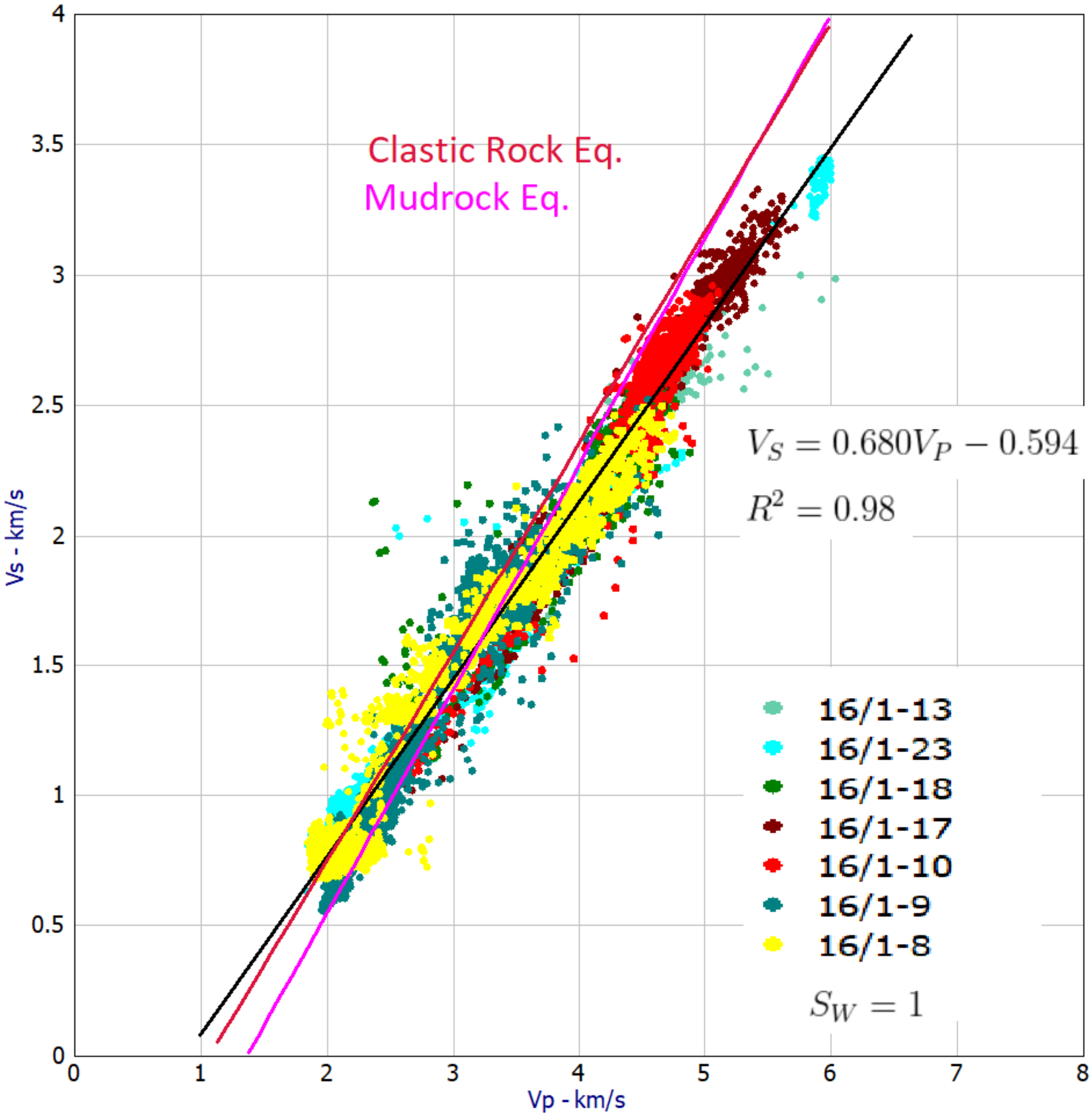

Figure 5.1: Figure showing all the data of from the petrophysical analysis plotted in the V_P vs V_S space, with the Mudrock and clastic rock equations plotted in. A regression line is drawn as shown to the right in the figure.

s

Missing log intervals of interest of 16/1-2, 16/1-4 were estimated by the use of Greenberg and J. Castagna, 1992 and linear regressions from same formations from geographically close wells with similar burial depth. The crossplots are firstly constrained by only evaluating brine saturated sands ($S_W = 1$, clean sands and shaly sands ($V_{sh} \leq 0.5$) to assess the reliability of the datapoints in regards to the equations from the literature.

V_P vs V_S is great for indicating presence of gas as it greatly effects V_P while V_S is indiscriminate for fluids. It can also help in indicating lithology as V_P/V_S ratios are different for i.e. sandstones and shales, or help understand the extent of compaction due to larger V_P and V_S.

Figure 5.2 shows the background trend of all well data, color coded by ϕ_E and V_{sh} respectively. Hydrocarbon containing datapoints are not plotted to omit any effects on the V_P regarding hydrocarbon effects, aswell as bad log intervals of V_P from caprocks which were spotted from the caliper log. The Greenberg and J. Castagna, 1992 sandstone and shale lines are also plotted. The compaction trend is easily visible in fig 5.2, sharply decreasing for high values of V_P and V_S. The colorcoding of V_{sh} showed the best fit with the Greenberg and J. Castagna, 1992 sandstone and shale lines, although varying in accuracy.

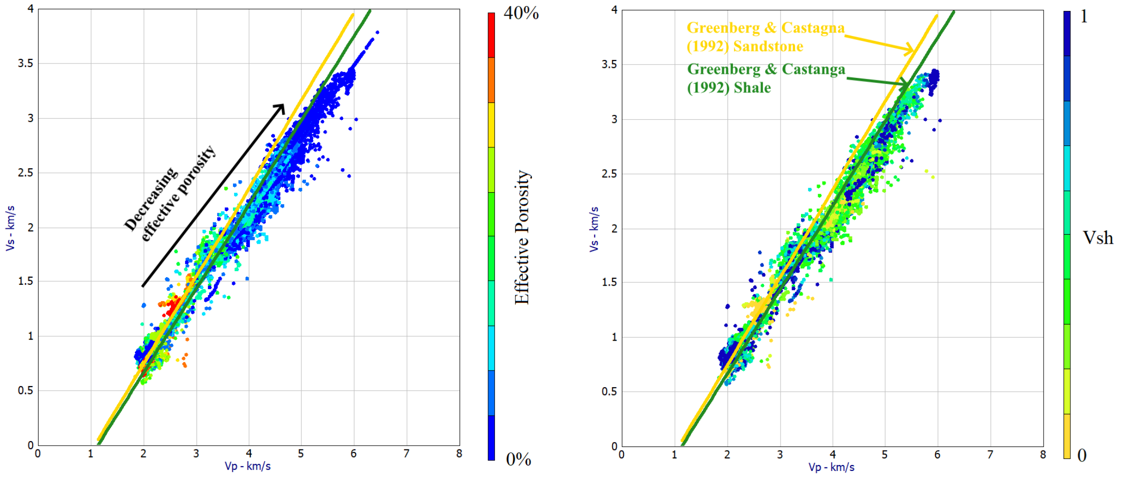

Figure 5.2: Figure showing all the data of from the petrophysical analysis plotted in the V_P vs V_S space. Left hand side is color coded with effective porosity, right hand side color coded with V_{sh}. Water satuartion cutoff is applied to $S_W = 1$ to avoid effects of hydrocarbon.

5.1.1.1 Skagerrak Formation

Figure 5.3 shows the V_P vs V_S crossplot for the Skagerrak Formation in all wells. The data is separated into pay on the left hand side and reservoir on the right hand side. Most of the pay and reservoir is overlapping due to the low ϕ_E, along with similiarities in V_P for oil and brine. A strong separation from the background is spotted at high porosites, which is the result of well 16/1-13 (Edvard Grieg 2nd Appraisal) with ϕ_E up to 30%.

5.1.2 Contact Models

Velocity versus porosity crossplots are introduced in chapter 3.5.6.1. The contact models were in part generated in Python by the methodology 3.5.6 and 3.5.4. By employing contact models, geological features such as sorting, diagentic trend and cementation can be visually estimated by comparing datapoints to the trend lines. The overlay contact models are superimposed onto the cross plots, calculated in Python by the methodology disucssed in 3.5.4 The parameters were chosen partially by typical values and partially fitted to the basin. The parameters for the construction is shown in table 5.1

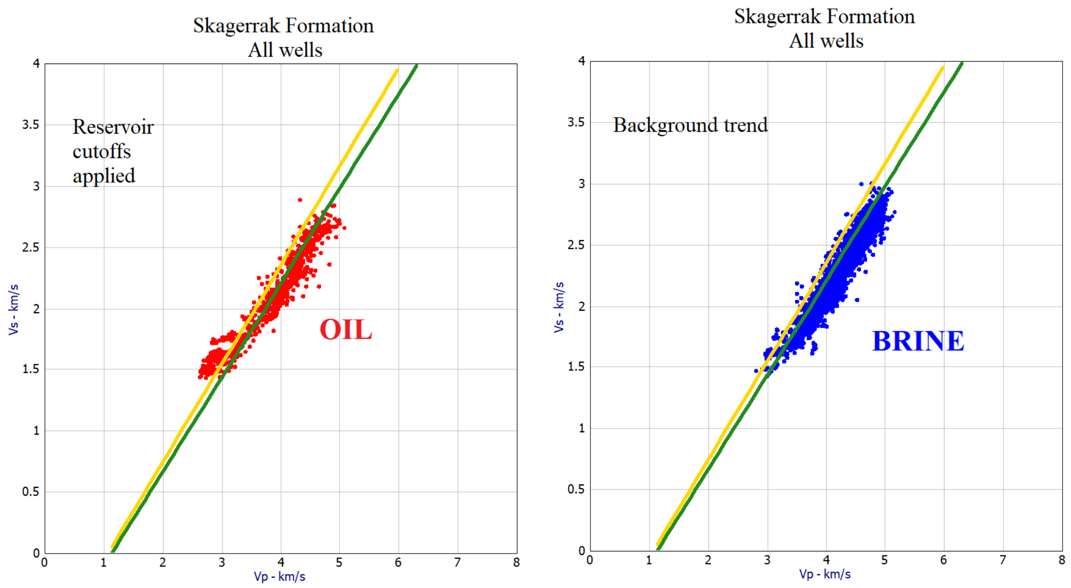

Figure 5.3: Plot showing the skagerrak formation in all wells with Greenberg and J. Castagna, 1992 sandstone and shale lines. Reservoir cutoffs are applied, with the left hand side delinaeted by considering $S_W \leq 0.6$.

Cement volume can be derived from the contact models, but is also attempted quantified from the Marcussen et al., 2010 formula and is disucssed more below in the contact model part.

Table 5.1: Input parameters used in calculating the contact models plotted in V_P or V_S vs ϕ space. P (effective pressure) was fitted to the data to better explain compaction effects.

K_M	μ_M	K_f	ϕ_C	ρ_b	ρ_W	P
37 GPa	44 GPa	2.38	0.4	2.65 g/cc	1.025 g/cc	10 MPa

To most accurately portray the effects of the sandgrains with increasing inclusion material and diagenisis (cementation), the shalyness and pore fluids are adjusted for. V_{sh} is therefore only plotted for values ≤ 0.5, conforming to the terminologies for sand and sandy shale. To evade fluid effects on the seismic velocities, V_S is used in the crossplots which is indifferent to pore fluids.

The clay volume lines from Han et al., 1986 can help quality control for the effective pressure and the shale volume interpreted in the petrophysical analysis. A fit of the Hans clay lines at 20MPa is shown in figure 5.4. The inverted V-shape described from Marion et al., 1992 is tried to interpret to limiting results. Large amounts of the conglomeratic skagerrak formation carries small porosites and plots will into the boundary of grain supported-shale supported matrix. The circled area of high V_{sh} is contributed to the lower part of the reservoir in well 16/1-8 (Edvard Grieg Discovery).

The contact models compare different ways to reduce porosity assuming the same lithology. The friable sand line assumes the only porosity reducing factor is passively adding grains in the porespace. The friable sand line shows the sorting trend, as all grains are assumed more or less perfeclty sorted at deposition. With the addition of smaller grains inside the porespace, the sorting deteriorates at lower porosites.

The contact cement assumes uniformly cement growing around the grains. The constant cement lines are drawn from the contact cement line at percentages of porosity reductions (the reduction of porosity here is the cement volume), and interpolated to the mineral point by the friable sand line.

Cement volume estimation is conducted by utilizing the empirically derived, linear fit from Marcussen et al., 2010, which is given by

$$V_P = 86.60 V_{CEM} + 2773.73 \tag{5.3}$$

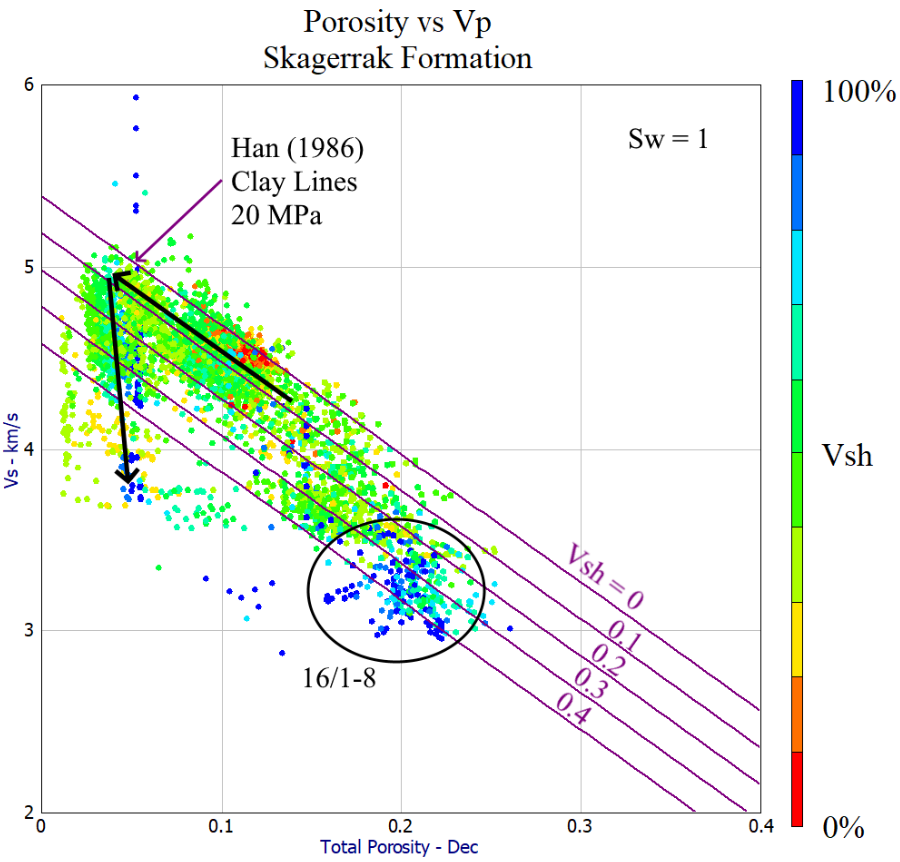

Figure 5.4: ϕ vs V_P crossplot of the Skagerrak Formation in all the wells availible. The Han et al., 1986 clay equations are shown as purple lines, showing the best fit of 20MPa. The transition from grain supported to clay supported matrix is interpreted as described in Marion et al., 1992. The high shale values circled around in the grain supported matrix-region are plotted from well 16/1-8 (Edvard Grieg Discovery).

Table 5.2: Table showing the average cement found by using Marcussen et al., 2010 on the Sleipner- and Skagerrak Formation. The numbers are percentage cement

	16/1-2	**16/1-3**	**16/1-7**	**16/1-8**	**16/1-9**	**16/1-10**	**16/1-12**	**16/1-13**	**16/1-17**	**16/1-18**	**16/1-23**
Sleipner Formation	-	8.11	9.68	-	12.99	-	-	-	-	-	-
Skagerrak Formation	9.94	-	12.17	10.36	9.96	20.82	1.49	14.67	14.67	15.28	16.25

where V_P is given in m/s and V_{CEM} is % cement volume.

It is derived from Etive sands in the northern part of the Viking Graben. As the equation is only dependent on V_P, care should be treated as it can under represent the cement volume when overpressure is present, resulting in a lower V_P for a reservoir. Average cement volumes calculated by Marcussen et al., 2010 for the Sleipner- and Skagerrak Formation is shown in table 5.2.

5.1.2.1 Sleipner Formation

Figure 5.5 shows ϕ vs V_S crossplot from the Sleipner formation in all wells containing pay. Well 16/1-7 (West Cable Discovery) shows deteriorating sorting trend which is correlated with depth. At the lower half of Sleipner Formation cementation starts to heavily increase towards calculated values of up to 30%. Well 16/1-9 (Ivar Aasen Discovery) shows less occurences of extreme cementation with a more dense datapoints yielding large cementation values. Porosity *variatons* seems to be more coupled with deteriorating sorting, while the primary porosity reduction is from cementation. Well 16/1-3 shows a great range in sorting, ranging from almost critical porosity down to poor porosities $\phi < 10\%$.

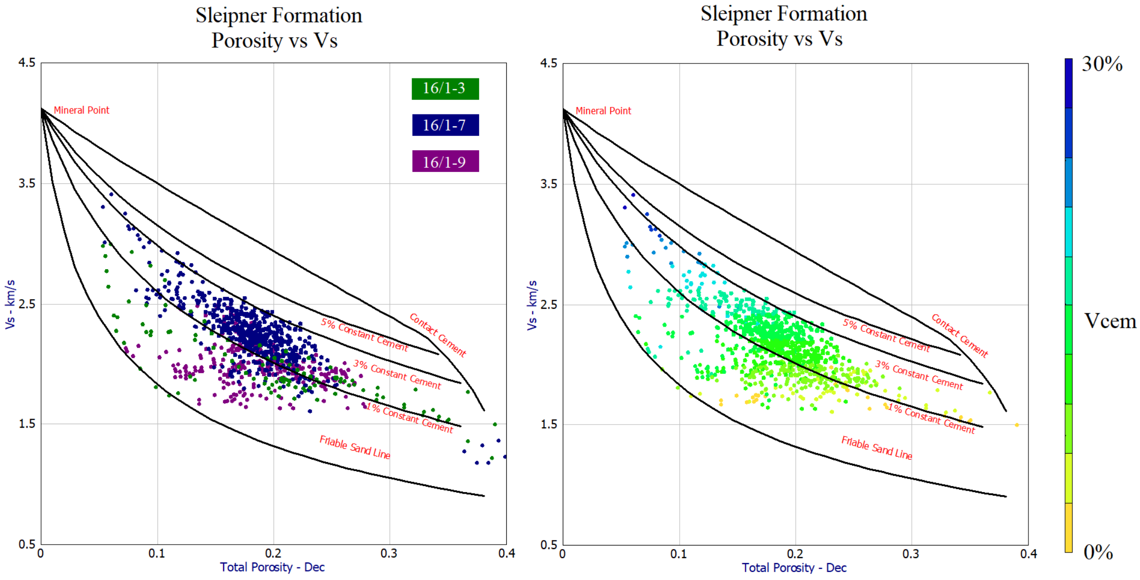

Figure 5.5: Contact model RPT for the Sleipner Formation in three wells. Left hand side shows the distribution of the different wells in the $\phi - V_S$ space, while right hand side is plotted for V_{cem} calculated by Marcussen et al., 2010

5.1.2.2 Skagerrak Formation

Figure **??** shows ϕ vs V_S for the Skagerrak Formation in all wells containing pay. The data is mostly plotted between the friable sand line and the 3% constant cement lines. The calculated cement volume ranges up to 30%, greatly exceeding the constant cement lines. Most of the data plots in towards poorer sorting, with exception from well 16/1-13 (Edvard Grieg 2nd Appraisal) which shows a region of very good sorting. Well 16/1-8 (Edvard Grieg Discovery) shows an increasing cementing line trending across the 1% constant cement line. Well 16/1-10 (Edvard Grieg 1st Appraisal) shows a heavily deteriorating trend, owing to the top of the reservoir having more finely sorted sandstone than then lower conglomeratic section. Well 16/1-23 (Edvard Grieg 5th Appraisal) Shows a heavy cementation ranging up to $30\% V_{cem}$.

5.1.3 V_P/V_S vs AI crossplots

The V_P/V_S vs AI crossplot is used to quality control the petrophysical analysis presented in chapter 4 and help distinguish pore fluids and lithologies. The wells chosen for V_P/V_S vs AI crossplotting are wells situated in the Edvard Grieg field as it contains the most interesting wells containing differing lithology of cap rocks and wildly different sorting. Well 16/1-13 (Edvard Grieg 3rd Appraisal) contains a cross stratified sandstones sealed by the chalk from the Ekofisk Formation while 16/1-23 S (Edvard Grieg 5th Appraisal) conatins a conglomeratic, alluvail fan sandstone sealed by Shale from the Åsgard Formation.

V_P/V_S vs AI RPTs are generated in Hampson Russel. The template is generated by the procedure shown in chapter 3.5.6. Starting with Hertz-Mindlin contact theory at critical porosity, the elastic moduli are interpolated to the mineral point by the use of the lower Hashin Shtrikman bound and subsequently fluid replaced with the Gassmann equation. The density is calculated by the voigt bound.

Figure 5.7 and 5.8 show the V_P/V_S vs AI plots for well 16/1-13 (Edvard Grieg 2nd Appraisal) well 16/1-23 (Edvard Grieg 5th Appraisal). The effective dry mineral components are calculated by the lower Hashin Shtrikman bounds. From the spectral gamma ray logs, the sandstones show large potassium values indicating a very feldspar rich reservoir. Mahmic et al., 2018 indicate feldspar dominated clasts in the conglomeratic sandstone reaching around 50% which, together with V_{sh} estimated from

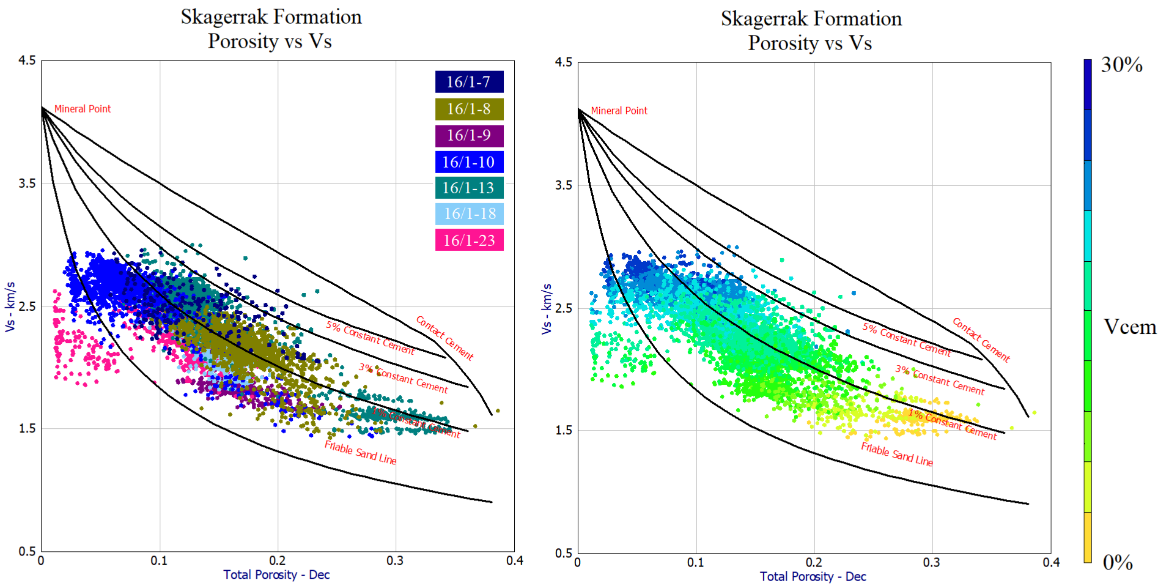

Figure 5.6: Contact model RPT for the Skagerrak Formation in 7 wells. Left hand side shows the distribution of the different wells in the $\phi - V_S$ space, while right hand side is plotted for V_{cem} calculated by Marcussen et al., 2010

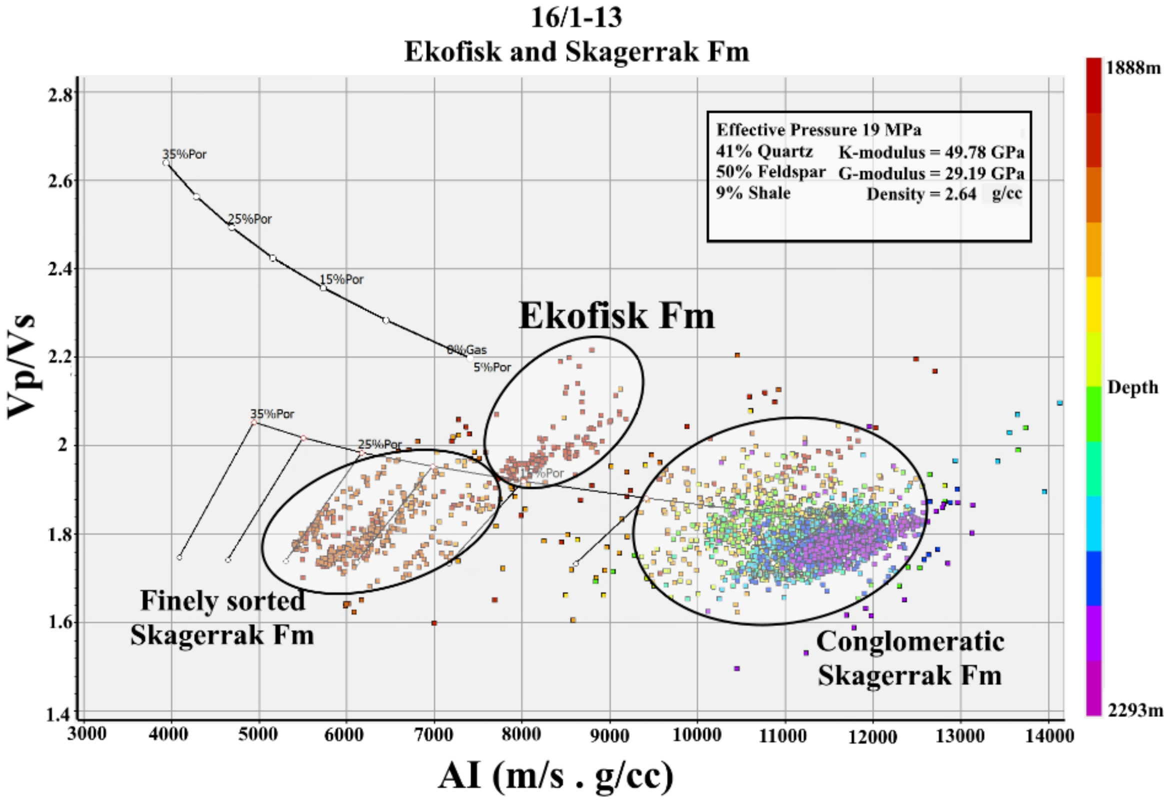

Figure 5.7: Figuer showing the diferent formations and depth plotted in V_P/V_S vs AI for well 16/1-13 (Edvard Grieg 2nd Appraisal).

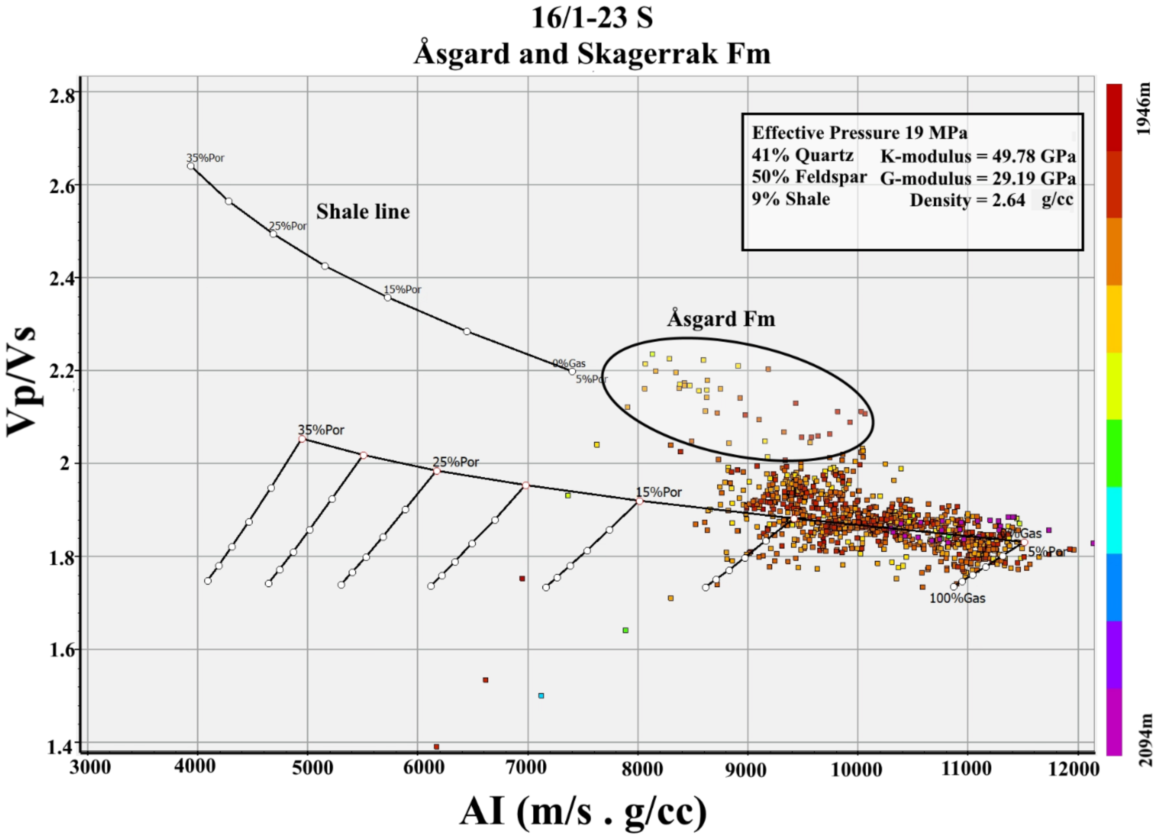

Figure 5.8: Figuer showing the diferent formations and depth plotted in V_P/V_S vs AI for well 16/1-23 (Edvard Grieg 5th Appraisal).

petrophysical analysis shows a very good fit with the reservoir. The remaining matrix constiuents of the reservoir are that of quartz.

The Åsgard Formation devaited from the shale line, possibly due to inclusions of limestone which both have higher densities and V_P, making the cap rock trend to the left in the V_P/V_S vs AI space.

The Ekofisk Formation in well 16/1-23 (Edvard Grieg 5th Appraisal) shows

Additional V_P/V_S vs AI crossplots color coded for volume of limestone is shown in the appendix (C.1 and C.2).

5.1.4 LMR

LMR (Lambda-Rho vs Mu-Rho) rock physics template is disu. The LMR crossplot helps differentiate between lithologies and cementation by cutoffs defined by Goodway et al., 1997. The porous gas sand cutoff is defined at $\lambda\rho = 20GPa \cdot g/cc$. The cutoff for differentiating between carbonates and silisclastic rocks are defined at $\lambda\rho = 100GPa \cdot g/cc$.

The general trend of the LMR is that for increasing gas, the incompressibility defined by $\lambda\rho$ decreases significantly below the threshold, while the rigidity is unaffected. Shales are plotted in the medium values of incompressibility, but low values of rigidity, due to their flaky geometry (Goodway et al., 1997), (Simm et al., 2014). Sandstones are plotted with medium incompressibility and rigidty, with an increase in both of these values with increasing cementation (Goodway et al., 1997).

5.1.4.1 Sleipner Formation

LMR color coded with pay is shown in figure **??**. This reservoir shows a gas cap in the upper part, spanning 8m. Selecting all values inside the Goodway et al., 1997 cutoff for porous gas sands, helps detect levels of pay not detected in the petrophysical analysis. In fig **??**, the cutoff for the porous gas sands nicely correlates to the pay identified expect in the red circle marked in the figure. The

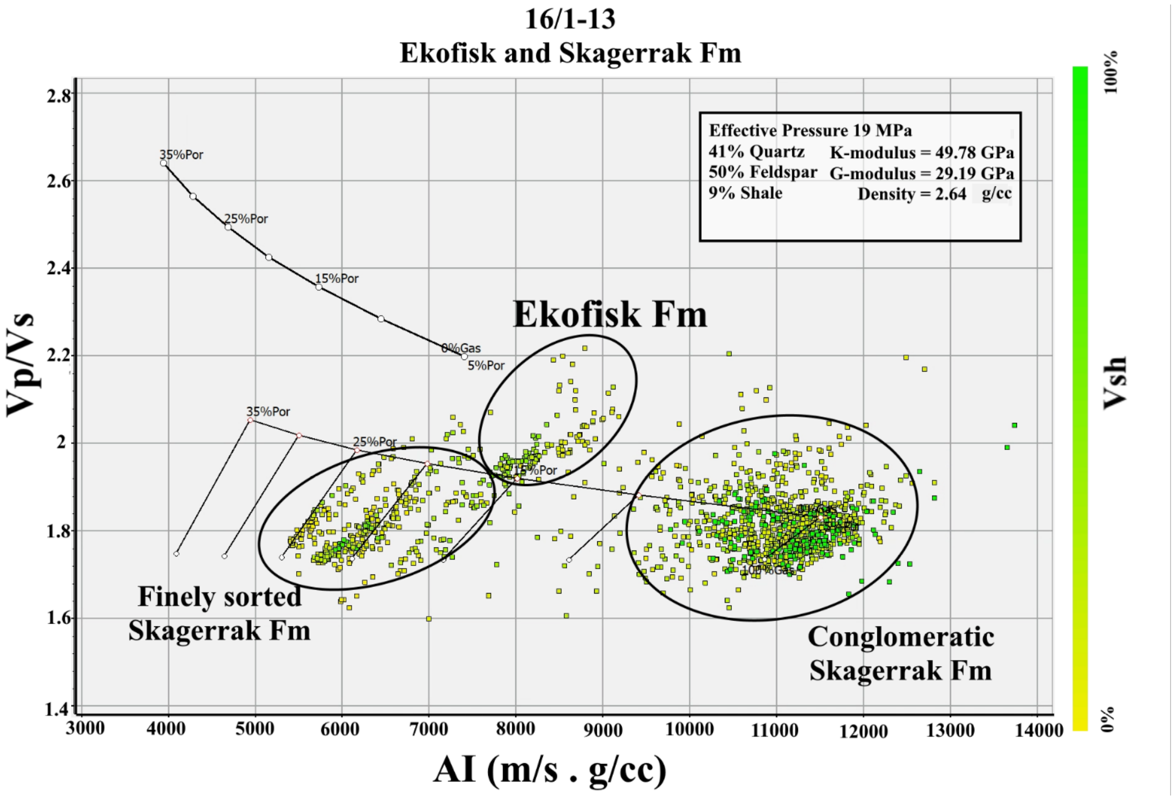

Figure 5.9: Figuer showing the diferent formations and depth plotted in V_P/V_S vs AI for well 16/1-13 (Edvard Grieg 2nd Appraisal).

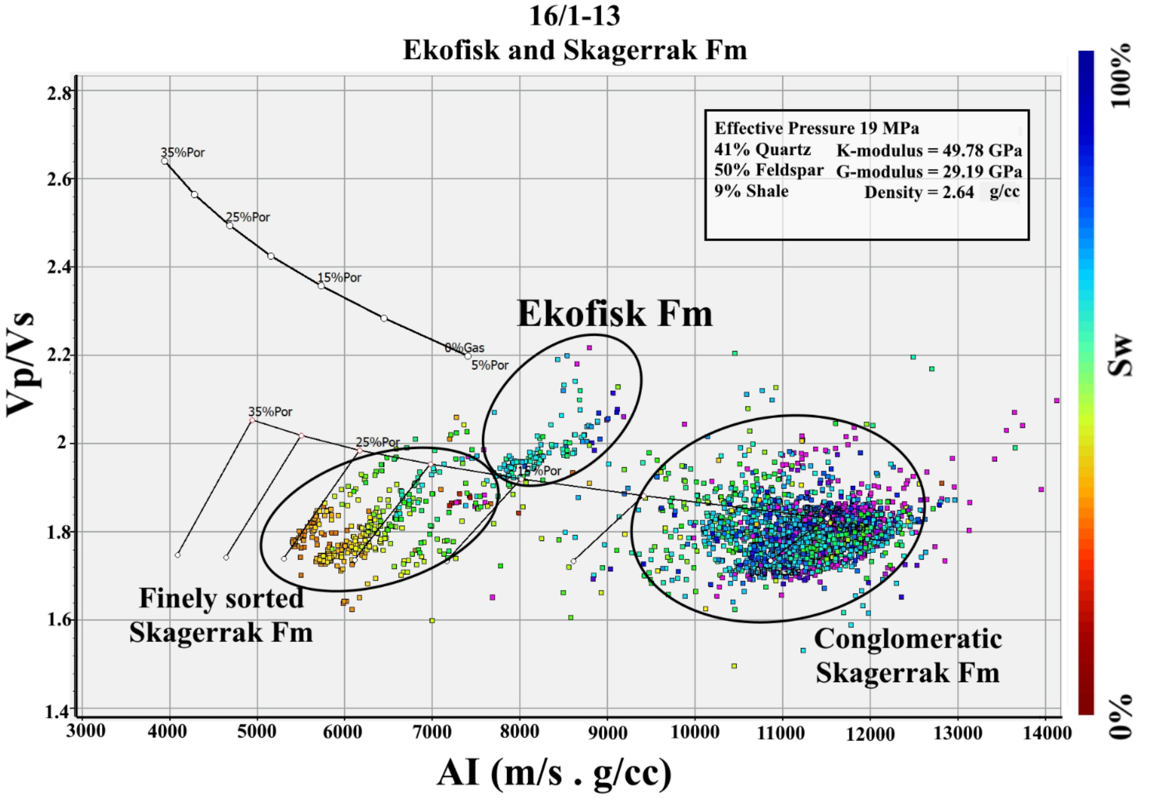

Figure 5.10: Figuer showing the diferent formations and depth plotted in V_P/V_S vs AI for well 16/1-13 (Edvard Grieg 2nd Appraisal).

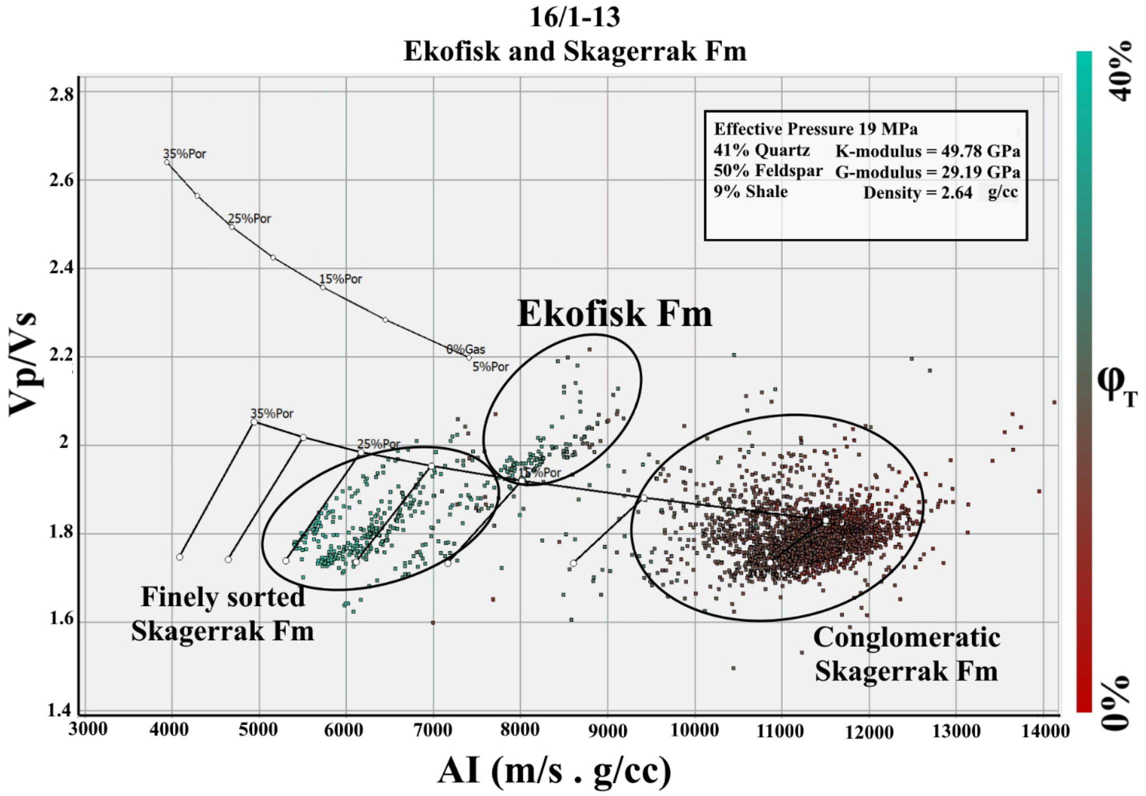

Figure 5.11: V_P/V_S vs AI for well 16/1-13 (Edvard Grieg 2nd Appraisal). Color coded for shale volume.

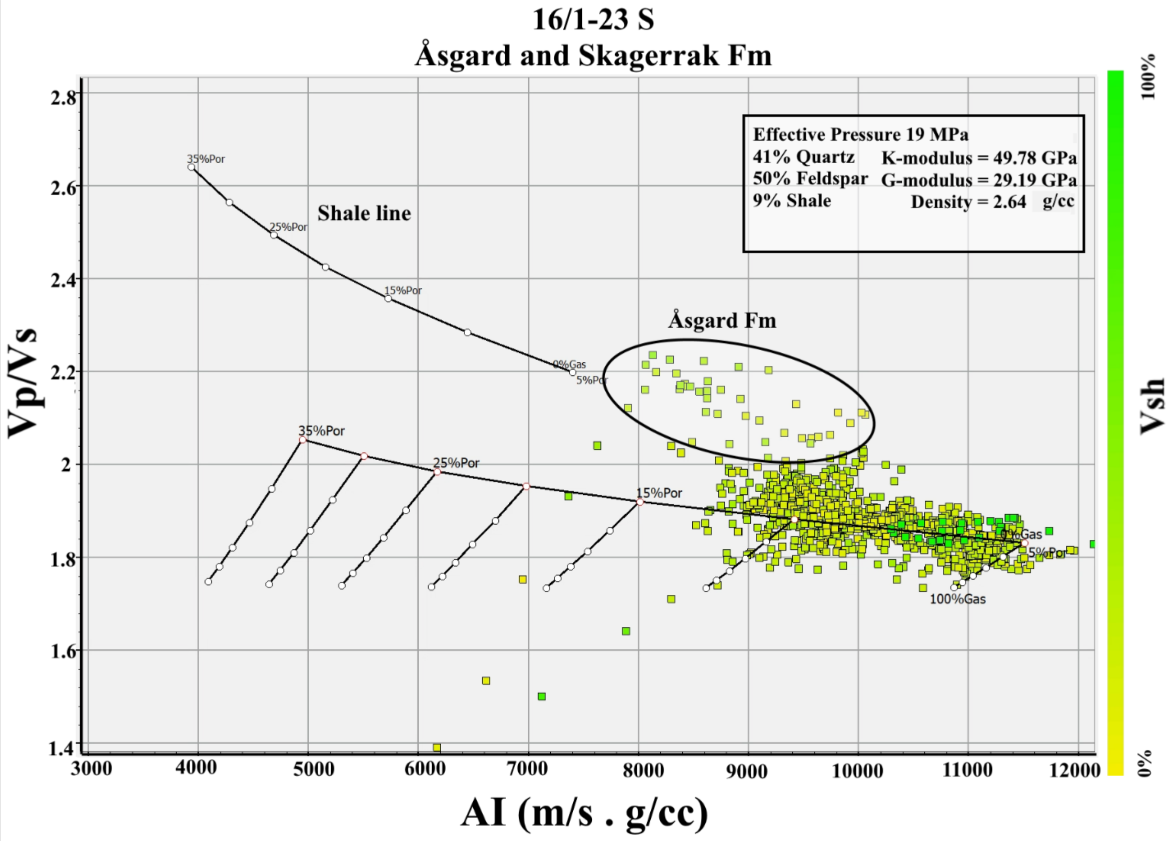

Figure 5.12: V_P/V_S vs AI for well 16/1-23 (Edvard Grieg 5th Appraisal). Color coded for shale volume.

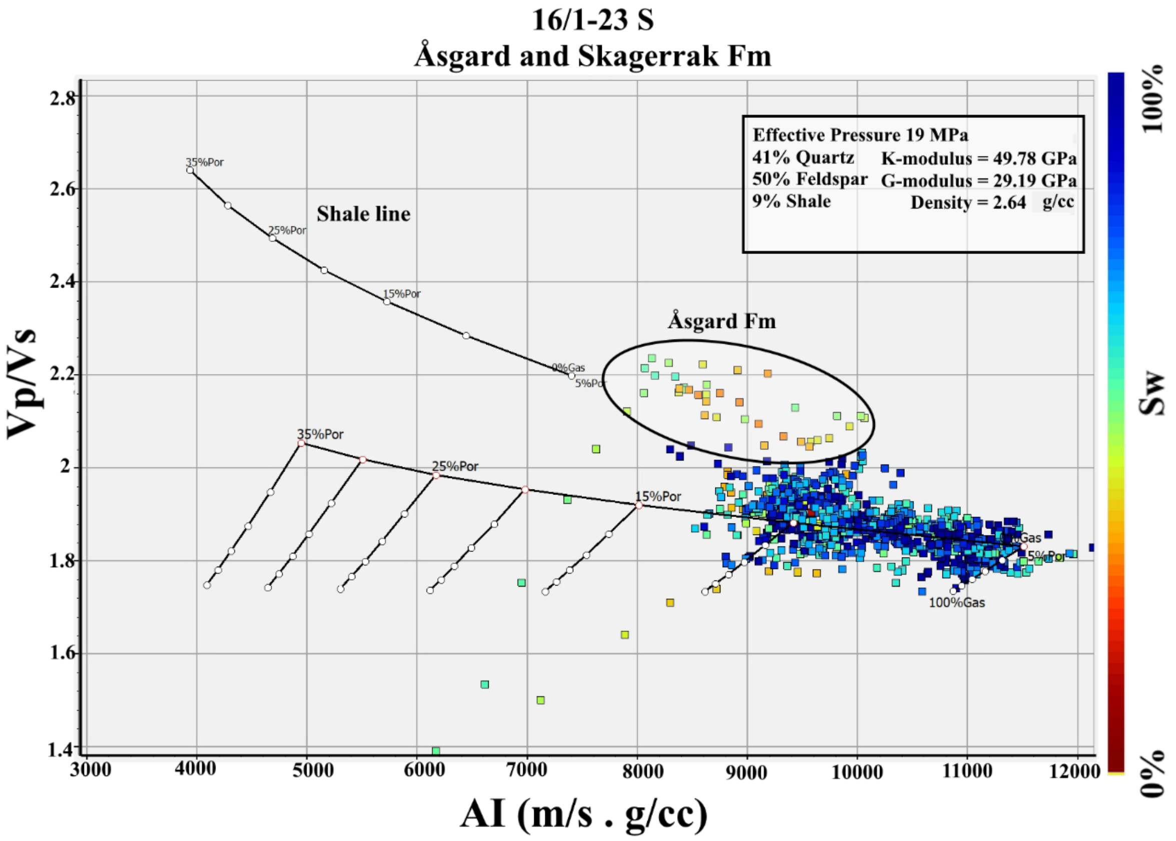

Figure 5.13: V_P/V_S vs AI for well 16/1-23 (Edvard Grieg 5th Appraisal). Color coded for shale volume.

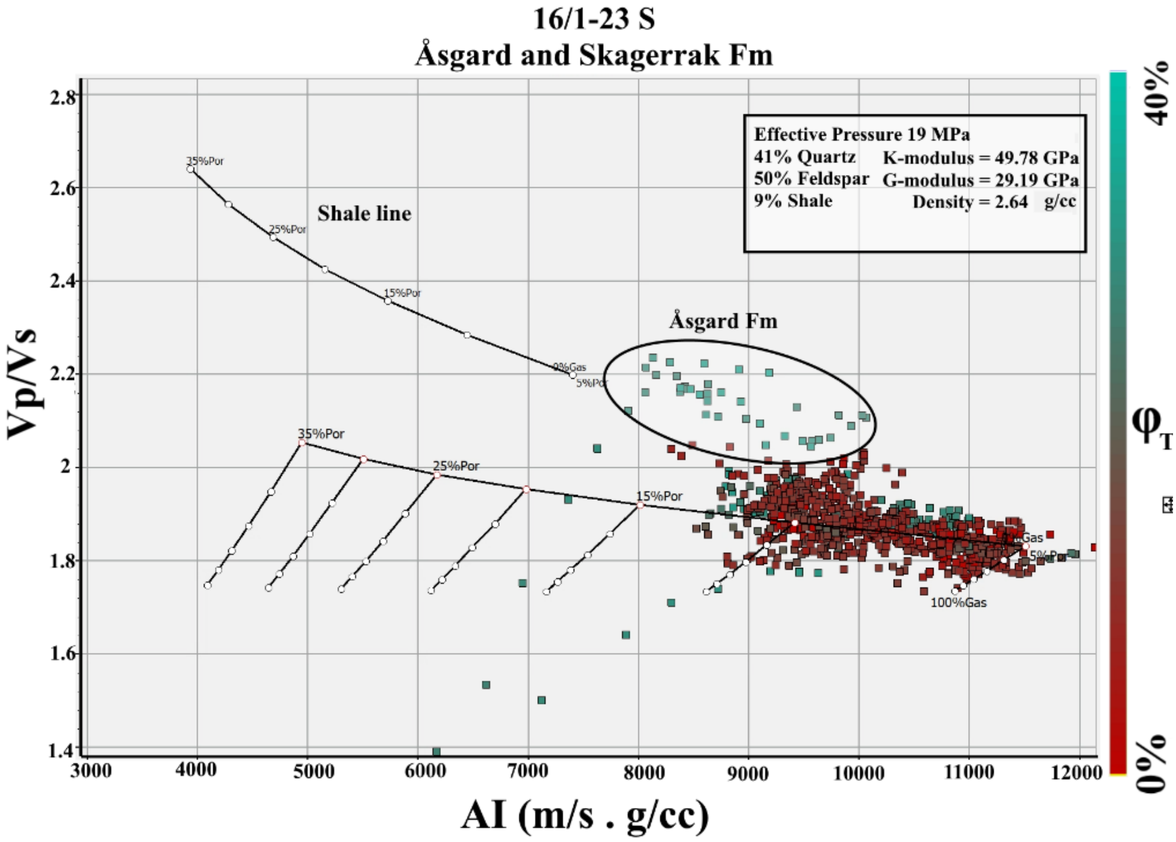

Figure 5.14: V_P/V_S vs AI for well 16/1-23 (Edvard Grieg 5th Appraisal). Color coded for shale volume.

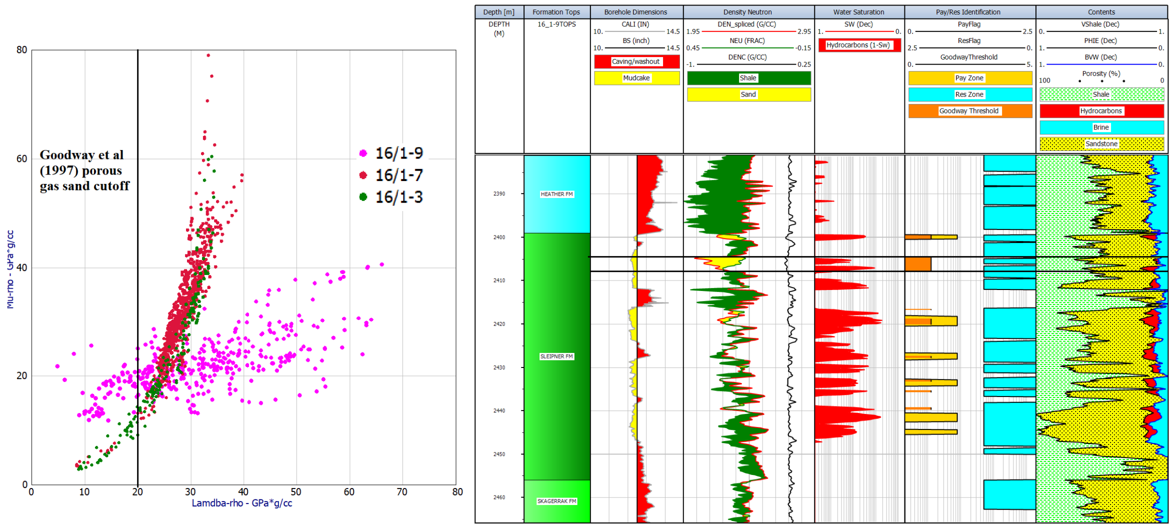

Figure 5.15: LMR crossplot well 16/1-9 (Edvard Grieg Discovery). Datapoints within the Goodway et al., 1997 cutoff for porous gas sands (left side) are extracted as pay flags in the well log (right side).

interval correpsonds to the large separation in the neutron-density log combination, but the resistivity log missed this.

Figure 5.16 shows the LMR crossplot for 16/1-7 (West Cable Discovery). The well was missing V_S and was estimated by the regression found from V_S vs V_P data (eq. 5.1).

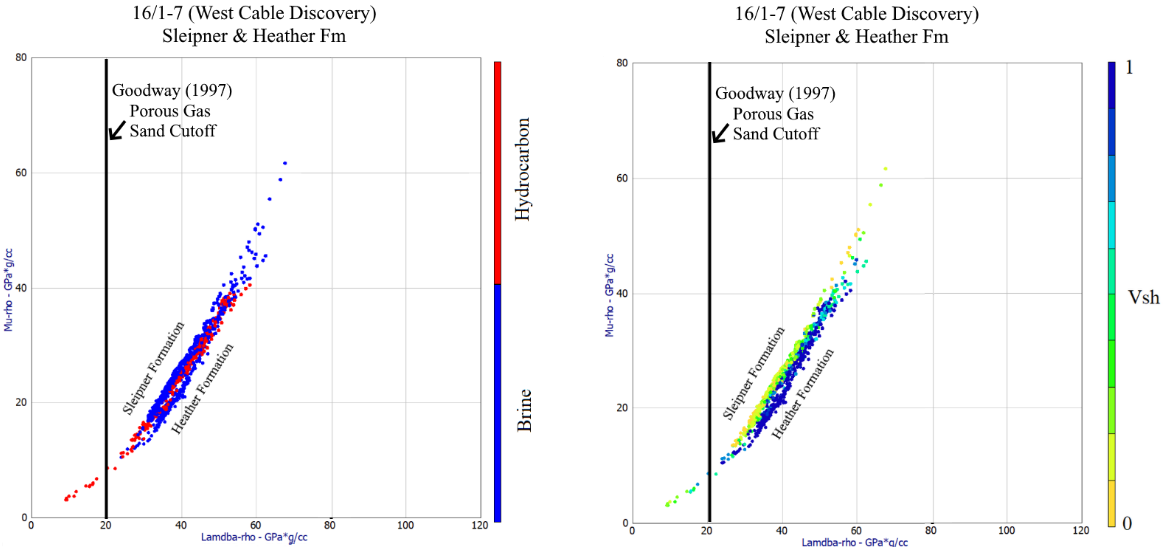

Figure 5.16: LMR crossplot well 16/1-7 (West Cable Discovery). Lef side color coded for water saturation, right hand side color coded for V_{sh}.

5.1.4.2 Skagerrak Formation

The Skagerrak Formation is plotted in the LMR crossplot as seen in figure 5.17 and 5.18. The cementation trend is calculated from heavily increasing incompressibility and rigidity. The Åsgard Formation and the Hod Formation are plotted on different sides of the reservoir trend. The chalky Hod Formation is shown to contain high values of shale, resulting in being plotted under the 100 $\lambda\rho$ threshold for carbonates. The Åsgard Formation is plotted below the Skagerrak Formation in the LMR space with large amounts of shale present. It is plotted as brine saturated, and the datapoints crossing the porous gas sand cutoffs are from depths of bad borehole environments right above the reservoir which the Gardners Equation could not fully compensate for.

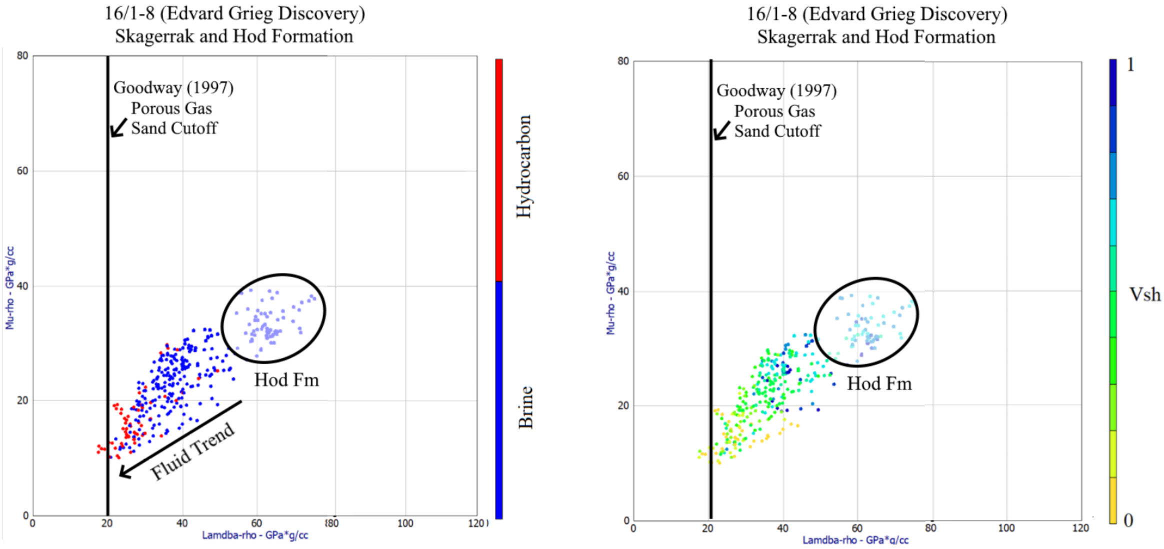

Figure 5.17: V_P/V_S vs AI for well 16/1-23 (Edvard Grieg 5th Appraisal). Color coded for shale volume.

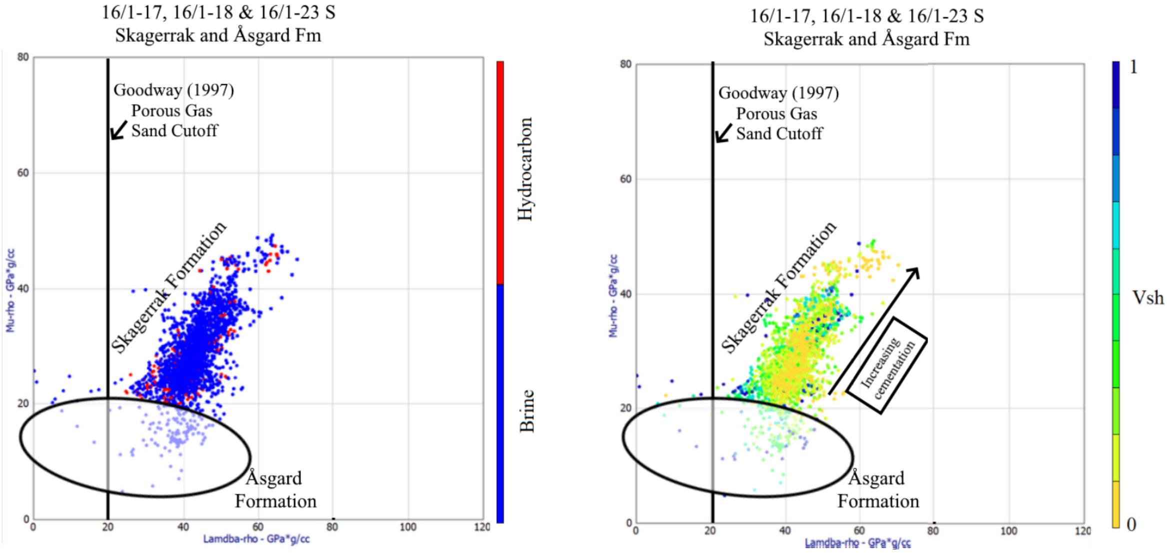

Figure 5.18: LMR crossplot for well 16/1-23 (Edvard Grieg 5th Appraisal). Color coded for shale volume.

5.2 Discussion

This subchapter discusses the results shown in the previous chapter 5.1 with regard to reservoir quality and validation of petrophysical analysis done in chapter 4. Effects of shale volume, pressure, fluid sensitivity and porosity reduction due to compaction and cementation on will be discussed below.

5.2.1 Shale volume and lithology

Estimating shale volume from Han et al., 1986 clay equations did not give a good fit. The arkosic nature of the Skagerrak Formation provides very large values of gamma ray possibly distorting the shale volume estimation. Well 16/1-8 (Edvard Grieg Discovery) did not contain spectral gamma to correct for the possibly high Potassium contents of reservoir, suggesting a more cleaner sandstone than first estimated. The effective pressure of the Skagerrak Formation was

Calculation of Han et al., 1986 clay equations on the Sleipner Formation (figure **??**) was also complicated as NPD, 2021c reports wildly differing effective pressure in the 16/1-7 (West Cable Discovery), $\approx$ 17MPa, and 16/1-9 (Ivar Aasen Discovery), $\approx$ 6MPa.

V_P vs ϕ worked poorly for controlling shale volume given Marion et al., 1992 lines of increasing shalyness. Uncertainties in V_{sh} estimations are evident from a very arkosic sandstone possibly owing to the lacking of SGR in well 16/1-8 (Edvard Grieg Discovery). The transition from grain supported to clay supported matrix in the ϕ vs V_P crossplot was not easily distinguishable.

The LMR crossplot of the Edvard Grieg field showed a clear distinction between the shales of the Åsgard Formation and the chalky Hod Formation, being plotted on the lower and upper side of the reservoir trend, respectively. The Hod Formation did contain shale which constrained it from exceeding the carbonate cutoff. The same trend is also visible in the V_P/V_S vs AI crossplots, where the caprock of Åsgard Formation and Ekofisk Formation does not match with the shale line, trending more towards the reservoir.

Well 16/1-13 (Edvard Grieg 2nd Appraisal) and 16/1-23 S (Edvard Grieg 5th Appraisal) were plotted in the V_P/V_S vs AI crossplot. The Ekofisk and Åsgard Formations were the cap rocks, interpreted to be repsectively chalk and shale from the petrophysical analysis. The Åsgard formation contained large amounts of limestone, shifting the cap rock datapoints in the V_P/V_S vs AI space closer to the sandstone line. This is due to the carbonates exhibiting larger seismic velocities.

5.2.2 Compaction

The estimation of the cementation from Marcussen et al., 2010 showed very high values for the Skagerrak Formation, with cementation ranging from 1.49% to up to a mean of 20.82%. The quantified cement volumes showed better results for the Sleipner Formation which is situated at larger depths. Possible explanataions for these unreasonable values could be unability for the method to deal with carbonate cement in the Skagerrak Formation. It is also worth mentioning that the Sleipner Formation in the Ivar Aasen field shows signficant overpressure with an effective pressure of 5MPa in well 16/1-9 (NPD, 2021c). This results in a decreased V_P, even for very low porosites (Bjørlykke, 2015b), which results in a lower quantified cement volume. The Sleipner formation is also situated deeper than the Skagerrak Formation which should yield larger cementation.

Most of the wells did not show any significant uplift, and therefore the depths of which cementation have occured is more easily contained. The 70°C boundary, estimated from the geothermal gradient calculated from the bottom borehole temperature, are found to be:

- 16/1-2 (Ivar Aasen Field): 2028m BSF
- 16/1-7 (West Cable Discovery): 1822m BSF
- 16/1-8 (Edvard Grieg Discovery): 1765m BSF
- 16/1-9 (Ivar Aasen Discovery): 1959m BSF
- 16/1-10 (Edvard Grieg 1st Appraisal): 1930m BSF
- 16/1-13 (Edvard Grieg 2nd Appraisal): 1744m BSF
- 16/1-15 (Edvard Grieg 3rd Appraisal): 1585m BSF
- 16/1-18 (Edvard Grieg 4th Appraisal): 1635 – 1876m BSF*
- 16/1-23 (Edvard Grieg 5th Appraisal): 1635 – 1876m BSF*

The wells marked with * are wells where the bottom hole temperature was absent. The ranges are therefore calculated from the 95% confidence intervals of the geothermal gradient from wells in the Edvard Grieg field.

The cementation and sorting trends as dominant porosity reducing processes is shown in the fig 5.6 and 5.5. The contact models indicate that the Skagerrak Formation that well 16/1-23 shows very poor sorting, while the remaining trends have cementation to be the most porosity reducing factor.

5.2.3 Fluid sensitivity

Fluid sensitivty is difficult for oil saturated reservoir, especially in the Edvard Grieg field which can show poor to fair porosites in the poorly sorted conglomeratic part of the reservoir.

V_P vs V_S provided difficulties in separation of hydrcarbon. Low porosities in the conglomeratic unit of the Skagerrak formation constrains the separation. Additionally the bulk modulus of oil is more similiar to brine than gas, limiting the possible separation. Well 16/1-7 containing a 9m gas cap that shows a glimpse of a clear separation.

Data points in the V_P/V_S vs AI can be distorted by trends discussed in chapter **??**. Increased shale content or larger pressures moves the datapoints in the opposite direction of increasing hydrocarbon saturation which can mask the fluid sensitivity

Fluid sensitivty in the LMR crossplot are more visible with the porous gas sand cutoff from Goodway et al., 1997. Oil bearing sands plots with lower rigidity.

LMR completely fails to distinguish oil saturation in the basement owing to the non-sedimentary origin resulting to wrongly applied RPTs.

5.3 Uncertainties

Uncertainties regarding the workflow and results from the rock physics diagnostics that should be known to the reader are

- The models are assumed on high porosity sandstones being isoptropic and linearly elastic.
- Assuming under compaction that all grains experience the same stress
- For unconsolidates sands, Hertz Mindlin theory is violated as the pressure is assumed only in the vertical direction.
- V_P/V_S vs AI crossplots require input parameters regarding effective pressure, coordination number and lithology. The effective pressure is estimated from overburden and the pore pressure provided by NPD, 2021c. Coordination number is calculated by the Muprhy, 1982. The lithology compostion is estimated from
- Cement volume estimation from Marcussen et al., 2010 may show severe errors in regions of overpressure or large presence of hydrcarbons.
- RPT created with an effective pressure of 10MPa
- Clay lines from Han et al., 1986 use clay volume instead of V_{sh}. Clay is a component of the V_{sh} and is therefore used to portray overall trends in the data.
- Rock Physics Diagnostics are heavily influenced by the interpretator as the analysis is carried out visually. The quality control and sensitivity analysis is done with respect to outline general trends in lithology, compaction, diagensis and fluid content.

CHAPTER 6

AVO Modeling

6.1 Results

This subchapter presents the results from AVO analysis for selected wells of the dataset by employing AVO forward modelling conducted in Hampson Russell. Fluid effects, compaction/diagenisis and lithology effects on the multi-depositional skagerrak formation and the Ivar Aasen field is explored. Fluid contacts are examined were present but is not prioritized. The selected wells for examination are presented in figure ??, with top and base interfaced for each well presented in table 6.1. Note that well 16/1-17 was dry and the fluid contacts used are top and base of the reservoir unit to mimic the spatially close 16/1-18.

Table 6.1: Overview of fluid interfaces for the AVO forward modelling presented in this chapter. "Green" wells are contained in the Edvard Grieg field, "orange" are Ivar Aasen field. (*Since well 16/1-17 is dry, fluid substitution is computed in the whole Skagerrak Formation).

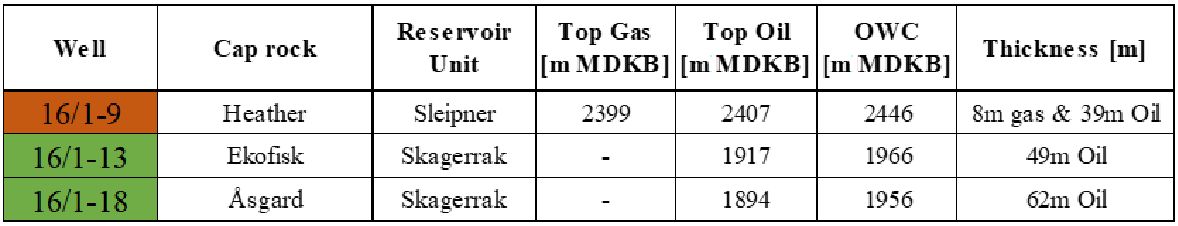

Well	Cap rock	Reservoir Unit	Top Gas [m MDKB]	Top Oil [m MDKB]	OWC [m MDKB]	Thickness [m]
🟧 16/1-9	Heather	Sleipner	2399	2407	2446	8m gas & 39m Oil
🟩 16/1-13	Ekofisk	Skagerrak	-	1917	1966	49m Oil
🟩 16/1-18	Åsgard	Skagerrak	-	1894	1956	62m Oil

The wells within the Edvard Grieg field are green. The AVO Forward Modelling aims to study the fluid sensitivty for the different reservoir characteristics, cap rocks and porosities. Compaction study of well 16/1-13 (Edvard Grieg 3rd Appraisal) is also conducted.

6.1.1 Synthetic seismic generation

The generation of synthetic seismic is discussed in chapter 3.6.1 and this chapter will build upon the more practical side in relation to the data set. Selection of wavelet, blocking size and -method, modeling algorithm and gradient-intercept equations are accounted for below. Examples provided through the discussion is taken from 16/1-13 (Edvard Grieg 3rd Appraisal).

6.1.1.1 Selection of wavelet

The wavelet used in generation of synthetic seismic is generally extracted from real seismic data acquired around the well paths. This is done help the synthetics generated from the borehole to be comparable with the seismic and help in inversion models of the subsurface.

As this study does not have seismic data available, the Ricker wavelet (see figure 6.1), an idealized symmetrical, zero phase will be used. This study will use a dominant frequency of 45 Hz as it is the default setting in Hampson Russell. The phase is linear with a phase rotation of the wavelet is 0 degrees, with a samplte rate of 1ms. The wavelet length is 150.

For the purpose of the AVO forward modeling conducted, the choiche of wavelet is sufficient for investigating the generalized effects from different fluid and compaction scenarios. This study will

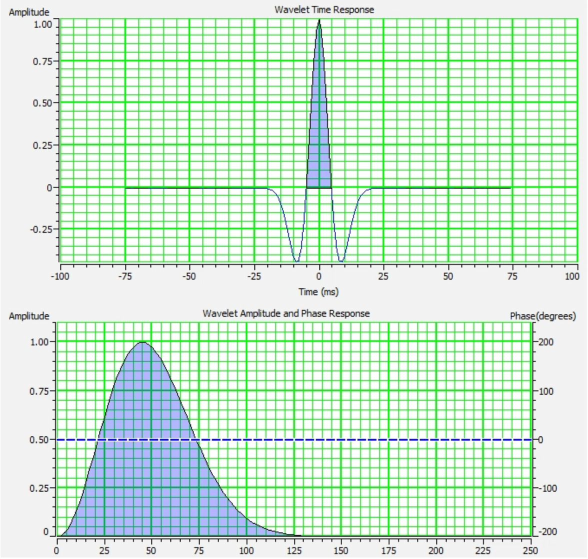

Figure 6.1: The Ricker Wavelet used in this study, displayed in both time and frequency domain. Screenshot from Hampson Russell Software.

use SEG normal polarity, which results in positive amplitudes for an increasing impedance boundary (Simm et al., 2014).

6.1.1.2 Gassmann Fluid Substitution

For the investigation of the fluid effects in the reservoir rocks, Gassmann's fluid substition are used to model different scenarios. The modelling is done by using the Fluid Replacement Modeling (FRM) provided in the Hampson Russell Software. The scenarios tested for each of the wells are 100% brine, 100% oil, 100% gas and 10%. For well 16/1-18, incremental changes in oil saturation from 0% to 100% are modelled. The changes in the seismic properties due to fluid subtition are shown in fig **??**.

Figure 6.3 shows the relative changes in the seismic properties for different fluid scenarios. The Poission's ratio is the most sensitive to any change in fluid content, especially just small inclusions of gas of 10%. The Poisson's ratio also strengthens significantly when the reservoir is fully brine saturated, further stressing how sensitive Poission's ratio is to fluid content. V_P does interestingly show the largest decrease with a smaller saturation of gas than if the pore volume was completely saturation with gas.

The AVO Modelling will investigate fluid substitutions by using gassmann fluid substitution. Different fluid content scenarios are investigate in both their changes to seismic properties and then the AVO response. Figure 6.2 shows how the seismic properties changes with different scenarios. The well data is from well 16/1-13 and displays the sandstone Skagerrak reservoir which is oil bearing. By substituting in 10% gas, 90% brine, the reservoir

6.1.1.3 Blocking and upscaling of well log data

The spatial resolution of well log data is far superior than seismic data with measurements carried out as often as every 2 cm. To bridge the gap between these resolutions when creating synthetic seismograms, upscaling needs to be done. Different blocking methods are used to average over intervals

Automatic uniform blocking method averages the logs between constant intervals and non-automatic uniform selects the intervals, but no smaller than the thickness set, that captures the most significant changes in the well logs based upon maximum likelihood estimation **??**. The backus averaging uses constant intervals but aims to find the average elastic parameters of the rock by taking a harmonic average of the medium. Figure 6.4 shows the blocking of the density log for well 16/1-13. Backus average with a minimum of 15m and 5m captures the reservoir changes best, meanwhile the automatic uniform and especially the automatic non-uniform fails to capture the boundaries of the reservoirs sufficiently. For the AVO forward modelling, the backus average will be used, but with varying blocking size fitted to best capture the boundaries of the fluid contacts.

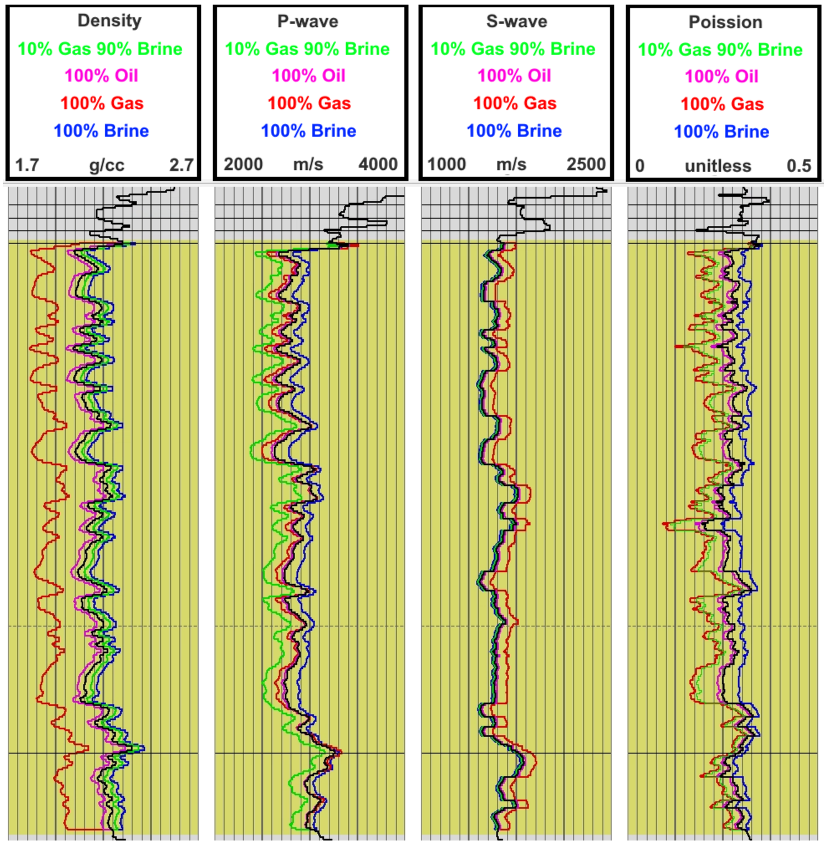

Figure 6.2: Changes in seismic properties with changing fluid content for well 16/1-13. The reservoir is already containing hydrocarbons, which leads to 10% gas scenario yielding a higher density than the in situ.

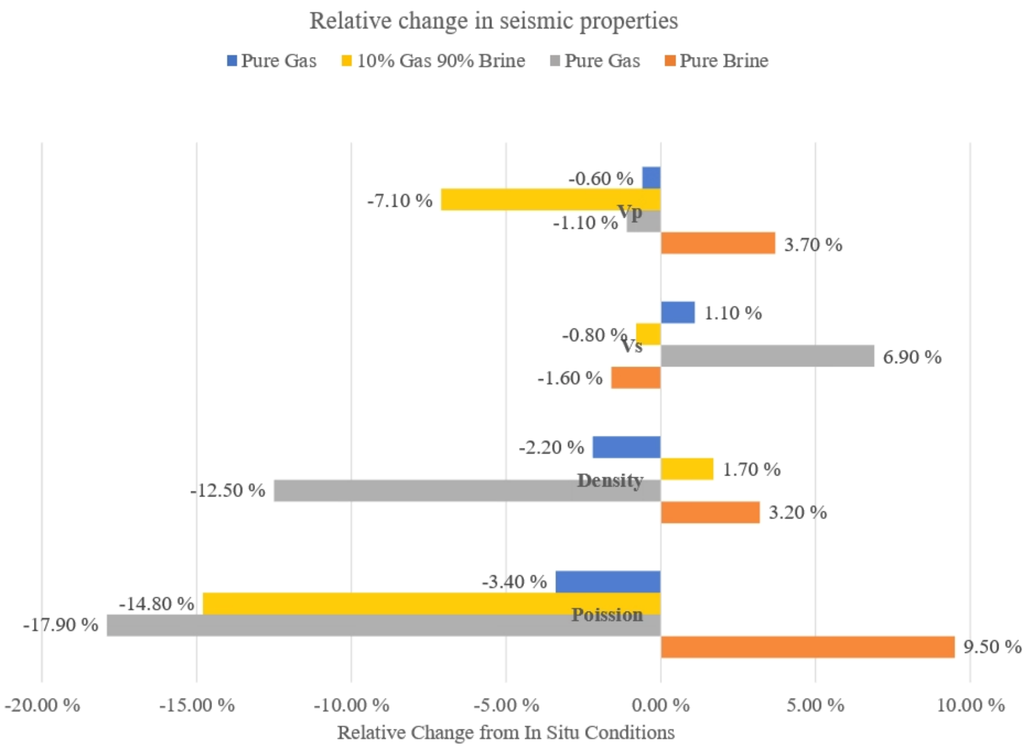

Figure 6.3: Bar plot showing the relative changes from in situ conditions in well 16/1-13 for different fluid scenarios.

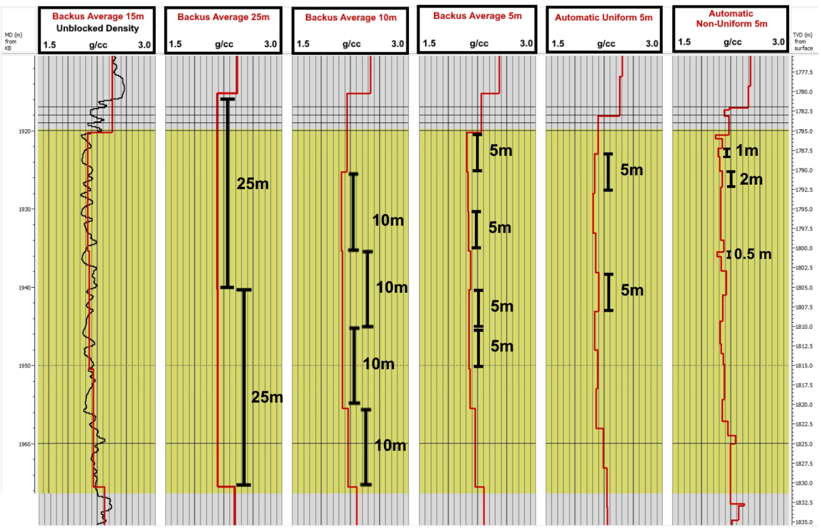

Figure 6.4: Figure showing the density log for well 16/1-13 blocked with various methods. The yellow zone indicates the reservoir which needs to be modelled.

Figure 6.5 shows the intercept gradient plot of the different blocking methods and sizes.

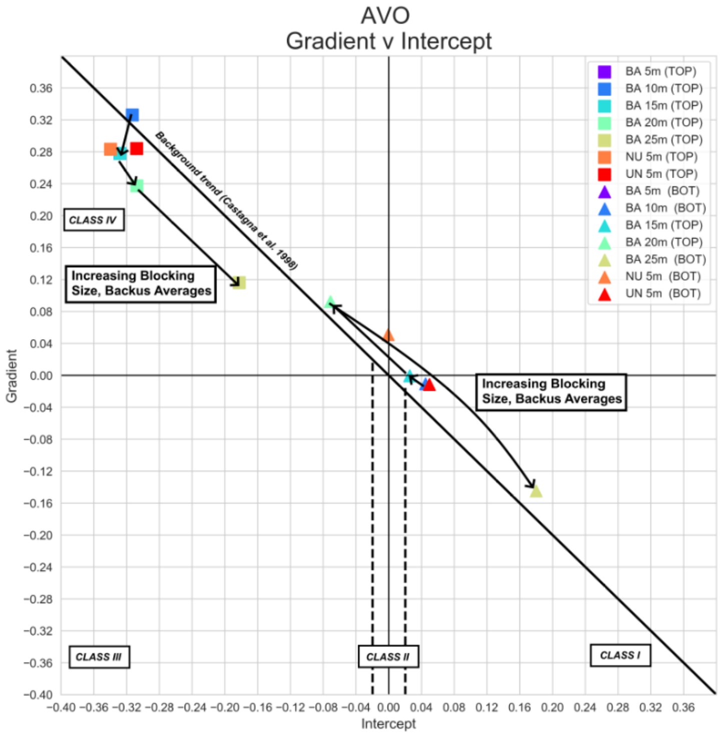

Figure 6.5: Gradient Intercept-plot of fluid contacts with different blocking methods and blocking thicknesses for well 16/1-13. Top is located at top of oil and bot is the OWC.

6.1.1.4 AVO equation and background trend

The algorithm chosen for the synthetic seismic is the Zoeppritz algorithm provided in the Hampson Russell™ software with 15 angles of maximum 30°. The ray path is then calculated by ray tracing. For classification of the AVO-classes, two-term Aki Richards approximation is used, which is valid up to 30°.

Table 6.2: Overview of blocking methods and minimum thicknesses chosen for each well.

Well	Blocking Method	Blocking Size
16/1-9	Backus Average	14m
16/1-13	Backus Average	25m
16/1-18	Backus Average	14m

6.1.2 AVO classification

AVO classification is performed by plotting the top fluid contact and the bottom fluid contact on the Intercept-Gradient crossplot. The intercept and gradient are fitted by the two-term Aki Richards approximation. A total of 5 wells have been selected for AVO-modelling, where each well have been investigated for different scenarios.

6.1.2.1 Fluid sensitivity for well 16/1-9

Well 16/1-9 is the only well in the dataset which contains a somewhat sizeable gas cap. Fluid subsitituion was carried out by firstly removing the gas cap to conform with the reservoir being solely containing oil, before substituting for different scenarios. Figure 6.6 show the in situ conditions with different pore fluid properties plotted.

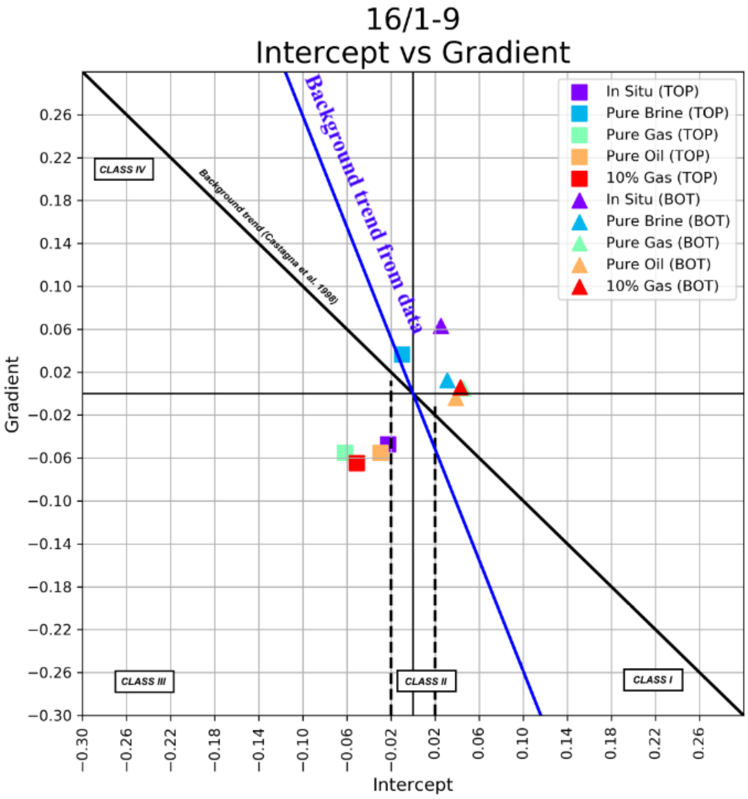

Figure 6.6: Gradient Intercept-plot of well 16/1-9 with top of the reservoir denotes as squares and water contact denoted as triangles.

6.1.2.2 Compaction and diagensis for well 16/1-13

The 16/1-13 has the best reservoir properties in the dataset, owing to aeolian sandstone deposits yielding porosites up to 30%. The cap rock is the Hod and Ekofisk Formations of chalky reservoirs, yielding a great contrast in the seismic properties.

Figure 6.7 shows the Intercept-Gradient cross plot of well 16/1-13 when the reservoir is modeled for decreasing porosity. The reservoir is part of the sandstone part of the Skagerrak Formation and exhibits the highest porosity in the dataset of 30%. The reservoir for insitu is defined at the 30% porosity case. By decreasing the porosity of the reservoir to its more alluvial deposited counterparts, a trend from Class IV to class 2 takes shape, with the largest drop occuring at the change from 10% to 5% porosity.

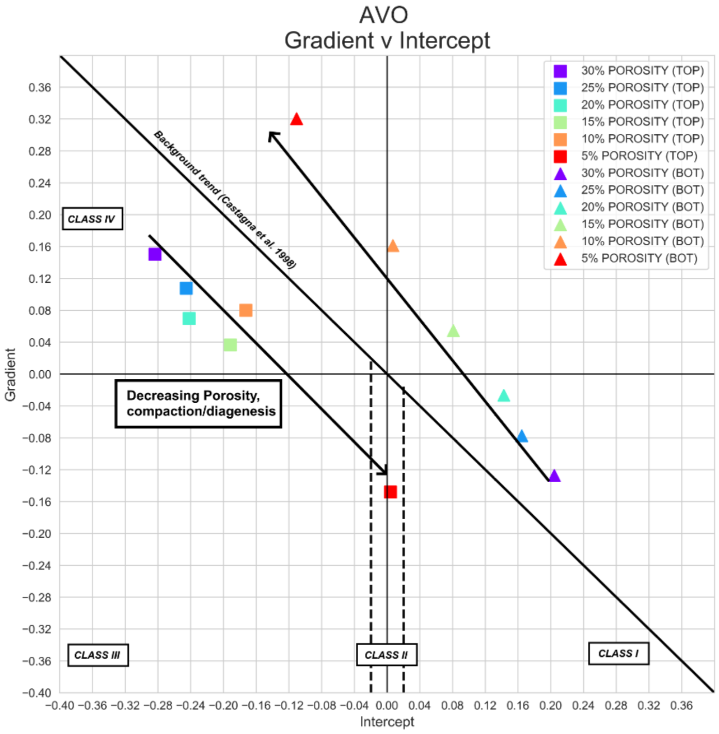

Figure 6.7: Gradient Intercept-plot of fluid contacts with different blocking methods and blocking thicknesses for well 16/1-13. Top is located at top of oil and bot is the OWC.

With decreasing porosity, the amplitudes are dimming towards class II AVO. A similar mirroring effect is observed at the OWC of the reservoir. The greatest reduciton in the AVO response occurs at the lowest porosites.

6.1.2.3 Fluid sensitivity for well 16/1-18

Well 16/1-18 is shown in fig 6.8 with in situ and different fluid saturations. This well contains the conglomeratic part of the Skagerrak Formation, exhibitng very poor to fair values of porosity.

6.2 Discussion

AVO modelling is done to help explain seismic signatures related to different lithology and fluid scenarios. AVO anomalies also aids in detection of hydrcarbon being a direct hydrocarbon indicator (DHI).

Summary of the in situ contacts are shown in figure 6.9 in the I-G space, with compaction and hydrocarbon trend highlighted.

6.2.1 Lithology

The sealing cretaceous successions over the Edvard Grieg field is comprised of large amounts of carbonates, ranging from chalk to marly shales. The (Simm et al., 2014)

6.2.2 Compaction

Porosity show great restrain on fluid sensitivity as shown in the RPTs. The reducing factors of porosity in the dataset is not only diagnesis with increasing depth, but also the degree of sorting. The upper part

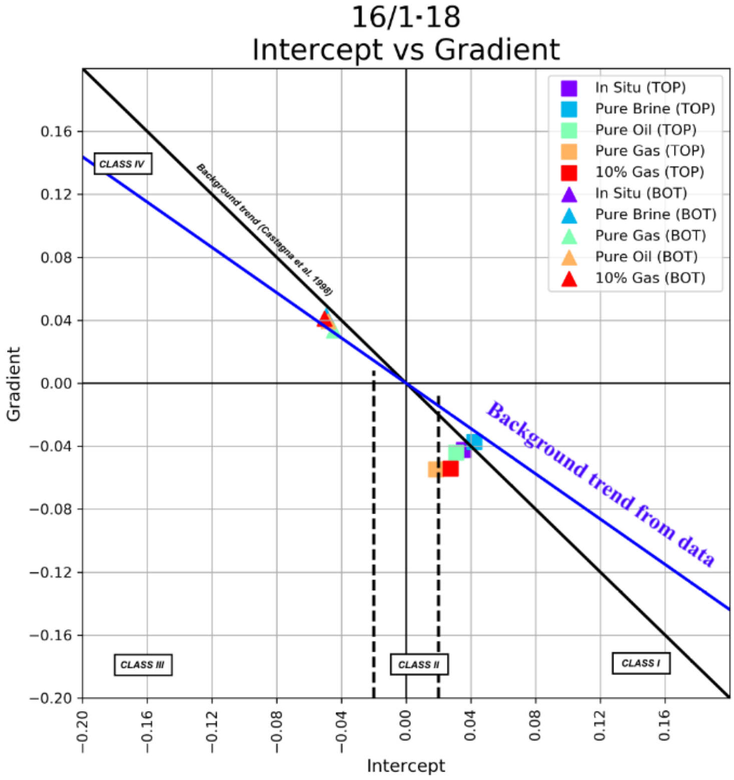

Figure 6.8: Gradient Intercept-plot of well 16/1-18 with top of the reservoir denotes as squares and water contact denoted as triangles.

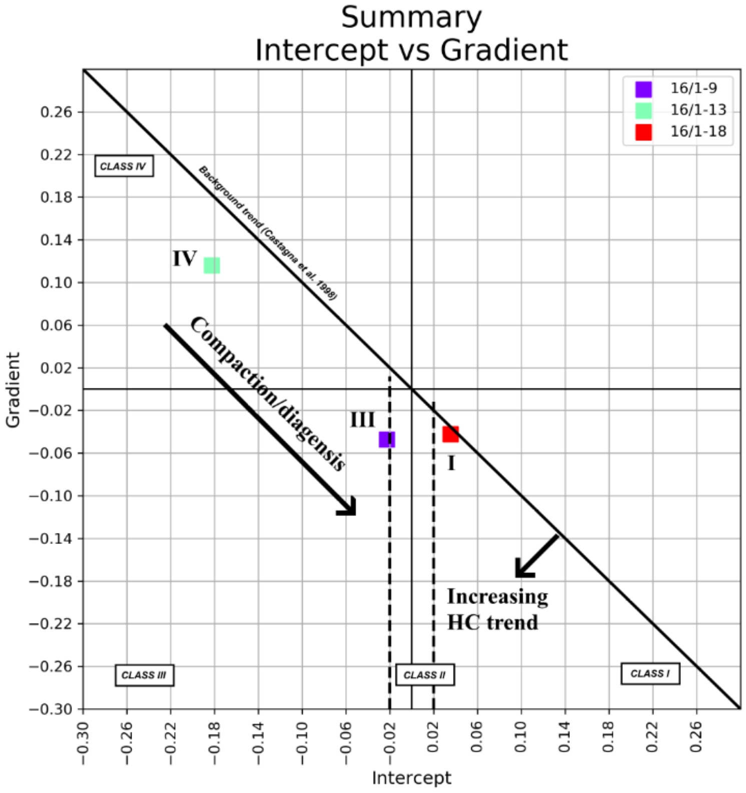

Figure 6.9: Gradient Intercept-plot the wells modelled in this chapter. The Hydrcarbon trend and porosity reducing compaction and diagensis trend is superimposed.

of the Skagerrak Formation shows wildy different sorting dependant on the depositional environment, from the conglomeratic parts of well 16/1-18 to the aeolian sandstones in well 16/1-13.

6.2.3 Fluid Saturation

The increase in hydrocarbon saturation is found to appear perpendicular to the background trend from the in situ data. The incresing oil saturation is shown from well 16/1-18 to be minimal compared to that of gas, as expected from trends.

6.2.4 Bed Thickness and layering

The Åsgard formation overlying the reservoir has been found to have an average thickness of ≈ 5 m over the Edvard Grieg field which is below the tuning thickness of the seismic wavelet (Ndingwan et al., 2018), which can help explain the low intercept gradient responses for well 16/1-18.

6.3 Uncertainties

Uncertainties and limitiations which should be made evident for the reader are

- Intervals of poor well log data. The density log is corrected by Gardners equation in regions of highly deviatoric calliper log but there are no methods used to correct the transit log interval, providing a possible error to the seismic properties and AVO forward modelling.
- The ricker wavelet used is stationary which means it does not change with increasing depth.
- For the synthetic seismic no attentuation of amplitudes or frequency deterioration is presented with increasing depth unlike real seismic. There are also no multiples or noise in the data which again results to a highly idealized seismic trace
- Matrix substition in Hampson Russell for studying increaing shale content did not yield changed seismic parameters and was therefore omitted from this study.
- The limited wells presented in this chapter are due to time constraint as it was lastly prioritized. The wells chosen portray the main distinctive features of the reservoir targets.

CHAPTER 7

Summary and Conclusions

The overall goal of this study was to utilize log well data to characterize reservoirs in the Triassic and Jurassic succsesion of the east western part of Utsira High, block 16/1. Three distinct methodologies have been carried out to analyze the target reservoirs: petrophysical analysis, rock physics diagnostics and AVO forward modelling. The data contained 17? wells, with the first well dating back almost 50 years.

The Jurassic Sleipner Formation of the Vestland Group and the Triassic Skagerrak Formation of the Hegre Group was of most interest, aswell as some minor analysis in the fractured basement and some of the thinly draped Cretaceous formations covering the Utsira High.

The petrophysical analysis gave quantified estimates of shale volume, porosity, water saturation, net-to-gross reservoir and net pay. The neutron-density crossover plot used alongside the gamma ray log to estimate shale volume, while the density and neutron, where availible, were used to calculate porosity. Water saturation was estimated by the use of Archies equation.

The Jurassic Sleipner Formation showed overal better reservoir properties than the Skagerrak Formation as a whole. The Skagerrak Formation was found to be containing a more finely sorted, aeolian unit in the upper part of the utsira high, showing at best up to 30% porosity. It suffered from thickness as it only was visible in well $16/1-13$ and slightly in $16/1-10$. Underlying the aeolian skagerrak was the conglomeratic skagerrak formation, suffering from very poor sorting and drastic decrease in porosity, down to $10-15\%$.

Rock physics diagnostics was conducted to help further understand the degree of compaction, sorting, pore fluids and lithology in the target reservoirs. Reservoir contained within the Edvard Grieg and Ivar Aasen fields were modelled for different rock physics templates and quality controlled with the petrophysical analysis.

AVO forward modelling was selected on 5 of the 17 wells with both distinct and comparable characteristics. Synthetic seismograms were created on blocked well log data to provide the most realistic comparison to pre-stack seismic possible. Caveats are that real seismic contain noise and that the wavelet chosen was the ricker wavelet, which is a highly primitive wavelet. Fluid substituion was carried out to compare different scenarios of pore fluid and their response in the intercept-gradient cross plot. Effects of differing blocking size, changing pore fluids, change of shale volume and compaction are all discussed, including the tuning effects of the thin, cretaceous seals.

Reservoir zones and pay zones were identified by silisclastic cutoff values from the literature. For reservoir zones the requirements were set to effective porosity above $\phi_E \geq 0.06$, shale volume under $V_{sh} \leq 0.5$. For pay identification the additional requirement was water saturation to be $S_W \leq 0.6$.

There was 17 wells in this study and the amount of wells were used variously for their purpose. Thickness maps, uplift estiamtion and depth maps used all well data. The petrophysical analysis constrained the data to wells containing the Jurassic Sleipner Formation (the main reservoir unit in the Ivar Aasen Field), the Triassic Skagerrak Formation (the main reservoir unit in the Edvard Grieg Field) and the basement for wells interpreted to be containing reservoir zones. The rock physics diagnostics was constrained to only wells showing the Sleipner Formation and the Skagerrak Formation and the AVO Forward Modelling extracted a few representative wells from the Ivar Aasen- and Edvard Grieg field to conduct fluid sensitivity analysis.

- The Sleipner Formation found in three wells showed on average larger N/G, larger porosity and lower shale volume than the triassic Skagerrak Formation. However well 16/1-10 and 16/1-13 showed very good porosites in the uppert part of the reservoir.

- Sleipner Formation showed a N/G ranging from $0.484 - 0.713$ with net reservoir ranging up to 76.23m. Shale volume ranged from 0.16 to 0.19, with fair to good porosites. All wells exhibitng approximentaly $7 - 9$ meters of pay.

- The thickness distrubtion of the Sleipner Formation conforms shallows to the South East of the study area, mainly bound by the half-graben on the western part of the Utsira High.

- The Skagerrak Formation showed a N/G ratio ranging from 0.199 to 0.985, with net reservoir up to 276.45m. Reservoir showed fair porosites around $10 - 15\%$. Net pay intervals ranged from 1.22m to 41.61m.

- The basement was found to carry the lowest N/G ratios, ranging from 0.001 to 0.559. The porosity is mostly around 9%, with an exception in well 16/1-4 of 15%. Net pay intervals ranged from 5.79 to 40m when present.

- The thickness distribution of the Skagerrak Formation shows an overal opposite trend of the Sleipner Formation as it thickens across the Utsira High. A possible fault inside the Edvard Grieg field have preserverd a larger column of the Skagerrak formation.

- Cementation volume estimated from Marcussen et al., 2010 provided unrealisticly high values for the Skagerrak Formation, ranging from 1.49 to 20.82% average cement volume. The Sleipner formation also showed large numbers of 8.11 to 12.99% cement volme.

- Spectral gamma ray log was avaible for 7 logs in this study, almost all contained within the Edvard Grieg field. The trendings show The Skagerrak Formation showed mostly continental depositonal environment with high amounts of Potassium. The gamma ray log of the Sleipner formation showed oscillating finings upwards sequence indicative of fluvial delatic depositional environement. The spectral gamma ray log indicated a mix of continental and marine depositon.

- Uplift estimation of the area showed minimal uplift agreeing with estimates from literature.

- Rock physics models such as LMR and V_P/V_S vs AI showed good ability to discriminate between lithology. The data was color coded for shale volume, and carbonate dominated cap rocks were easily spottable by deviation from the shale regions. Ekofisk Formation, Hod Formation and Åsgard Formation showed an mix of shale and carbonates. LMR crossplot helped aid in possible missed pay identification in the Sleipner Formation in well $16/1 - 9$ where water saturation log indicated brine.

- AVO Modelling was performed on 16/1-9 (Ivar Aasen Discovery), 16/1-13 (Edvard Grieg 2nd Appraisal) and 16/1-18 (Edvard Grieg 4th Appraisal). The 16/1-9 (Ivar Aasen Discovery) was classified as a class III AVO anomaly, the 16/1-13 (Edvard Grieg 2nd Appraisal) a class IV AVO anomaly and 16/1-18 (Edvard Grieg 4th Appraisal) a class I anomaly. The class IV anomaly occured with very high porsity sandstone underlain chalk cap rock. The class I anomaly is more typical of the Edvard Grieg field as a whole, with low porosities from conlgomeratic sandstones.

- Porosity and flud saturation trends in the Intercept-gradient crossplot were established from the data. Decreasing porosity plays a huge role in the fluid sensitivity and showed a greater range than increasing fluid content. With modelled compaction, 16/1-13 (Edvard Grieg 2nd Appraisal) trended from a class IV anomaly to a class I anomaly. The fluid saturation of increasing oil showed a very subtle deviation from the background trend due to low porosities.

Appendices

APPENDIX A

Uplift Estimation

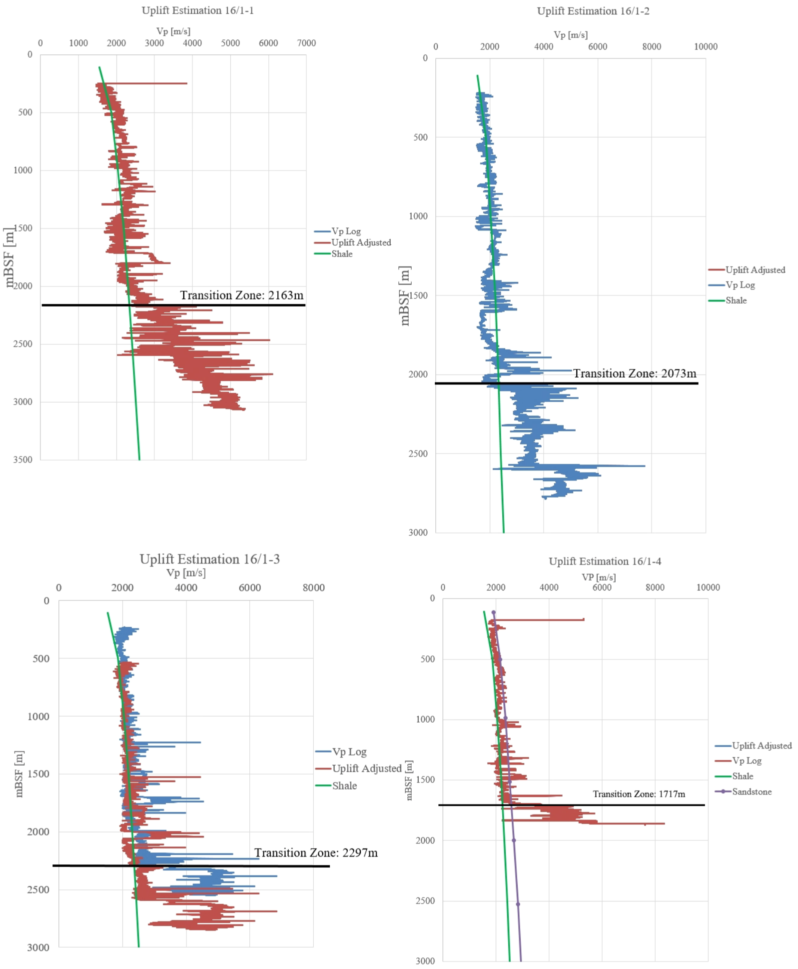

Figure A.1: Uplift estimation of wells () by fitting the V_P log with normal compaction trends from Mondol et al., 2007

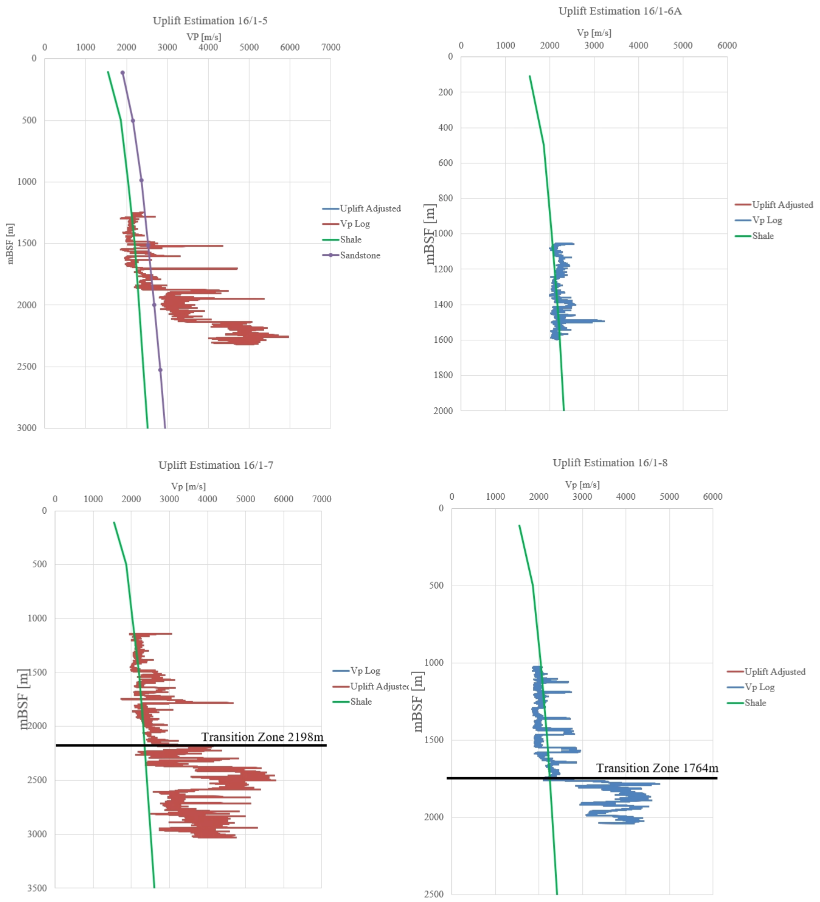

Figure A.2: Uplift estimation of wells () by fitting the V_P log with normal compaction trends from Mondol et al., 2007

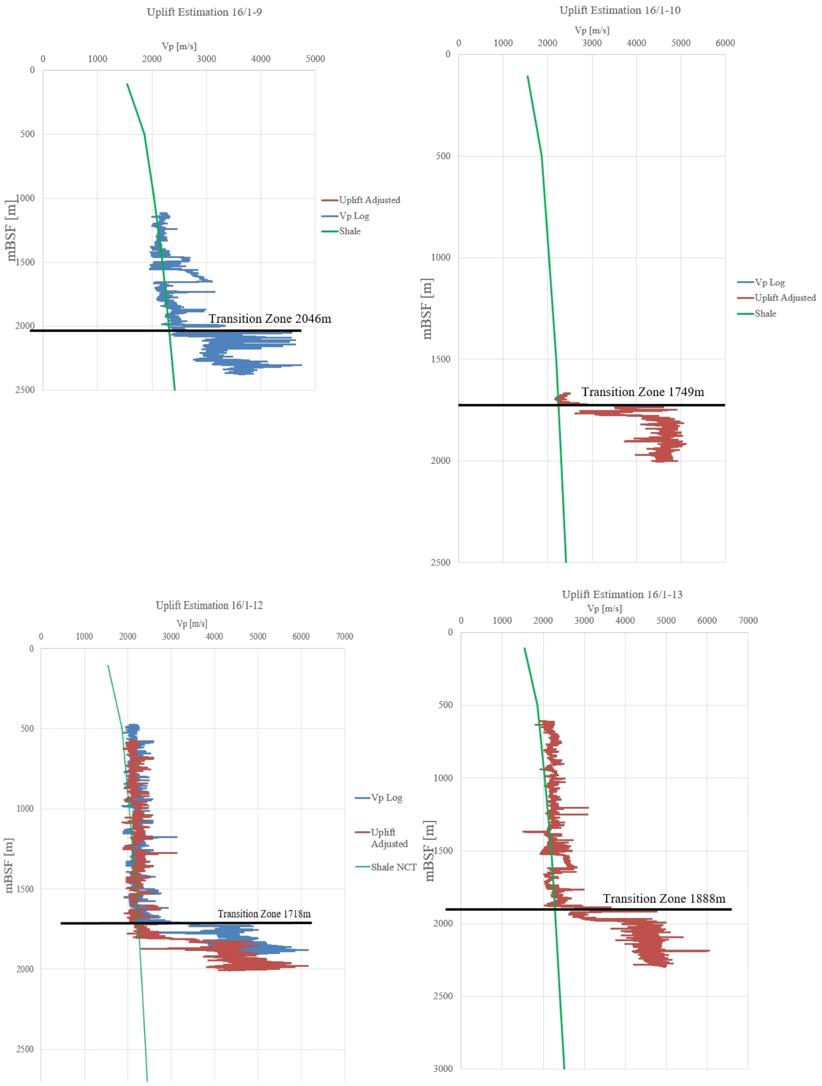

Figure A.3: Uplift estimation of wells () by fitting the V_P log with normal compaction trends from Mondol et al., 2007

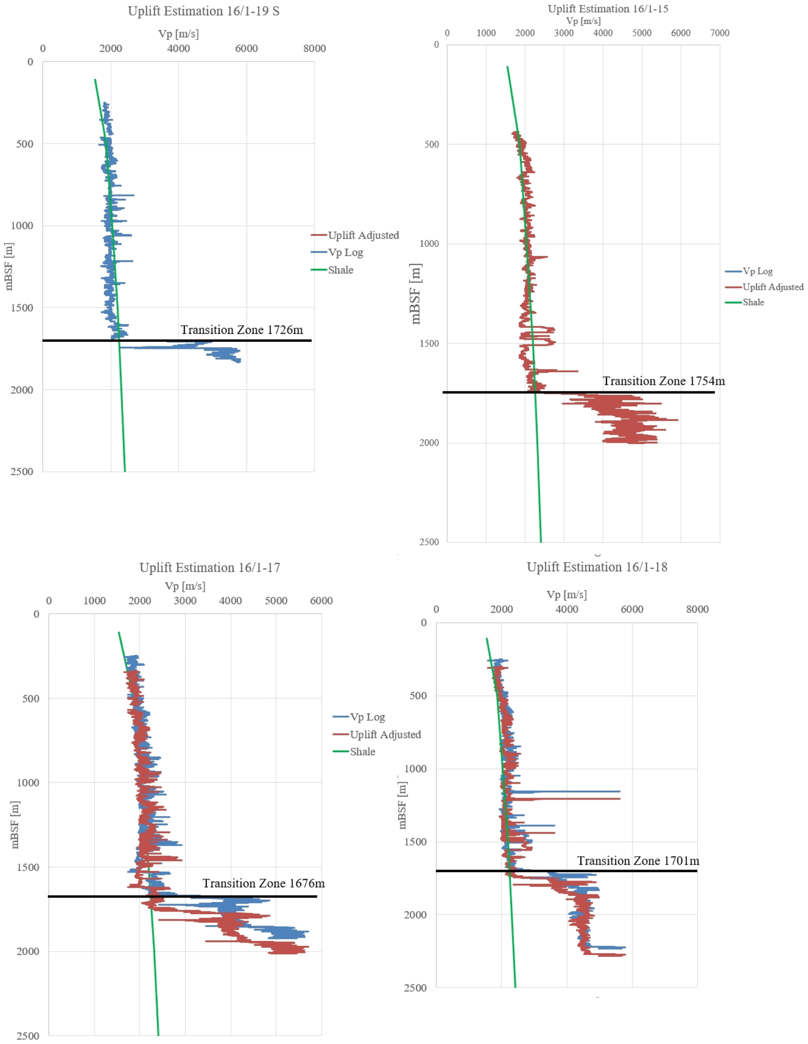

Figure A.4: Uplift estimation of wells () by fitting the V_P log with normal compaction trends from Mondol et al., 2007

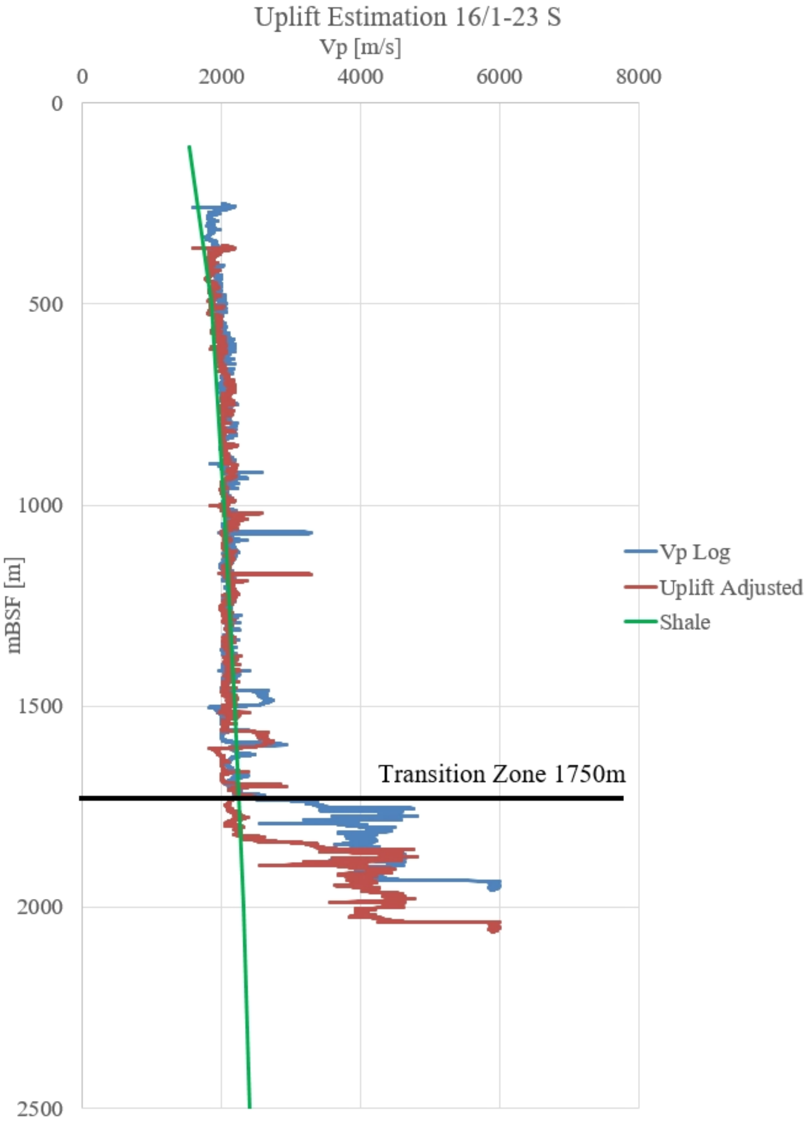

Figure A.5: Uplift estimation of wells () by fitting the V_P log with normal compaction trends from Mondol et al., 2007

APPENDIX B

Well Section

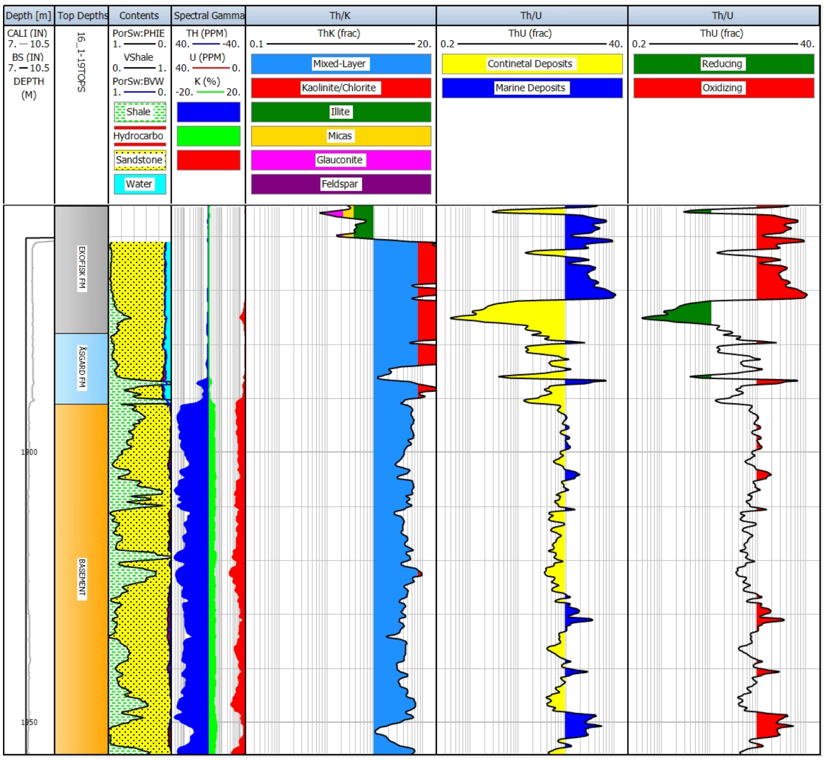

Figure B.1: Track display of well 16/1-19 S (Ivar Aasen 4th Appraisal) the interpreted lithology and fluid contents alongside dominant clay mineral and general determination of depositional regime.

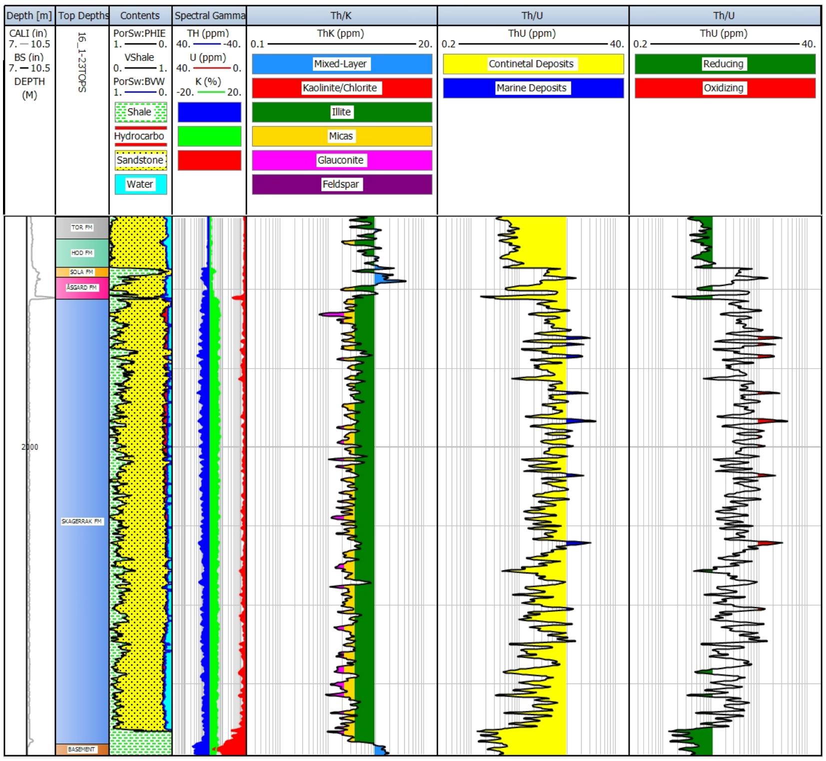

Figure B.2: Track display of well 16/1-23 S (Edvarg Grieg 5th Appraisal) the interpreted lithology and fluid contents alongside dominant clay mineral and general determination of depositional regime.

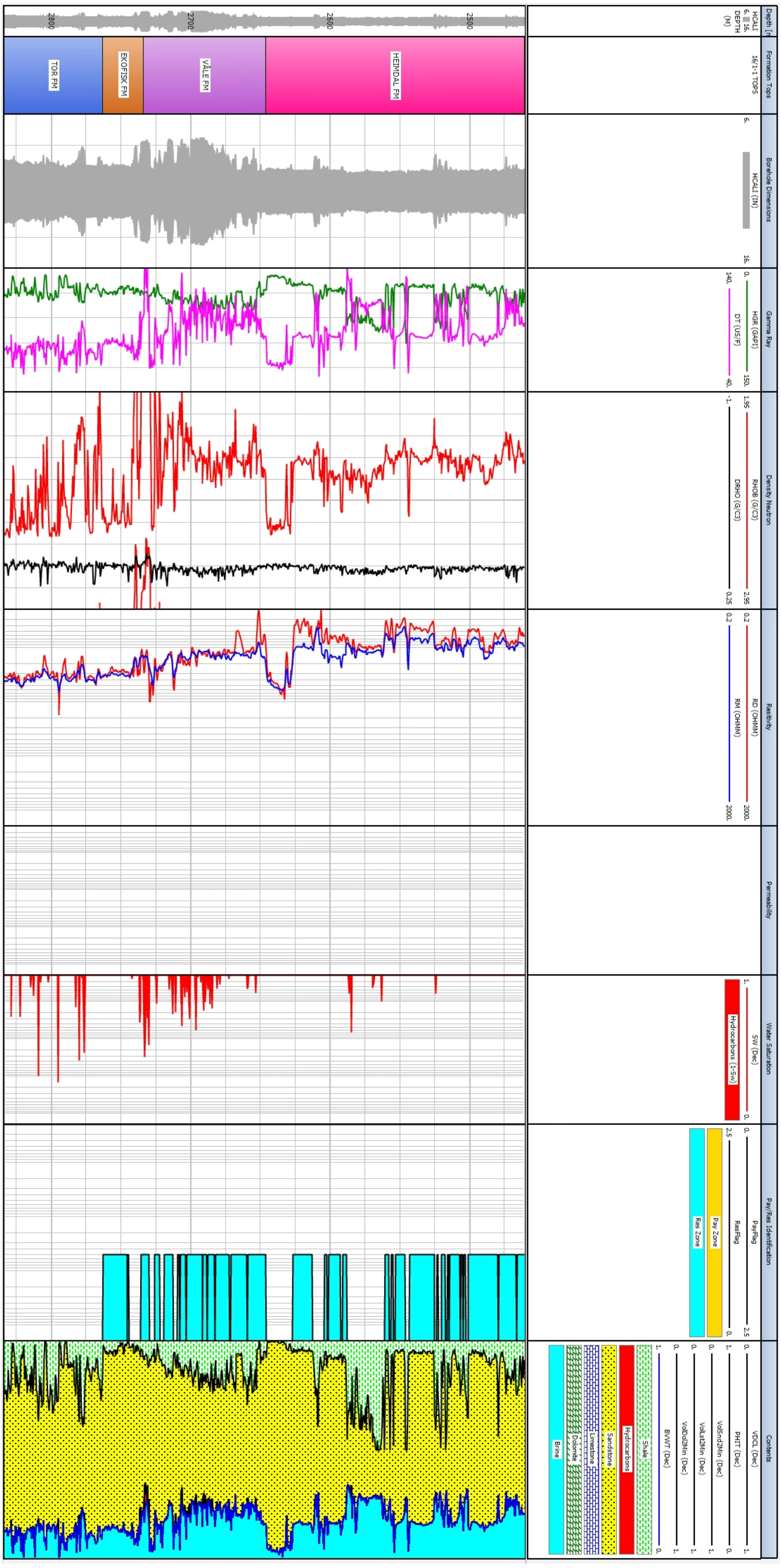

Figure B.3: Petrophysical overview of well 16/1-1

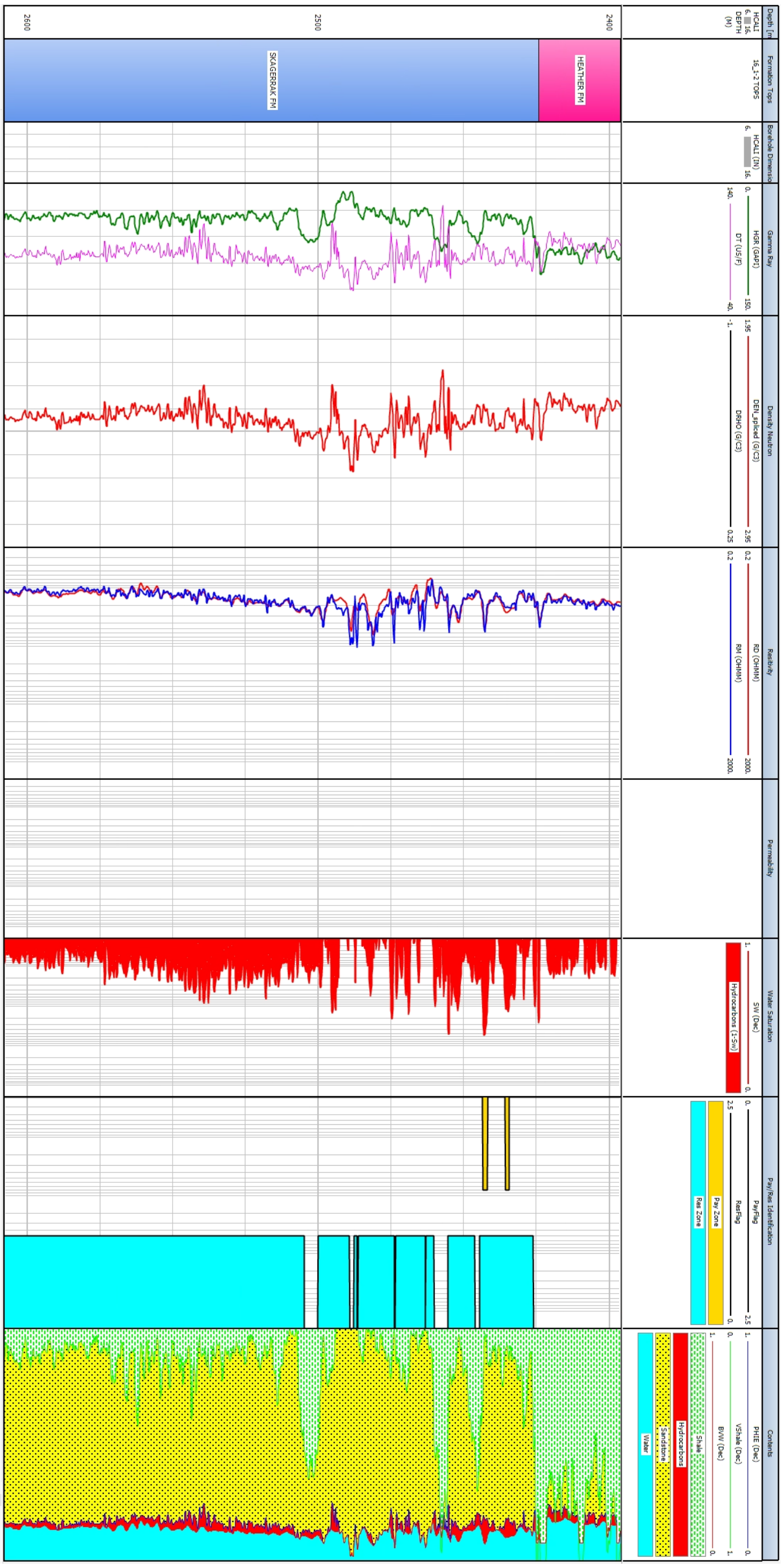

Figure B.4: Petrophysical overview of well 16/1-2

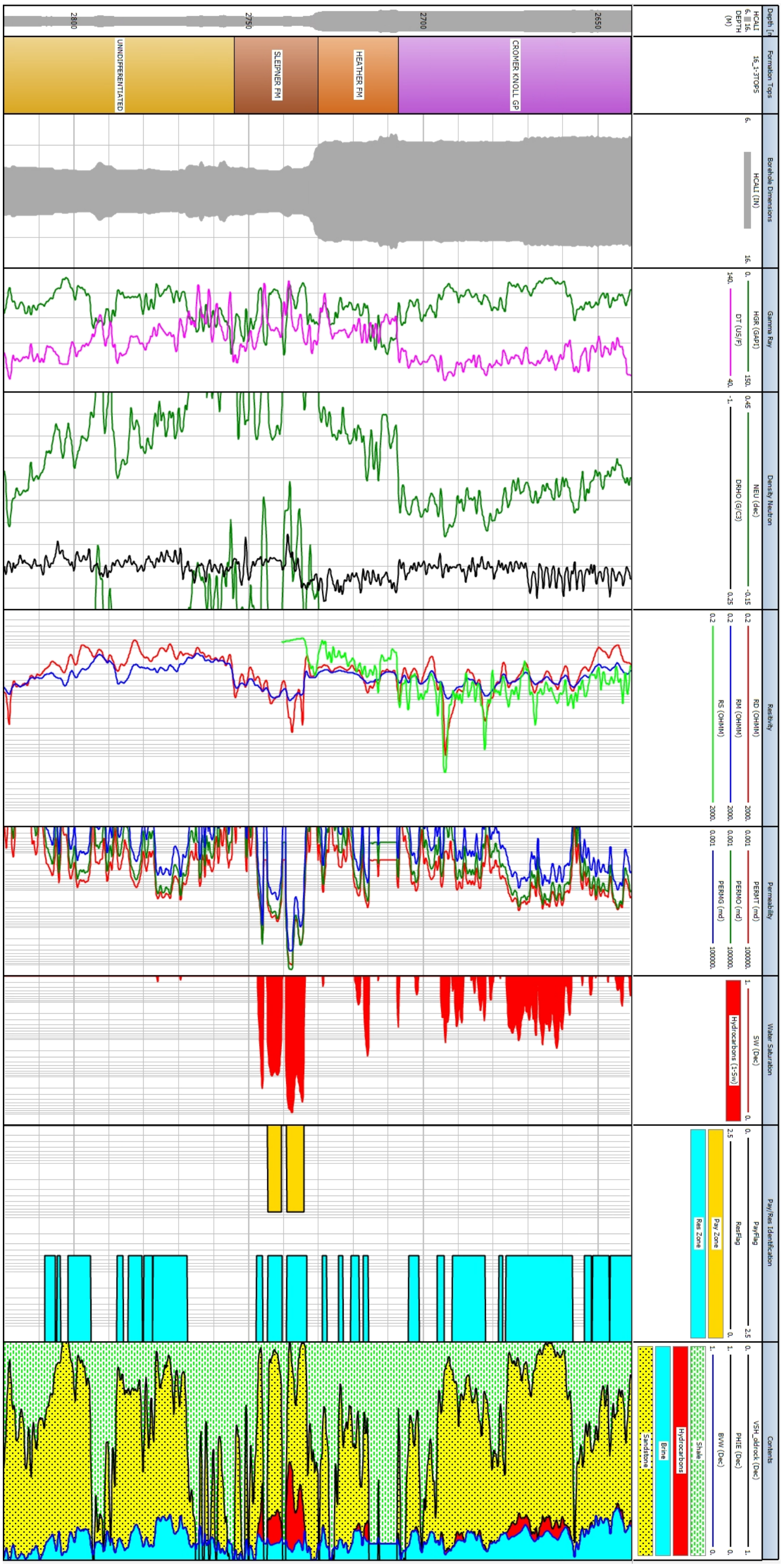

Figure B.5: Petrophysical overview of well 16/1-3

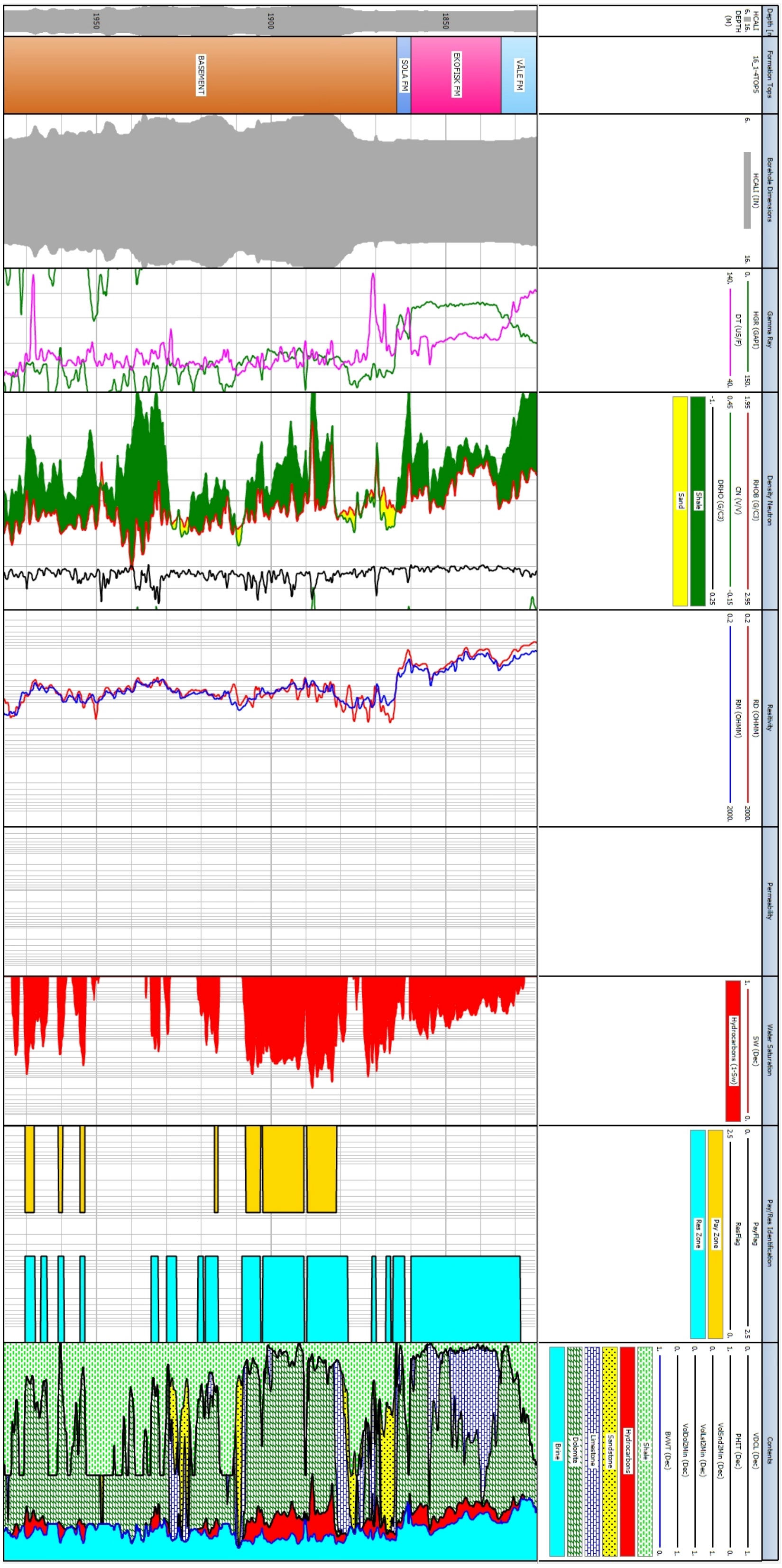

Figure B.6: Petrophysical overview of well 16/1-4

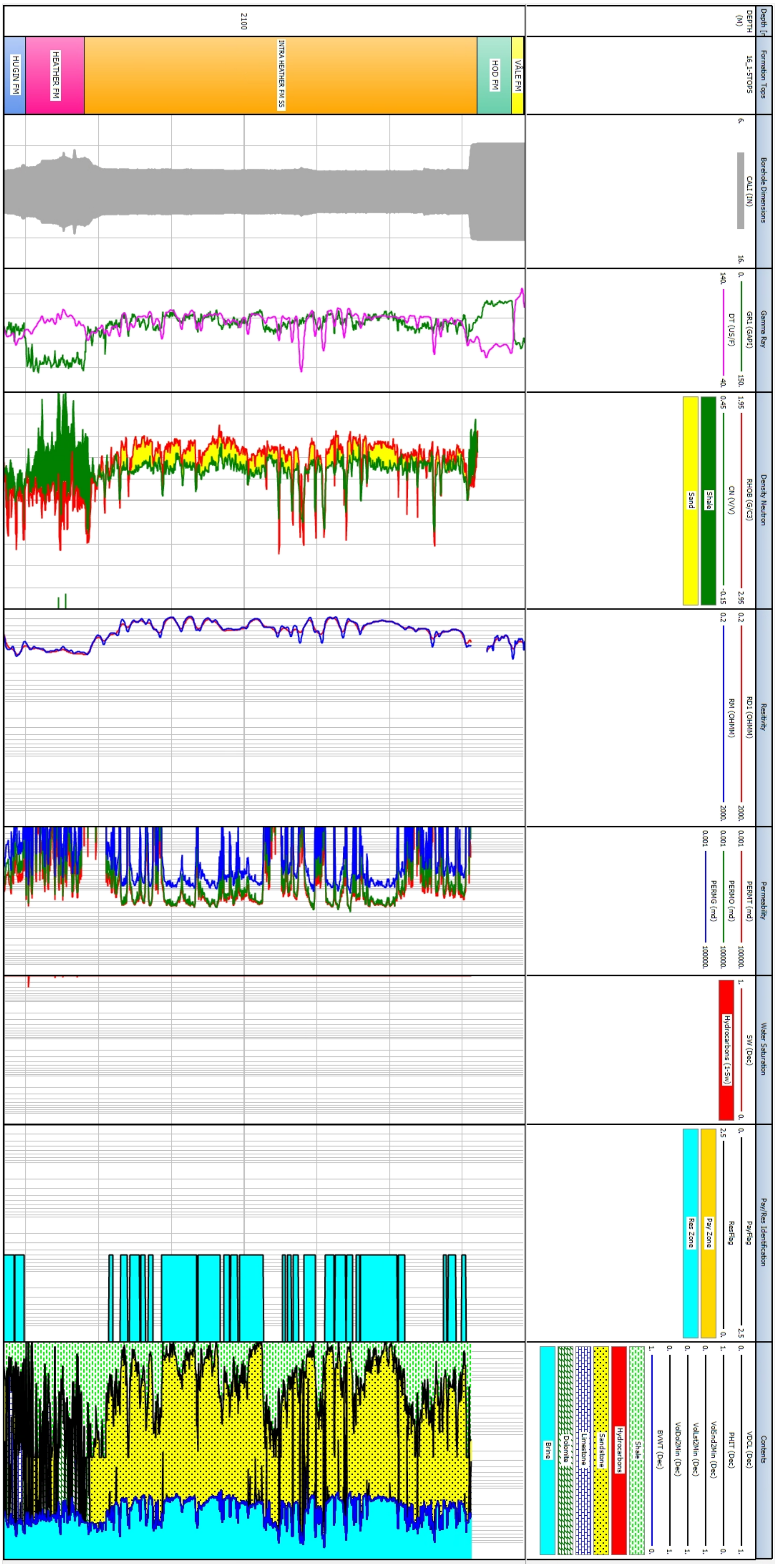

Figure B.7: Petrophysical overview of well 16/1-5

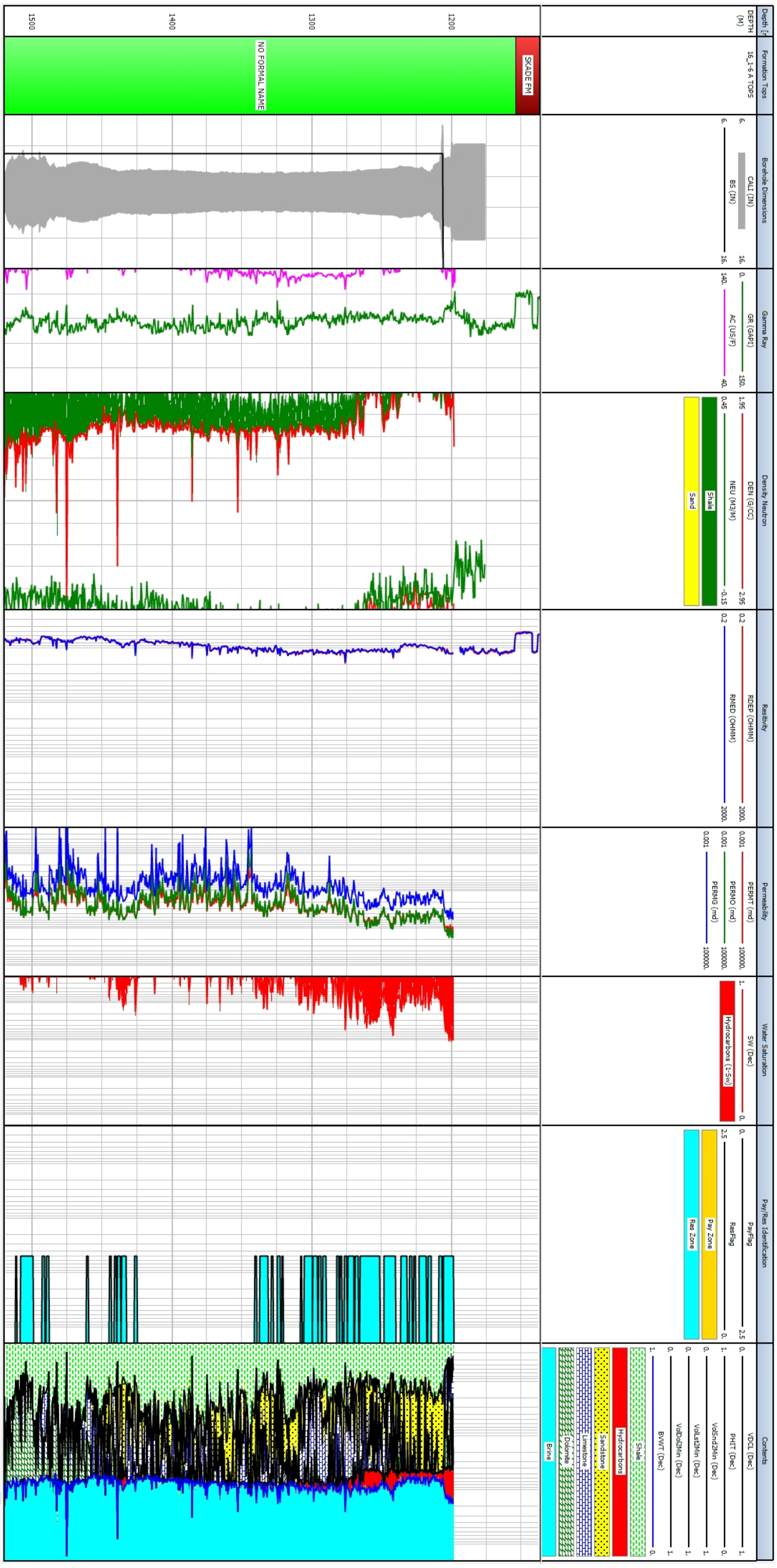

Figure B.8: Petrophysical overview of well 16/1-6 A

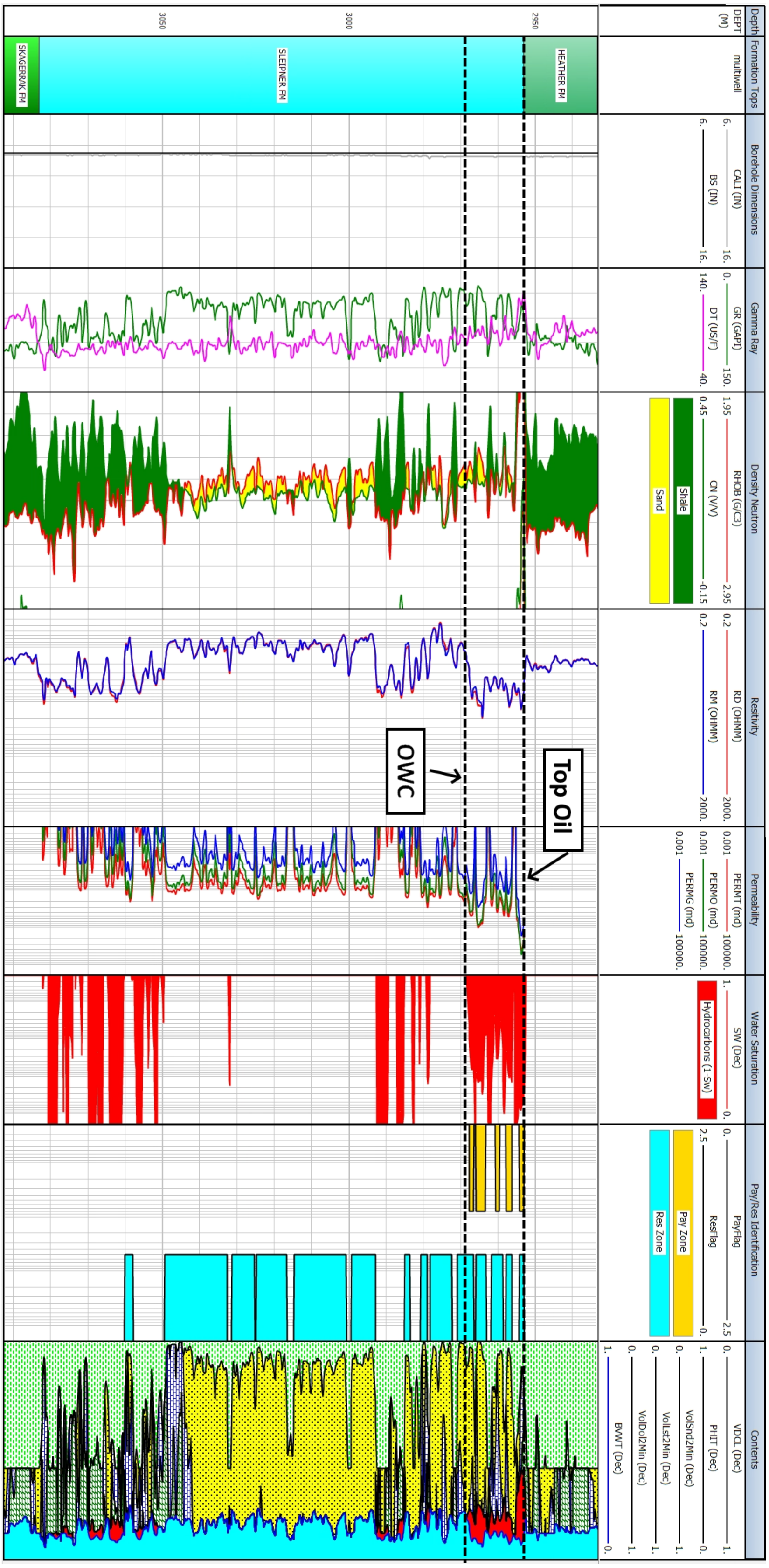

Figure B.9: Petrophysical overview of well 16/1-7

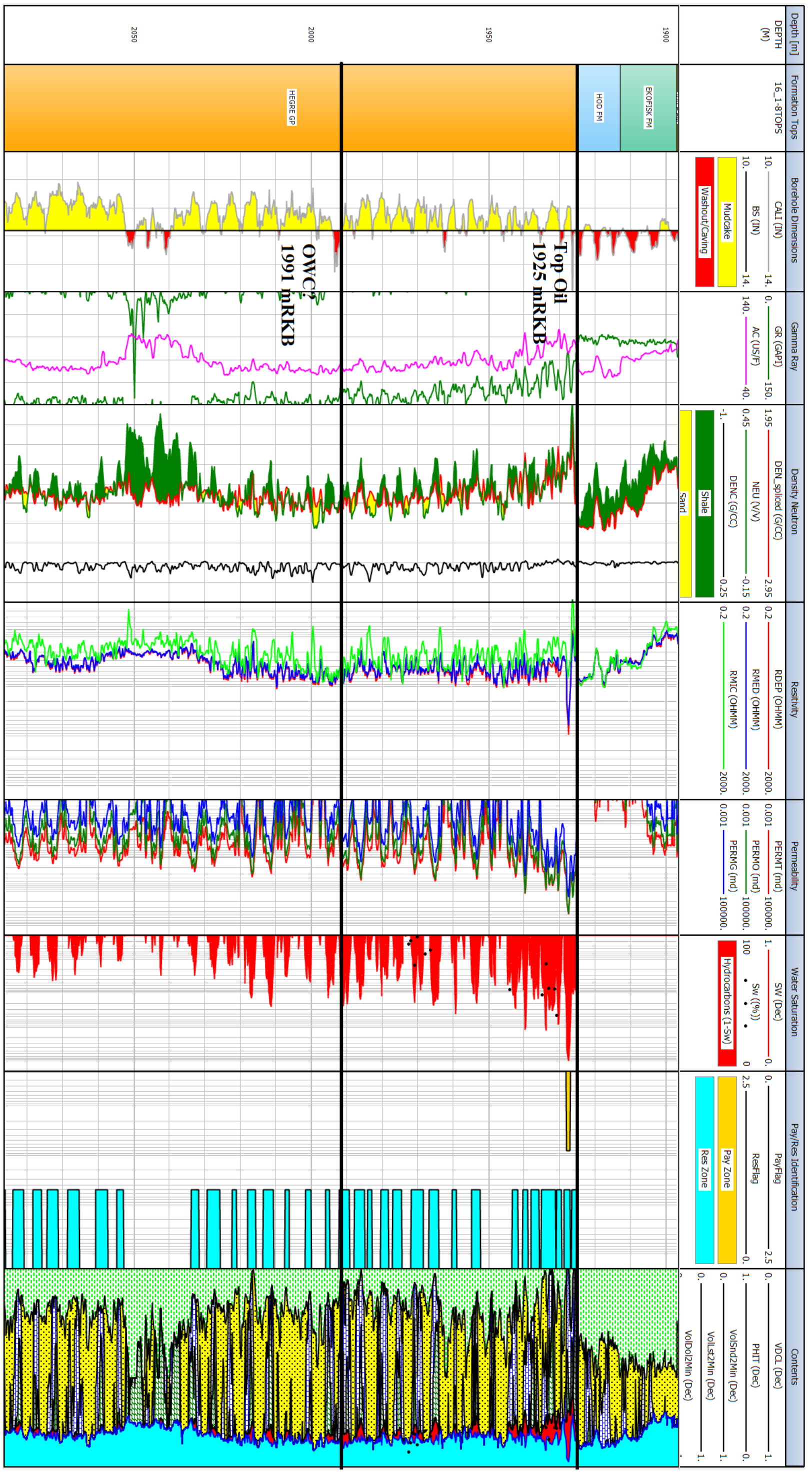

Figure B.10: Petrophysical overview of well 16/1-8

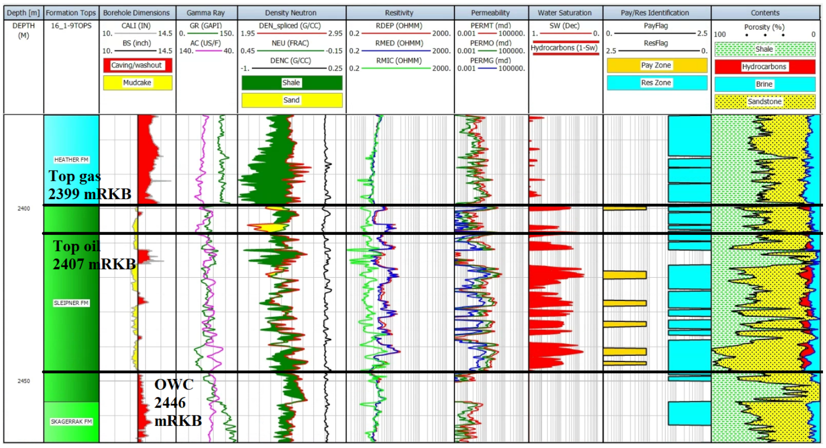

Figure B.11: Petrophysical overview of well 16/1-9

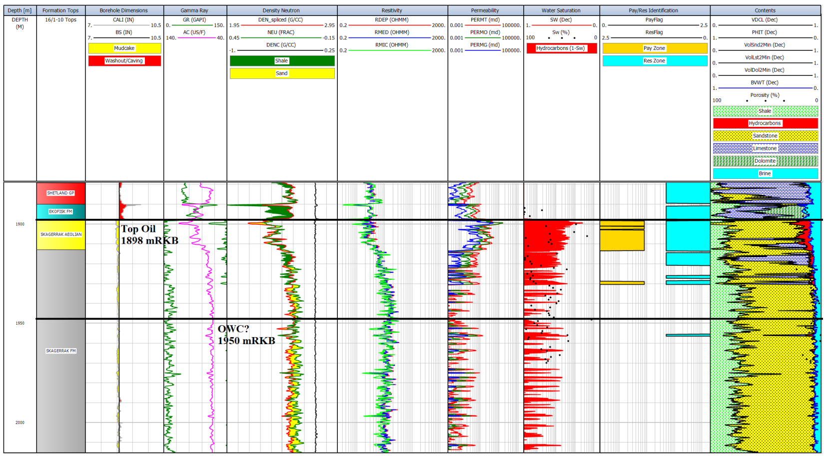

Figure B.12: Petrophysical overview of well 16/1-10

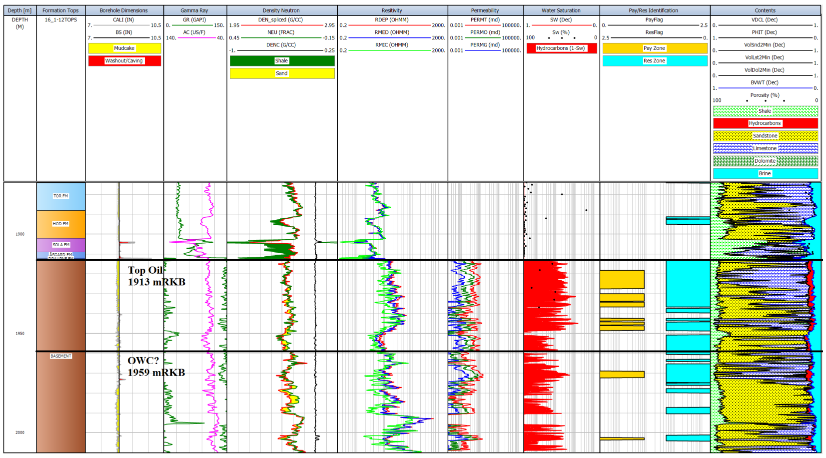

Figure B.13: Petrophysical overview of well 16/1-12

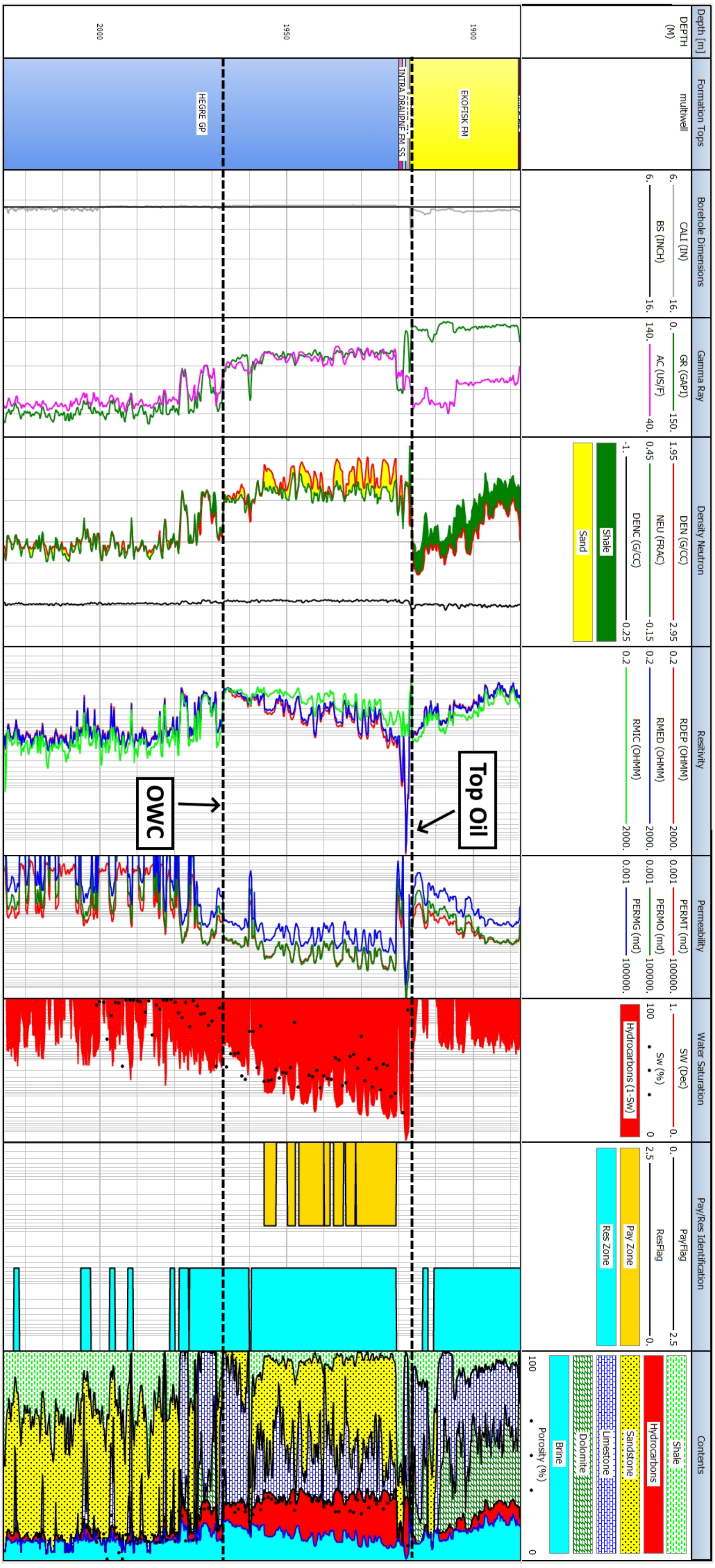

Figure B.14: Petrophysical overview of well 16/1-13

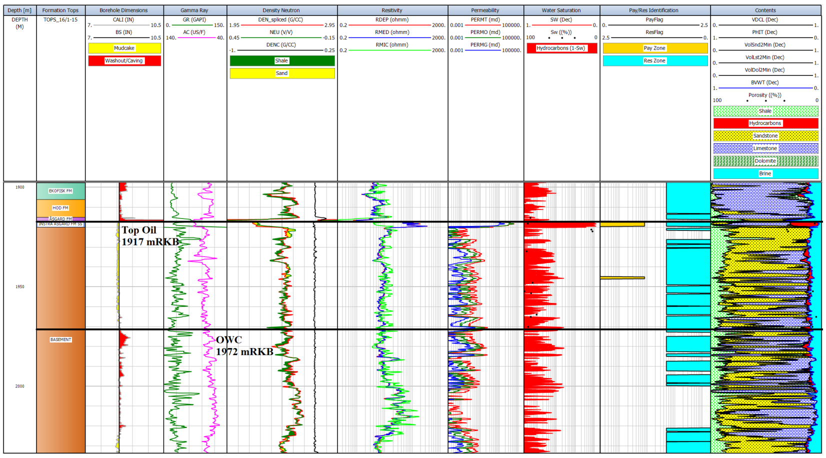

Figure B.15: Petrophysical overview of well 16/1-15

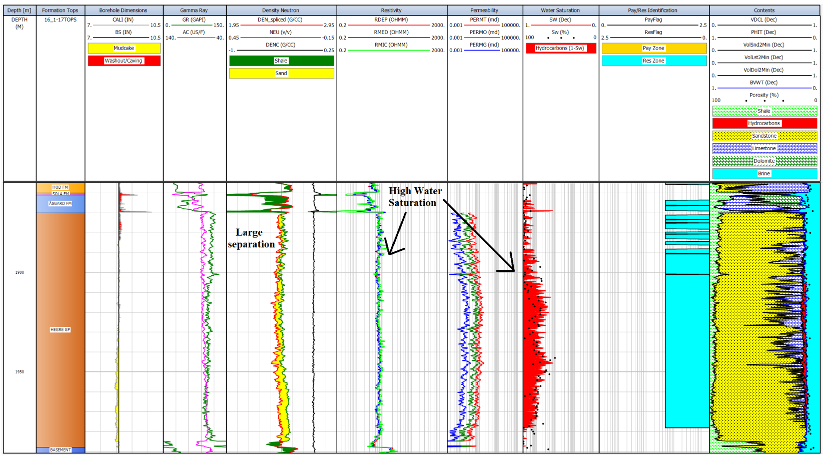

Figure B.16: Petrophysical overview of well 16/1-17

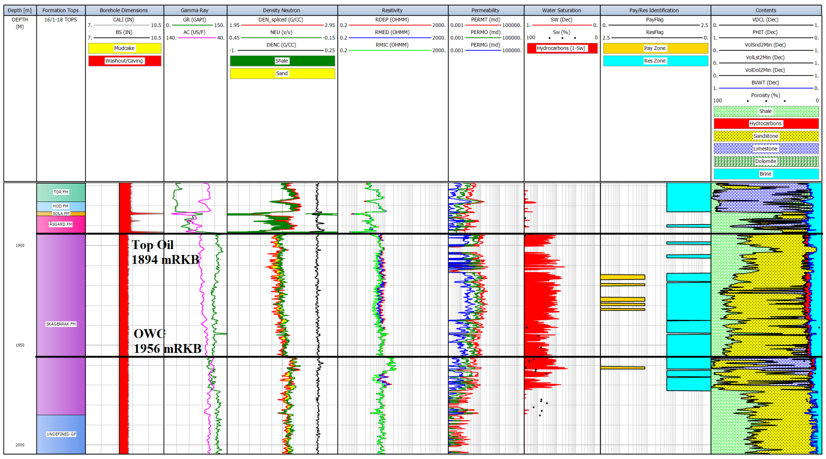

Figure B.17: Petrophysical overview of well 16/1-18

Figure B.18: Petrophysical overview of well 16/1-19 S

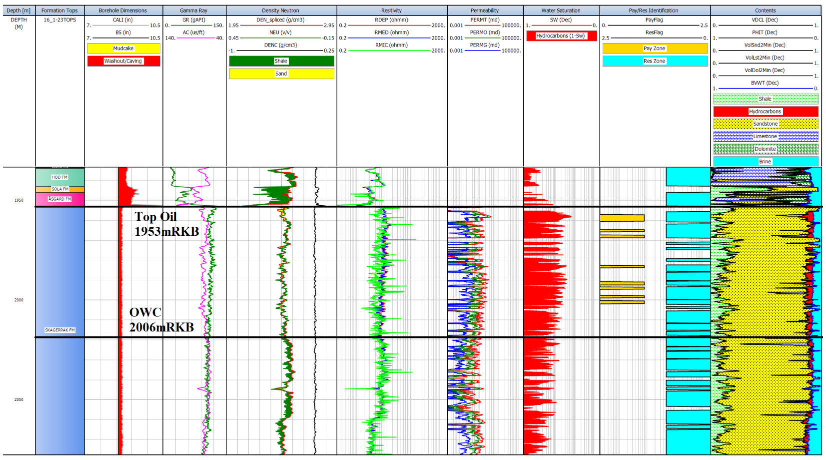

Figure B.19: Petrophysical overview of well 16/1-23 S

APPENDIX C

Crossplots

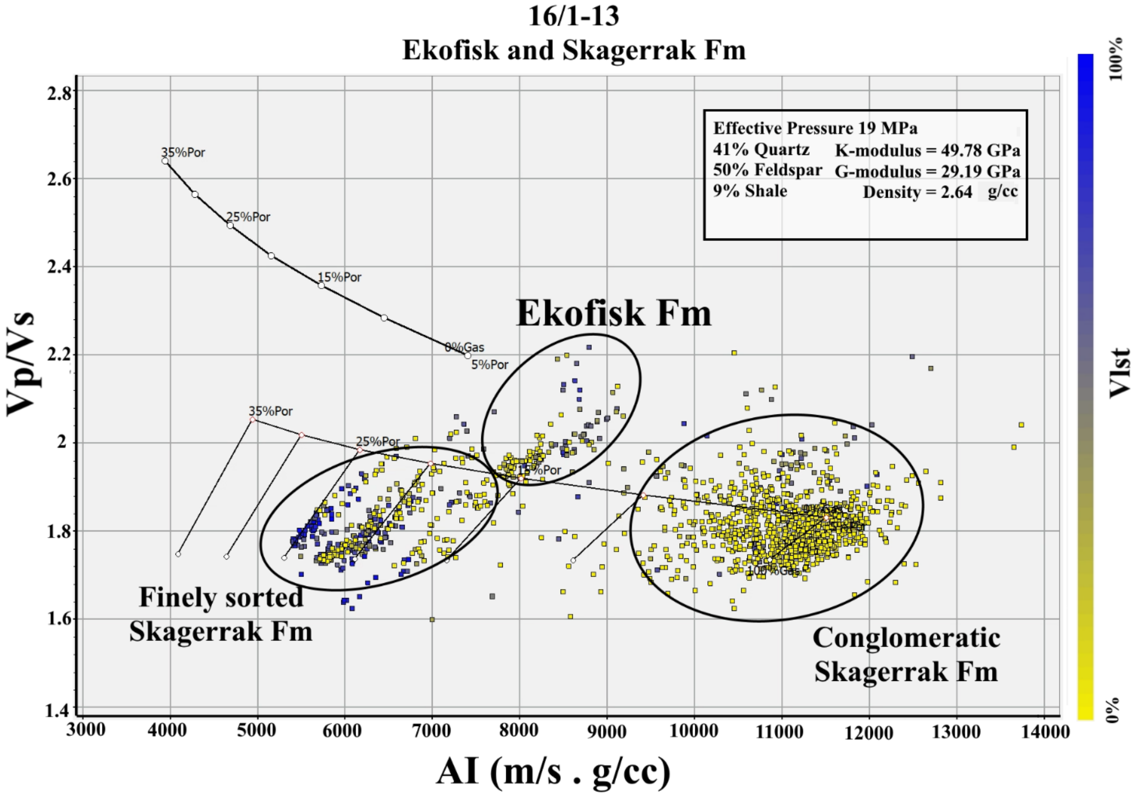

Figure C.1: V_P/V_S vs AI for well 16/1-13 (Edvard Grieg 2nd Appraisal). Color coded for limestone volume.

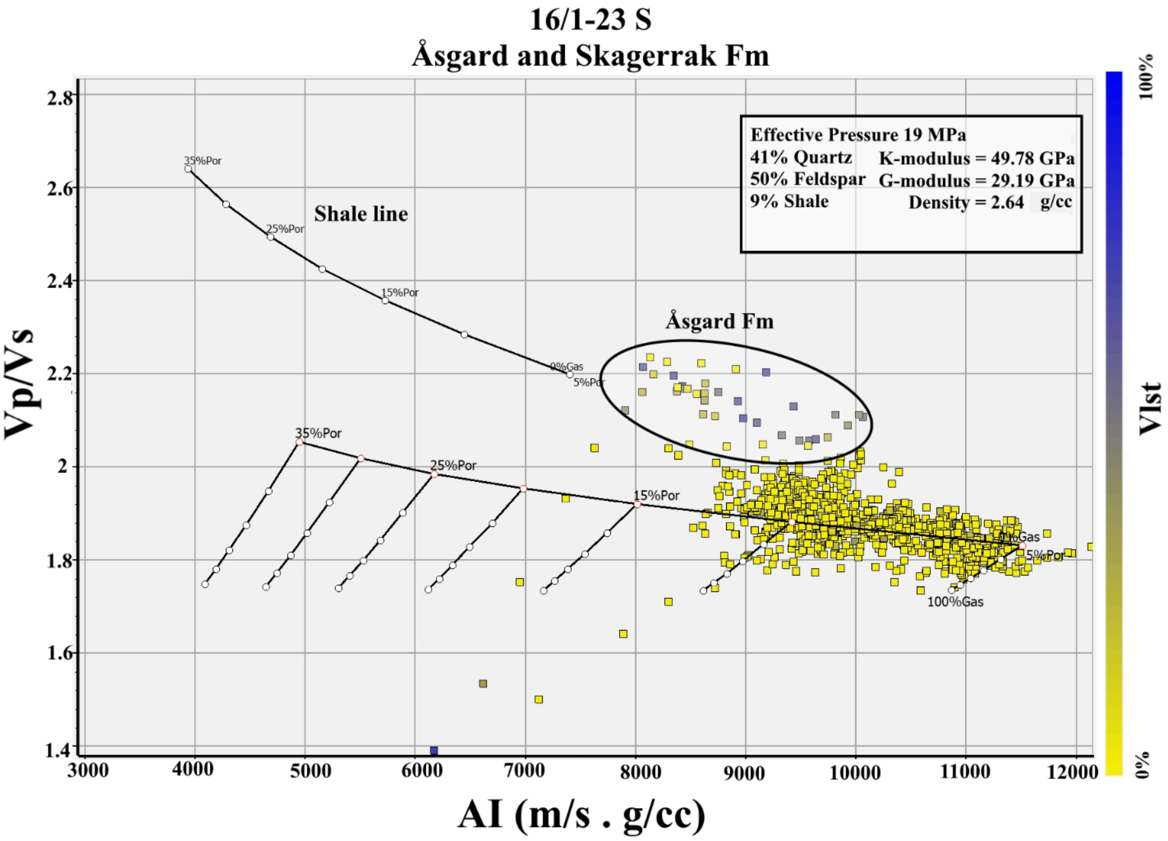

Figure C.2: V_P/V_S vs AI for well 16/1-23 (Edvard Grieg 5th Appraisal). Color coded for limestone volume.

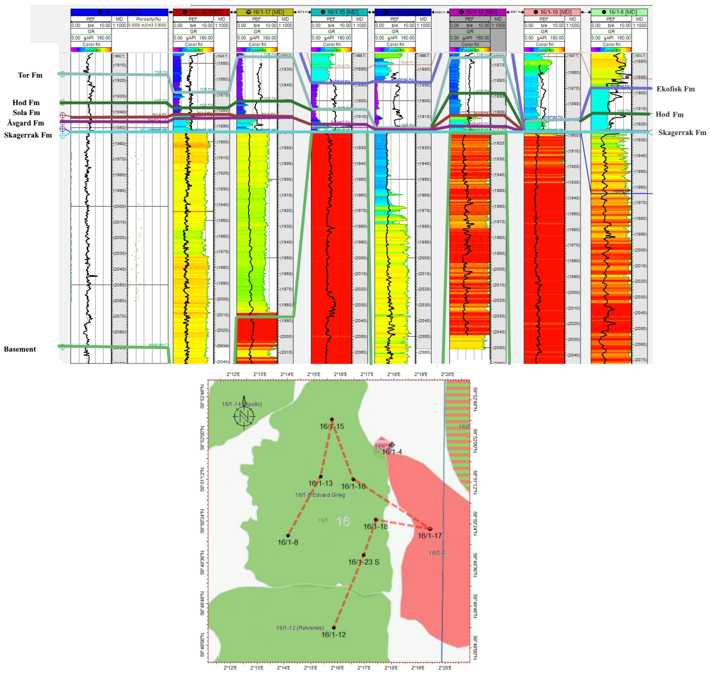

Figure D.1: Well correlation of formations within the Edvard Grieg field. Formations flattened around the Skagerrak Formation. Bottom showing map of well trace.

APPENDIX D

Other

References

Asquith, G. B., Krygowski, D. and Gibson, C. R. (2004). *Basic well log analysis.* Vol. 16. American Association of Petroleum Geologists Tulsa.

Avseth, P. and Odegaard, E. (2004). 'Well log and seismic data analysis using rock physics templates'. In: *First break* vol. 22, no. 10.

Avseth, P. (2015). 'Explorational rock physics: the link between geological processes and geophysical observables'. In: *Petroleum Geoscience.* Springer, pp. 455–488.

Avseth, P., Dvorkin, J., Mavko, G. and Rykkje, J. (2000). 'Rock physics diagnostic of North Sea sands: Link between microstructure and seismic properties'. In: *Geophysical Research Letters* vol. 27, no. 17, pp. 2761–2764.

Avseth, P., Jørstad, A., Wijngaarden, A.-J. van and Mavko, G. (2009a). 'Rock physics estimation of cement volume, sorting, and net-to-gross in North Sea sandstones'. In: *The Leading Edge* vol. 28, no. 1, pp. 98–108.

— (2009b). 'Rock physics estimation of cement volume, sorting, and net-to-gross in North Sea sandstones'. In: *The Leading Edge* vol. 28, no. 1, pp. 98–108.

Avseth, P., Mukerji, T. and Mavko, G. (2010). *Quantitative seismic interpretation: Applying rock physics tools to reduce interpretation risk.* Cambridge university press.

Batzle, M. and Wang, Z. (1992). 'Seismic properties of pore fluids'. In: *Geophysics* vol. 57, no. 11, pp. 1396–1408.

Bellotti, P., Di Lorenzo, V. and Giacca, D. (1979). 'Overburden gradient from sonic log'. In: *SPWLA Transactions.*

Bertozzi, W., Ellis, D. and Wahl, J. (1981). 'The physical foundation of formation lithology logging with gamma rays'. In: *Geophysics* vol. 46, no. 10, pp. 1439–1455.

Bjørlykke, K. (2015a). 'Compaction of sedimentary rocks: Shales, sandstones and carbonates'. In: *Petroleum Geoscience.* Springer, pp. 351–360.

— (2015b). 'Subsurface water and fluid flow in sedimentary basins'. In: *Petroleum Geoscience.* Springer, pp. 279–300.

Bjørlykke, K. and Jahren, J. (2015). 'Sandstones and sandstone reservoirs'. In: *Petroleum Geoscience.* Springer, pp. 119–149.

BP (2021). *Coal: Energy economics: Home.*

Castagna, J. P. and Backus, M. M. (1993). *Offset-dependent reflectivity—Theory and practice of AVO analysis.* Society of Exploration Geophysicists.

Castagna, J. P., Batzle, M. L. and Eastwood, R. L. (1985). 'Relationships between compressional-wave and shear-wave velocities in clastic silicate rocks'. In: *geophysics* vol. 50, no. 4, pp. 571–581.

Castagna, J. P. and Swan, H. W. (1997). 'Principles of AVO crossplotting'. In: *The leading edge* vol. 16, no. 4, pp. 337–344.

Clavier, C., Hoyle, W., Meunier, D. et al. (1971). 'Quantitative interpretation of thermal neutron decay time logs: part I. Fundamentals and techniques'. In: *Journal of Petroleum Technology* vol. 23, no. 06, pp. 743–755.

Crain's Petrophysical Handbook (2021).

Darcy, H. (1856). *Les fontaines publiques de la ville de Dijon. Exposition et application des principes à suivre et des formules à employer dans les questions de distribution d'eau: ouvrage terminé par un appendice relatif aux fournitures d'eau de plusieurs villes au filtrage des eaux et à la fabrication des tuyaux de fonte, de plomb, de tole et de bitume.* Dalmont.

Dvorkin, J. and Nur, A. (1996). 'Elasticity of high-porosity sandstones: Theory for two North Sea data sets'. In: *Geophysics* vol. 61, no. 5, pp. 1363–1370.

Dvorkin, J., Nur, A. and Yin, H. (1994). ‘Effective properties of cemented granular materials’. In: *Mechanics of materials* vol. 18, no. 4, pp. 351–366.

Faleide, J. I., Bjørlykke, K. and Gabrielsen, R. H. (2015a). ‘Geology of the Norwegian continental shelf’. In: *Petroleum Geoscience*. Springer, pp. 603–637.

— (2015b). ‘Geology of the Norwegian continental shelf’. In: *Petroleum Geoscience*. Springer, pp. 603–637.

Gardner, G., Gardner, L. and Gregory, A. (1974). ‘Formation velocity and density—The diagnostic basics for stratigraphic traps’. In: *Geophysics* vol. 39, no. 6, pp. 770–780.

Gassmann, F. (1951). ‘Elasticity of porous media’. In: *Vierteljahrsschrder Naturforschenden Gesselschaft* vol. 96, pp. 1–23.

Gee, D. G., Fossen, H., Henriksen, N. and Higgins, A. K. (2008). ‘From the early Paleozoic platforms of Baltica and Laurentia to the Caledonide Orogen of Scandinavia and Greenland’. In: *Episodes* vol. 31, no. 1, pp. 44–51.

Glover, P. (2013). ‘THE SPECTRAL GAMMA RAY LOG’. In: *Petrophysics MSc Course Notes*.

Goodway, B., Chen, T. and Downton, J. (1997). ‘Improved AVO fluid detection and lithology discrimination using Lamé petrophysical parameters;“$\lambda\rho$”,“$\mu\rho$”, & “λ/μ fluid stack”, from P and S inversions’. In: *SEG technical program expanded abstracts 1997*. Society of Exploration Geophysicists, pp. 183–186.

Greenberg, M. and Castagna, J. (1992). ‘Shear-wave velocity estimation in porous rocks: theoretical formulation, preliminary verification and applications1’. In: *Geophysical prospecting* vol. 40, no. 2, pp. 195–209.

Gregersen, U., Michelsen, O. and Sørensen, J. C. (1997). ‘Stratigraphy and facies distribution of the Utsira Formation and the Pliocene sequences in the northern North Sea’. In: *Marine and Petroleum geology* vol. 14, no. 7-8, pp. 893–914.

Hamilton, E. L. (1956). ‘Low sound velocities in high-porosity sediments’. In: *The Journal of the Acoustical Society of America* vol. 28, no. 1, pp. 16–19.

Han, D.-h., Nur, A. and Morgan, D. (1986). ‘Effects of porosity and clay content on wave velocities in sandstones’. In: *Geophysics* vol. 51, no. 11, pp. 2093–2107.

Isaksen, G. H. and Ledje, K. H. I. (2001). ‘Source rock quality and hydrocarbon migration pathways within the greater Utsira High area, Viking Graben, Norwegian North Sea’. In: *AAPG bulletin* vol. 85, no. 5, pp. 861–883.

Johansen, Y. B., Christoffersen, K., Chatterjee, A., Elfenbein, C., Olsborg, L. H., Kvilaas, G. F., Baig, M. H., Datir, H., Bachman, N., Kausik, R. et al. (2018). ‘Use of Advanced Wireline Logs To Reduce Uncertainties in a Complex Reservoir: A Case Study From the Ivar Aasen Oilfield in the Norwegian Central North Sea’. In: *SPWLA 59th Annual Logging Symposium*. OnePetro.

Klaja, J. and Dudek, L. (2016). ‘Geological interpretation of spectral gamma ray (SGR) logging in selected boreholes’. In: *Nafta-Gaz* vol. 72, no. 1, pp. 3–14.

Kombrink, H. and Patruno, S. (2020). ‘The integration of public domain lithostratigraphic data into a series of cross-border North Sea well-penetration maps’. In: *Geological Society, London, Special Publications* vol. 494. eprint: https://sp.lyellcollection.org/content/early/2020/12/08/SP494-2020-25.full.pdf.

Krief, M., Garat, J., Stellingwerff, J., Ventre, J. et al. (1990). ‘A petrophysical interpretation using the velocities of P and S waves (full-waveform sonic)’. In: *The Log Analyst* vol. 31, no. 06.

Lanson, B., Beaufort, D., Berger, G., Bauer, A., Cassagnabere, A. and Meunier, A. (2002). ‘Authigenic kaolin and illitic minerals during burial diagenesis of sandstones: a review’. In: *Clay minerals* vol. 37, no. 1, pp. 1–22.

Larionov, V. (1969). ‘Radiometry of boreholes’. In: *Nedra, Moscow* vol. 127.

Lindseth, R. O. (1979). ‘Synthetic sonic logs—A process for stratigraphic interpretation’. In: *Geophysics* vol. 44, no. 1, pp. 3–26.

Lundin (July 2018). *Reservoaret på Edvard Grieg ble skapt av storflom.*

Magoon, L. B. and Dow, W. G. (1994). ‘The petroleum system: chapter 1: Part I. Introduction’. In.

Mahmic, O., Dypvik, H. and Hammer, E. (2018). ‘Diagenetic influence on reservoir quality evolution, examples from Triassic conglomerates/arenites in the Edvard Grieg field, Norwegian North Sea’. In: *Marine and Petroleum Geology* vol. 93, pp. 247–271.

Marcussen, Ø., Maast, T. E., Mondol, N. H., Jahren, J. and Bjørlykke, K. (2010). ‘Changes in physical properties of a reservoir sandstone as a function of burial depth–The Etive Formation, northern North Sea’. In: *Marine and Petroleum Geology* vol. 27, no. 8, pp. 1725–1735.

Marion, D., Nur, A., Yin, H. and Han, D.-H. (1992). ‘Compressional velocity and porosity in sand-clay mixtures’. In: *Geophysics* vol. 57, no. 4, pp. 554–563.

Mavko, G., Mukerji, T. and Dvorkin, J. (2009). *The Rock Physics Handbook: Tools for Seismic Analysis of Porous Media.* 2nd ed. Cambridge University Press.

Mindlin, R. D. (1949). ‘Compliance of elastic bodies in contact’. In.

Mondol, N. H., Bjørlykke, K., Jahren, J. and Høeg, K. (2007). ‘Experimental mechanical compaction of clay mineral aggregates—Changes in physical properties of mudstones during burial’. In: *Marine and Petroleum Geology* vol. 24, no. 5, pp. 289–311.

Mondol, N. H. (2015a). ‘Seismic Exploration’. In: *Petroleum Geoscience.* Springer, pp. 427–454.

— (2015b). ‘Well logging: Principles, applications and uncertainties’. In: *Petroleum Geoscience.* Springer, pp. 385–425.

Muprhy, W. F. (1982). ‘Effects of microstructure and pore fluids on the acoustic properties of granular sedimentary materials’. PhD thesis. Stanford University.

Ndingwan, A. O., Kolbjørnsen, O., Straith, K. R. and Bjerke, M. D. (2018). ‘Deciphering the seismic signature of the Edvard Grieg field, North Sea’. In.

NPD (2021a). *4.1 - Geology of the North Sea.*

— (Mar. 2021b). *Activity per sea area.*

— (2021c). *NPD Factpages.*

Omar, M. N. I. B., Lubis, L. A., Zanuri, M. N. A., Ghosh, D. P., Irawan, S. and Jufar, S. R. (2016). ‘Modelling of Seismic and Resistivity Responses during the Injection of CO2 in Sandstone Reservoir’. In: *IOP Conference Series: Earth and Environmental Science.* Vol. 38. 1. IOP Publishing, p. 012006.

Ostrander, W. (1984). ‘Plane-wave reflection coefficients for gas sands at nonnormal angles of incidence’. In: *Geophysics* vol. 49, no. 10, pp. 1637–1648.

Riber, L., Dypvik, H. and Sørlie, R. (2015). ‘Altered basement rocks on the Utsira High and its surroundings, Norwegian North Sea’. In: *Norwegian Journal of Geology* vol. 95, no. 1, pp. 57–89.

Richards, P. G. and Aki, K. (1980). *Quantitative seismology: theory and methods.* Vol. 859. Freeman San Francisco, CA.

Rider, M. M. (1999). *The geological interpretation of well logs.* Whittles Publishing Services.

Rutherford, S. R. and Williams, R. H. (1989). ‘Amplitude-versus-offset variations in gas sands’. In: *Geophysics* vol. 54, no. 6, pp. 680–688.

Rønnevik, H. C. (2015). ‘Exploration strategy’. In: *Petroleum Geoscience.* Springer, pp. 639–651.

Rønnevik, H. C., Jørstad, A. and Lie, J. E. (2017). ‘The Discovery Process behind the Giant Johan Sverdrup Field’. In.

Shuey, R. (1985). ‘A simplification of the Zoeppritz equations’. In: *Geophysics* vol. 50, no. 4, pp. 609–614.

Simm, R., Bacon, M. and Bacon, M. (2014). *Seismic Amplitude: An interpreter’s handbook.* Cambridge University Press.

Steel, R. and Ryseth, A. (1990). ‘The Triassic—Early Jurassic succession in the northern North Sea: megasequence stratigraphy and intra-Triassic tectonics’. In: *Geological Society, London, Special Publications* vol. 55, no. 1, pp. 139–168.

Stieber, S. et al. (1970). ‘Pulsed neutron capture log evaluation-Louisiana gulf coast’. In: *Fall Meeting of the Society of Petroleum Engineers of AIME.* Society of Petroleum Engineers.

SubSurfWiki (2021a). *Hashin–Shtrikman bounds.*

— (2021b). *Wedge model.*

Trice, R., Hiorth, C. and Holdsworth, R. (2019). ‘Fractured basement play development on the UK and Norwegian rifted margins’. In: *Geological Society, London, Special Publications* vol. 495.

Worthington, P. F. and Cosentino, L. (2005). ‘The role of cut-offs in integrated reservoir studies’. In: *SPE Reservoir Evaluation & Engineering* vol. 8, no. 04, pp. 276–290.

Yilmaz, Ö. (2001). *Seismic data analysis: Processing, inversion, and interpretation of seismic data.* Society of exploration geophysicists.

Zanella, E., Coward, M., Evans, D., Graham, C., Armour, A. and Bathurst, P. (2003). ‘Structural framework’. In: *The Millennium Atlas: Petroleum Geology of the Central and Northern North Sea. Geological Society, London* vol. 45, p. 59.

Ziegler, P. A. (1975). ‘The geological evolution of the North Sea area in the tectonic framework of North Western Europe.’ In.

Zoeppritz, K. B. (1919). ‘Über Reflexion ad Durchgang seismischer wellen durch Unstetigkeitsflachen’. In: *Mathematisch-physikalische Klasse*, no. K1, pp. 861–883.